Title
The Effect of Domain Size and Strain Rate on Inelastic Mechanisms in Engineering Solids

Author
Srivastava, Pratyush

Publication Date
2022

Peer reviewed|Thesis/dissertation

UNIVERSITY OF CALIFORNIA

Los Angeles

The Effect of Domain Size and Strain Rate on Inelastic Mechanisms in Engineering Solids

A dissertation submitted in partial satisfaction of the

requirements for the degree Doctor of Philosophy

in Mechanical Engineering

by

Pratyush Srivastava

2022

ABSTRACT OF THE DISSERTATION

The Effect of Domain Size and Strain Rate on Inelastic Mechanisms

in Engineering Solids

by

Pratyush Srivastava

Doctor of Philosophy in Mechanical Engineering

University of California, Los Angeles, 2022

Professor Vijay Gupta, Chair

Understanding the mechanical behavior of solids at small scales is of significant importance for the development of advanced structural materials with superior strength and ductility, and more specifically for the manufacturing of newer class of nano and micro electro-mechanical devices. Every year, new devices are being launched with on-board functional components that are smaller than their previous iterations. The sensors and actuators installed in smartphones to space satellites have now shrunk down to length scales that are below 1 micrometer. Hence, there is a need to characterize the properties of materials at such small scales before they can be employed in the electro-mechanical devices. Majority of materials behave very differently at the nano and micro scales compared to their bulk counterparts. This is primarily due to a reduction in the size and density of the defects. For instance, in crystalline solids, like FCC and BCC metals, the phenomenon of "smaller is stronger" is universally observed, where reducing the characteristic length scale below the

micron level results in a significant increase in the material yield strength. This dissertation focuses on uncovering other significant inelastic mechanisms in crystalline as well as amorphous solids, under a wide range of loading conditions. Inspired from previous simulations and experimental works at small scale, a hypothesis is developed whether "reducing domain size to microscale could be a proxy for increasing the temperature". Since, an increase in situ temperature generally results in reduction in the effective yield strength, the material then should exhibit enhanced ductility at small scales. While the literature has provided evidence of such behavior at lower strain rates in selected materials, the question remains whether such a hypothesis would hold even under dynamic ultrahigh strain rate loading conditions. The aim of this dissertation is to explore the above hypothesis for the entire range of loading strain rates. In addition, this thesis will explore if the above hypothesis is universally valid by choosing two very different material types. The first one is single crystal BCC tungsten (W), which is intrinsically brittle at room temperature in its macroscale form. The second class of material studied in this thesis was the amorphous silica glasses which are among the most abundant materials present on earth. For both materials we demonstrated that reducing the sample size to nano and micro scales resulted in enhanced ductility. For silica glasses, we also observed that the stress required to transform its amorphous phase to its crystalline form was significantly reduced. In fact such a transformation is credited with enhancement of material ductility. Both these phenomena in W and silica glasses are well known to occur at macroscale samples at low stresses only when temperatures are sufficiently high.

Systematic compression and bending experiments were carried out on <100> oriented nano and micro sized pillars and notched-beam specimens of W, respectively. Both types of structures were fabricated via focused ion beam (FIB) milling method and tested using a picoindenter equipped

inside a scanning electron microscope (SEM). First, compression experiments at lower strain rates of 10^{-3} to 10^{-1} s^{-1} were performed on pillars of diameters between 100 nm and 2 μm, with an aspect ratio (AR) equal to 3. The analyses of their stress strain curves revealed that there is a critical size of 500 nm (pillar diameter) below which the plastic flow characteristics, such as the flow stress and strain bursts statistics, become strain rate independent. Second, bending tests on notched cantilever beams with uncracked ligament lengths of 500 nm and 1 μm were performed. The crack propagation was visually recorded, along with the force displacement curves which showed slow and stable crack growth. Even with 2 to 3 times higher yield strength, submicron sized beams exhibited similar crack resistance behavior as their macroscale counterparts. Thus, the combination of compression and bending experiments conclusively demonstrate that W can behave in a ductile manner when its characteristic length scale is reduced below 1 μm. The key mechanisms behind this phenomenon were found to be the enhanced mobility of screw dislocations, driven by extremely high stress levels. Additionally, higher density of mixed dislocations was observed whose mobility is controlled by phonon drag and less dependent on thermal activation. The experimental data was consistent with the above mechanism that was uncovered by previous DDD simulations.

For exploring the size effect in silica glasses, a series of quasi-static and shock compression experiments were conducted on fused silica (FS, 100% SiO_2) and soda lime glass (SLG, 70% SiO_2) samples. The sample types varied from flat plates to nano and micro pillar geometries, which in turn were fabricated using a combination of FIB and photolithography techniques. A laser generated microflyer plate impact setup was developed for shock loading the glass samples. This setup is capable of launching Al discs of 0.8 to 1.5 mm diameter, and 25 to 50 μm thickness, up to speeds ranging between 0.5 and 3.8 km/s. The microflyer generation and its launching was accomplished

by focusing a high energy Nd:YAG laser pulse of 8 ns nominal duration with a special flat-head profile. In macroscale geometry, FS is known to undergo phase transition to crystalline Stishovite at shock stress of 34 GPa. However, no such threshold is known for the SLG material. Therefore, we started with shock compression experiments on SLG plates and analyzed the post-shocked samples using transmission electron microscopy (TEM). A stress threshold value of 7 GPa for Stishovite nucleation was found. This is the first report of Stishovite nucleation stress in the SLG material. Diffusion of cationic impurities under localized shear and friction heating is attributed to such a low crystallization stress in SLG.

To establish the effect of domain size on the polymorphic activity, quasistatic compression of FS and SLG nanopillars (500 nm diameter with an aspect ratio equal to 2) was conducted inside an SEM, using the same setup that was used for the W study. Both materials showed unprecedented plastic flow with strains reaching above 50% and a complete absence of brittle failure. Furthermore, TEM analysis of deformed SLG pillars revealed 4 nm regions of Stishovite crystals. The corresponding stress for this transformation was estimated to be only 4.2 GPa, which is 40% of the Stishovite nucleation stress of 7 GPa observed in macroscale samples. The diffusion of cationic impurities under very high shear stresses in the SLG pillars is explained as the key mechanism for such a low Stishovite nucleation stress. Interestingly, no Stishovite crystals were observed in any of the FS TEM samples, regardless of the pillar size, where the maximum stress was limited to only 7.2 GPa. Thus, it appears that Stishovite nucleation in FS pillars requires much higher stresses. Unfortunately, such an enhancement of the stress would have required further reduction in pillar size which was not possible due to constraints of the manufacturing procedure and equipment.

However, to overcome the above limitations, the stress levels in the FS pillars was enhanced via

shock loading by impacting them with microflyer plates launched at speeds ranging from 0.5-3.8 km/s. For this study, FS pillars of 3 - 15 μm in diameter and with an aspect ratio of 1 were fabricated by using the photolithography technique. X-ray diffraction analyses of the shocked samples showed crystalline peaks corresponding to Stishovite nucleation. The corresponding stress was estimated to be 15.24 GPa in the smallest pillars of 3 μm diameter. This stress is almost half of 34 GPa that has been widely accepted as the Stishovite nucleation stress for bulk FS. These observations conclusively demonstrate that reducing the domain size to nano and micro scales results in a significant reduction in the threshold stress for the onset of polymorphic activity in silica glasses.

The dissertation of Pratyush Srivastava is approved

Ajit K. Mal

Guruswami Ravichandran

Nasr M. Ghoniem

Vijay Gupta, Committee Chair

University of California, Los Angeles

2022

TABLE OF CONTENTS

LIST OF FIGURES

LIST OF TABLES

ACKNOWLEDGEMENTS

First and foremost, I would like to thank my parents for their unwavering love and support.

I would like to express my sincere gratitude to my advisor, Prof. Vijay Gupta, for his invaluable guidance and constant encouragement during my PhD. I am very grateful for his insights and help towards both academic and non-academic parts of my life. His trust in my capability early on gave me tremendous motivation and confidence which shaped my career very positively.

I would like to thank my committee members, Prof. Ajit Mal, Prof. Guruswami Ravichandran, and Prof. Nasr Ghoniem for their valuable insights, suggestions and reviews of my research.

I would also like to thank Prof Yinan Cui for all the invaluable discussions and helping in figuring out the scientific mechanisms involved in my experiments. I greatly appreciate the help of Katherine Jiang and Noah Bodzin in training me on SEM and FIB sample preparation. I am also grateful to Carlos Gamez and Brian Ramirez for training me on the laser setups early on in my PhD work.

I would like to thank MAE administrative staff Abel Lebon, Marla Cooper and Lance Kono for always being available to help me out with all my requests.

VITA

2015 B. Tech in Mechanical Engineering
Maulana Azad National Institute of Technology
Bhopal, India

2017 Executive Engineer
Larsen & Toubro Limited
Talegaon, India

PUBLICATIONS

[1] **Srivastava, P.**, Tanaka, K., Ramirez, B., & Gupta, V. (2021). Stishovite nucleation at low shock pressures in soda-lime glass. Acta Materialia, 215, 117124.

[2] **Srivastava, P.**, Jiang, K., Cui, Y., Olivera, E., Ghoniem, N., & Gupta, V. (2021). The influence of nano/micro sample size on the strain-rate sensitivity of plastic flow in tungsten. International Journal of Plasticity, 136, 102854.

[3] Cui, Y., Po, G., **Srivastava, P.**, Jiang, K., Gupta, V., & Ghoniem, N. (2020). The role of slow screw dislocations in controlling fast strain avalanche dynamics in body-centered cubic metals. International journal of plasticity, 124, 117-132.

[4] Pozuelo, M., Lefebvre, J., **Srivastava, P.**, & Gupta, V. (2019). Stishovite formation at very low pressures in soda-lime glass. Scripta Materialia, 171, 6-9.

Chapter 1. Introduction

1.1. Knowledge Gap in Size Effect in BCC Metals

A number of experiments have demonstrated that the flow stress in all body-centered cubic (BCC) crystals decreases sharply as the test temperature is increased. This behavior is observed up to a critical temperature, above which the flow stress becomes athermal [1–3]. This phenomenon is generally attributed to a fundamental mechanism that controls dislocation motion in BCC crystals. At temperatures below a critical value, kink pairs must be nucleated on the non-planar core structure of screw dislocations by overcoming an energy (Peierls) barrier. Subsequent migration of nucleated kinks leads to overall dislocation motion. The need to overcome the Peierls barrier either through thermal activation or through application of higher stress makes the BCC metals intrinsically brittle below the critical temperature (T_c). Above T_c, however, the dislocation motion does not require overcoming the Peierls barrier as it is dominated by phonon drag similar to that in the FCC polycrystals. Therefore, in this temperature regime, BCC metals respond in a ductile fashion. Since T_c for most BCC metals like tungsten (W) is quite high (>500K), they are brittle at room temperature. Because of its brittleness, W must be heated during machining and various forming processes that not only makes it expensive but also limits its application domain considerably.

Recent experiments on the plasticity of BCC crystals using submicron pillars have revealed that the flow stress increases sharply with a decrease in the sample size and that the stress-strain relationship exhibits discrete strain bursts instead of the smooth and continuous plastic flow that is characteristic of the polycrystals [4–6]. The underlying dislocation nucleation, multiplication, and propagation mechanisms that give rise to this size effect and strain burst behavior have also

been investigated by use of various Dislocation Dynamics models. It must be noted however that the vast majority of these studies have been carried out at quasi-static strain rates ($< 10^{-3}$ s^{-1}). The combined effects of strain rate and size on the flow stress of the BCC metals have received less attention. The strain rate sensitivity of BCC metals is associated with the motion of screw dislocations, because their non-planar core structure leads to very slow mobility, as compared to edge dislocations [5, 7–9]. Similarly, all prior studies have focused on the effect of size on the flow stress, without addressing the effect on fracture toughness, a property that more accurately measures the brittle versus ductile character of a material. It is controlled by the ability of the material to sweep out crack tip-nucleated dislocations in relation to the crack speed or loading rate. Thus, there is a knowledge gap with respect to the effect of domain size on strain rate sensitivity and fracture behavior of BCC metals. To fill this gap, single crystal Tungsten (W) is chosen as the model material.

1.1.1. Can small size lead to ductility in BCC at room temperature?

In light of the above discussion, an important question that remains unanswered is whether the temperature and strain rate will still have the same strong influence on the flow stress and fracture behavior in small volumes, as is the case in conventionally large BCC specimens? The current work is motivated by observations made by Cui et al. [10] where Discrete Dislocation Dynamics (DDD) simulations were carried out exploring the coupled effects of sample size and temperature in Tungsten single crystals. It was found that as the pillar's diameter was decreased from 2000 nm to 200 nm, while maintaining an aspect ratio of 2, the entire stress-strain characteristic, including the flow stress, became invariant over a very wide range of temperatures (150K-900K)! (Fig. 1.1). They attributed this behavior to enhanced mobility of screw dislocations on account of high stress,

their premature annihilation, and a significant decrease in their storage capacity in submicron pillars. Consequently, this resulted in a transition of the dislocation mobility mechanism from kink-pair dominated to that by phonon-drag even at 150K! This temperature independent phonon-drag mechanism is a hallmark of deformation in the ductile regime of BCC metals.

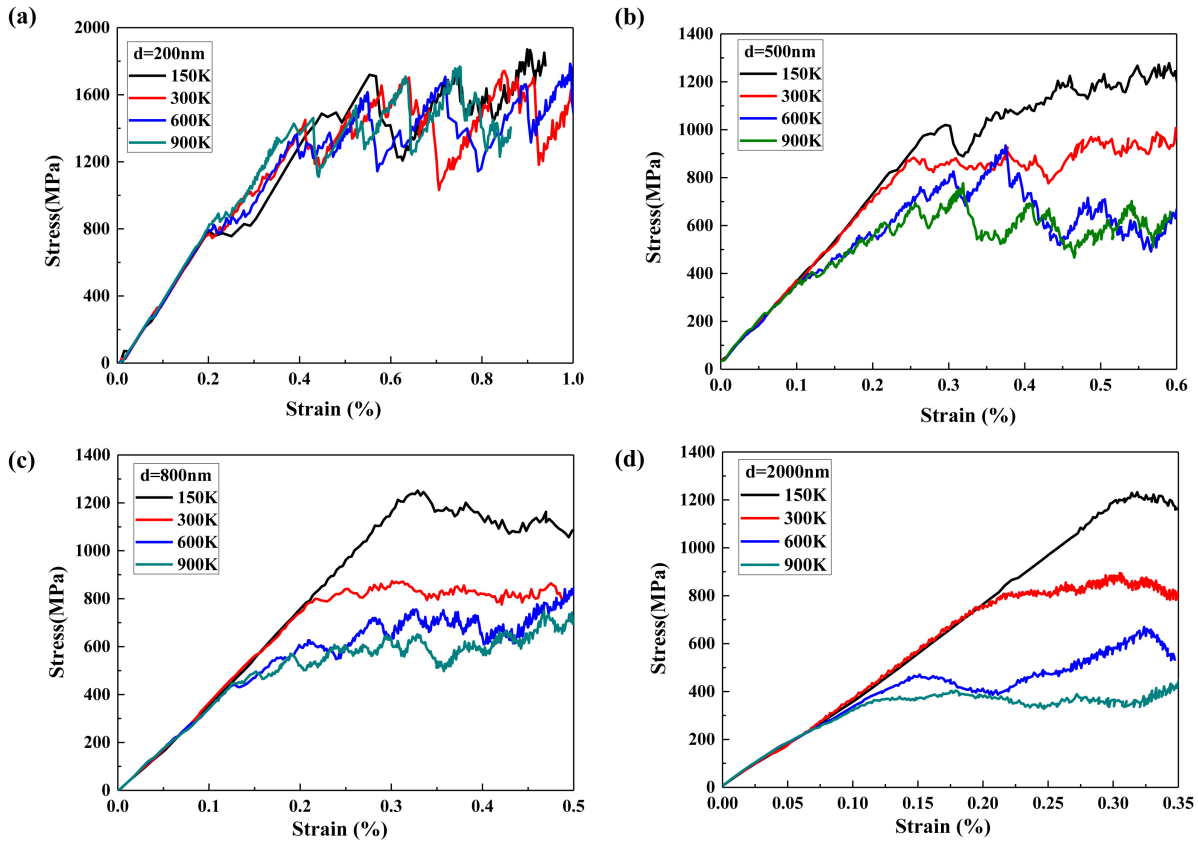

Figure 1.1: Stress-strain curves for micropillar tension test under different temperatures with diameter (a) 200 nm, (b) 500 nm, (c) 800 nm and (d) 2000 nm [10]

The DDD model by Cui et al. [10] were later validated experimentally by Abad et al. [11]. They carried out in-situ SEM compression tests up to 400°C on 500 nm to 5 μm in diameter Ta and W pillars. For both Ta and W, the stress-strain characteristics for the 500 nm diameter pillar is insensitive to the temperature change while the largest 5 μm pillar shows a significant variation. This experimental verification gives confidence in prediction of the change in dislocation mobility mechanism with sample / grain size and raises a distinct possibility of enhancing the room

temperature ductility of BCC metals while still retaining their very high strengths.

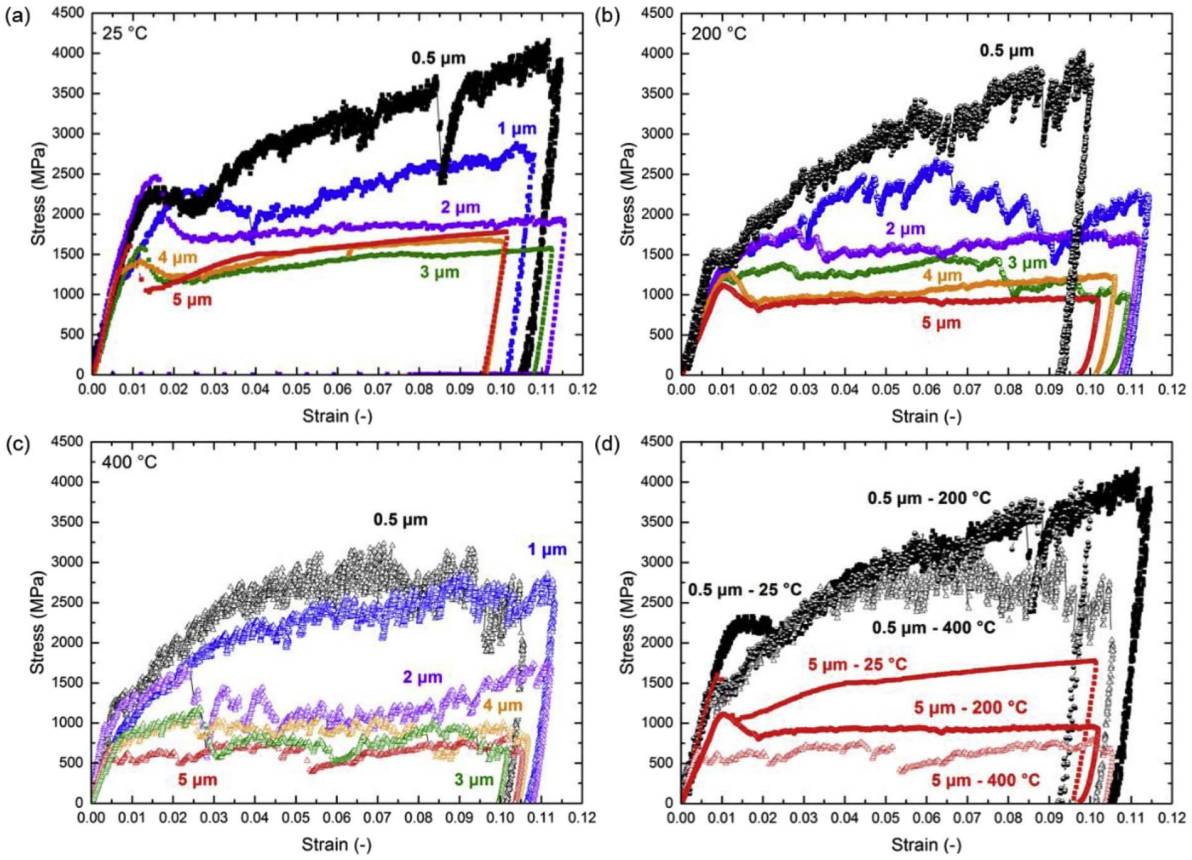

Figure 1.2: Compressive stress-strain curves for 0.5 - 5 μm diameter W pillars at 25°C, 200°C, and 400°C, clearly showing that the stress strain behavior becomes temperature independent at the smaller size [11]

In general, loading at ultra high strain rates and / or very low temperatures can induce brittle deformation in metals. Yet another surprising result was obtained by Crum et al. [12] where they deformed FIB-manufactured 500 nm diameter (100) copper single crystal pillars by loading the samples along the <100> axis by laser- driven stress waves of 1 ns rise time (Fig. 1.3 (a-d)). The pre- and post-shocked samples were analyzed using HRTEM, SEM, and SAED analysis to confirm the dislocation structures. These experimental observations were confirmed by MD simulations [13]. Remarkably, Cu pillars that were precooled to 100 K were found to accommodate a substantial compressive strain either through axial shortening (Fig. 1.3 (c)) or formation of a heavily displaced

shear band (Fig. 1.3 (b)) when loaded at an ultrahigh strain rate of 10^8 s^{-1}. In another laser generated shock wave study by Colorado et al. [14], when Cu nanopillars were loaded perpendicular to their axis by the shock wave (shock bending), they were found to bend by 180° even at such ultrahigh strain rates (Fig. 1.3 (e-h)). HRTEM images of the shocked pillar in the vicinity of a twin boundary are shown in Fig. 1.3 (h). Fourier transforms (FT) of the HRTEM images clearly show the presence of new grains. This is a remarkable finding as such a material rearrangement has occurred within few nanoseconds. Thus, DDD results on BCC nanopillars and the shock compression data on FCC pillars seem to indicate the availability of a general thesis that there may be a fundamental connection between small size and ductility which apparently cannot be perturbed either by ultrahigh strain rate loading or cryogenic temperatures. The current study intends to examine this thoroughly.

In the present study, single crystal Tungsten is chosen as the prototypical BCC metal whose plastic behavior is known to be strongly temperature and strain rate sensitive, making it an ideal candidate for exploring the size effect phenomenon. Fundamentally, including the effects of temperature and strain rate broadens the scope of the size effect as it can provide further insights into the age-old problem of how grain size affects strength and ductility of an alloy and how the local dislocation-based deformation processes fundamentally control the brittle-to-ductile transition temperature of BCC metals. This research can possibly lead to some general rules that may even be applicable to other crystal classes.

Technologically, understanding the deformation process in W is important since it has numerous ultra-high temperature applications, such as in magnetic fusion energy devices, plasma-facing components [15], and space electric propulsion, and is hard to machine in its bulk form at room

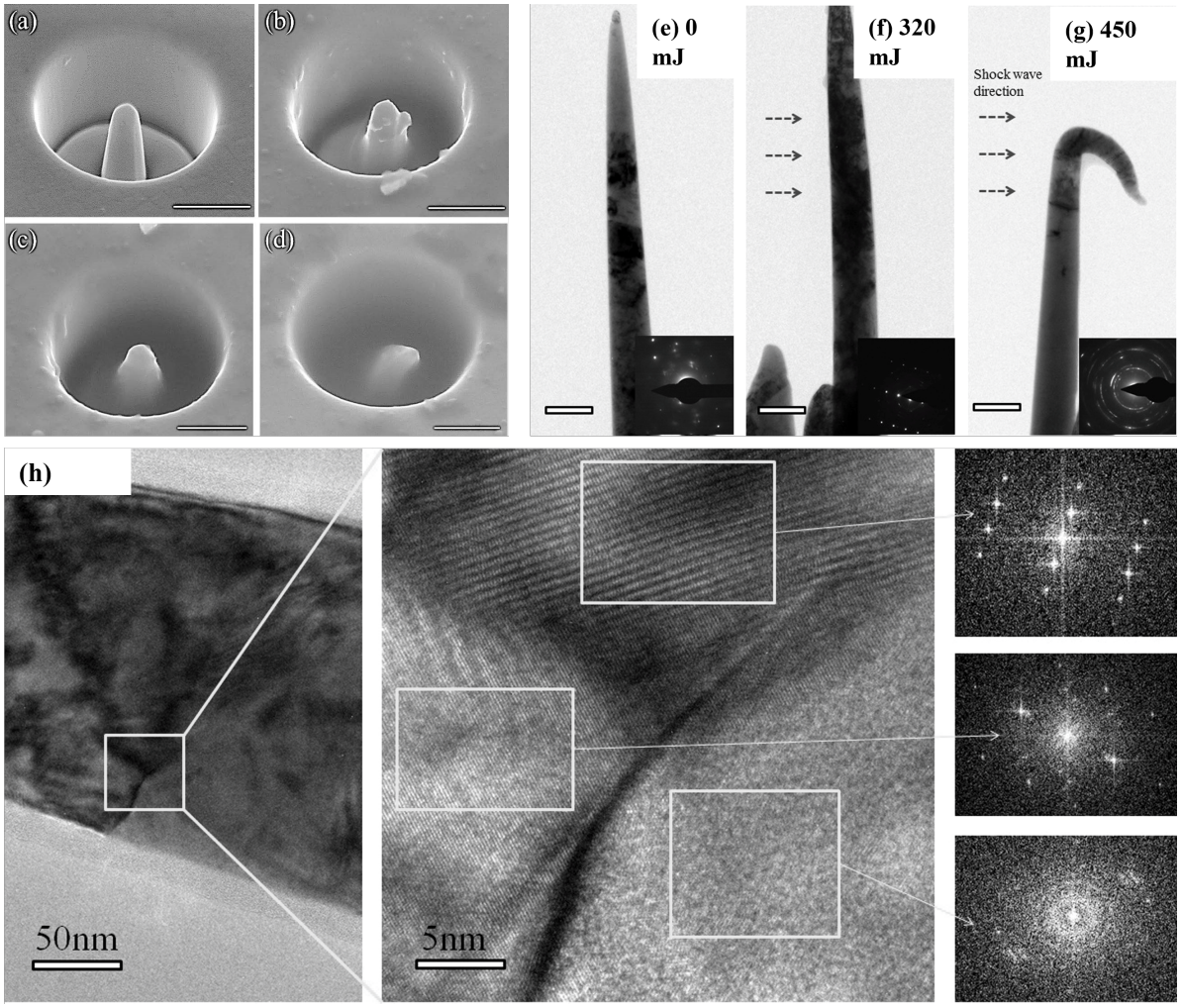

Figure 1.3: Cu nanopillars under high-energy shock- loading at cryogenic temperatures (a) before loading and (b), (c) & (d) after loading the pillar with a 700 kJ/m^2 fluence shock-wave [12]. Scale is 1 μm. (e-g) TEM bright field image of Cu nanopillars under high-energy shock bending at room temperature at different laser pulse energies [14]. Scale is 200 nm. (h) HRTEM images of the shock loaded pillar from (f). Panel to the right show FFT patterns of different areas boxed in the central panel. Two areas taken above the twin boundary has different orientation.

temperature. The study results can be directly used for improving the performance and reliability of various electronic and thermomechanical devices through direct control of crystal size and structure. A study at this level is also important for understanding the fatigue and fracture limits of newer types of active material-based microscale sensors, actuators and energy conversion and storage devices that function by coupling electrical, magnetic and optical fields to mechanical deformations.

1.2. Polymorphic Activity in Silica Glasses

There is a significant interest in understanding the behavior of silica glasses (such as Fused Silica and Soda Lime) under extreme conditions of temperature (>1000°C) and pressure (>20 GPa) as they undergo a phase transformation with up to 40% or more volume change. During this process, several high density polymorphs, including the ultra-hard Stishovite phase which has a density of 4.313 g/cc, are formed. These transformations consume an enormous amount of energy. Since such extreme conditions of temperature and pressure are generated during impact of hypervelocity projectiles, there is a significant interest in the armor design community to incorporate silica glass in advanced armor concepts for protection against shaped charges that send explosively formed projectiles with speeds up to 10,000 m/s.

Unlike fused silica, limited efforts have been made to observe and quantify the polymorphic activity in soda lime glass (SLG). Roshdy et al. [16] subjected a stack of soda-lime glass layers to a hypervelocity penetrator and analyzed the debris left behind in the channel created by the penetrator. The debris was washed several times in a hydrofluoric acid bath (in which Stishovite phase dissolves very poorly) prior to X-ray diffraction analysis, which confirmed the formation of the Stishovite phase. By subjecting SLG samples to shock pressures up to 110 GPa, Gorfain et. al. [17] found that the high pressure Hugoniot of SLG displayed stiffness that was similar to that of pure Stishovite. Alexander et. al [18] measured the release response of SLG from pressures as high as 40 GPa and observed a change in the shock release dynamics when compared to the fused silica response. Their work suggested that the network modification of silica due to the presence of alkali oxides in SLG inhibits transition to the Stishovite phase. However, the high-pressure steepness in the Hugoniot curve, similar to Stishovite hydrostat, suggested a quick reversible transition that prevents

freezing of the Stishovite phase. In all of these previous studies the entire volume of the sample is transformed into the crystalline phase which is then spotted through the change in continuum-level mechanical response. However, among recent studies on shock response of SLG, Renganathan et. al. [19] provided a different picture of continuum response at high stress levels (37 – 120 GPa). The linear shock velocity – particle velocity ($U_s - u_p$) model in their study shows that the Hugoniot states do not match the stiffness of the Stishovite phase as observed in fused silica. Hence there is a lack of consensus of Stishovite formation in SLG. Furthermore, the pressure threshold at which the Stishovite nucleates in bulk SLG is currently unknown.

1.2.1. Effect of Domain Size on Polymorphic Activity in Silica Glasses

The effect of domain size in the high pressure glass densification phenomenon has never been explored before despite the enormous attention received by this problem over several decades. The motivation to explore the effect of small domain size in silica glass stems from the works of Cui et al. [10], Crum et al. [12] and Colorado et al. [14], explained in section 1.1.1. Based on their collective efforts of DDD simulations and laser generated shock wave experimental results, one can then conclude that decreasing the sample size has a very similar effect as that of increasing the temperature. Should this translate to silica glass, then decreasing the domain size, which is proxy for increasing the temperature, should result in substantially low stress threshold for causing the transformation to the high density Stishovite phase. This is because there is ample evidence in literature that polymorphic transformation to high density phases occurs at much lower pressures at elevated temperatures. For example, Nishiyama et al. [20] synthesized Stishovite polycrystals at 100°C intervals between 1200 and 2000°C at a fixed pressure of only 15 GPa. More systematic studies exploring the polymorphic transitions in the pressure- temperature space has been done

in fused silica [21–23]. Soda-lime glass behaves similar to fused silica at higher pressures so the results from such studies can serve as a guide to further understand the phase transformations in soda-lime glass. These studies show that silica glass can undergo reversible and irreversible polymorphic transitions under pressure, leading to the elastic softening upon initial compression and permanent densification under high pressure. At room temperature (cold-compression) and pressures above 8–9 GPa, irreversible densification starts, reaching a maximum of 21% after further compression to 18–20 GPa. The same or even higher amount of densification can be achieved under much lower pressures (4–8 GPa) at high temperatures (hot compression).

Thus, higher densities can be attained at much lower pressures at higher temperatures in both fused silica and soda-lime glass. If the small domain size, even when compressed at room temperature, results in a condensed microstructure that would be similar to that created through hot compression (as small domain size is proxy for increasing the temperature) then one might be able to enjoy the additional benefits of much higher hardness and elastic moduli of hot compressed samples. Recent work of Guerette et al. [24] has confirmed this and showed that even though the hot compressed samples had the same density as the cold compressed samples, its bulk modulus was 16% higher. The resulting hardness was also substantially higher. By evaluating the samples using X-ray diffraction, Raman, BLS, and MD simulations, they showed the two samples to have very different internal molecular structures despite having very similar densities. The main summary of their findings is that the microstructure of the cold-compressed material is still inhomogeneous like its parent with large remaining pores and a broader distribution of both low and high member rings while the hot-compressed material has a more uniform microstructure with much smaller voids and narrower distribution of higher member rings.

In addition to the above queries, axial loading of amorphous silica (fused silica and soda lime glass) in small domains at different strain rates should allow us to study the formation and stability of high-pressure polymorphs of silica, such as Stishovite, during high pressure compaction. The proposed experiments will also bring out the effects of quasi-static as well as ultrahigh strain rates along with shear stress which has never been studied in a systematic manner before. All this would provide valuable experimental data which should assist in the development of constitutive models for silica glass and ultimately help in the development of glass-based advanced armor concepts for protection against hypervelocity projectiles.

1.3. Organization of the Dissertation

The layout of this dissertation is as follows. Chapter 2 provides a thorough experimental analysis on the influence of domain size on plastic behavior in single crystal tungsten. The domain size is defined by the dimensions of the nano- and micropillar samples fabricated via focused ion beam (FIB) milling. Chapter 3 further takes the domain size inspection to the fracture behavior in tungsten. Microcantilever beams fabricated via FIB are employed for the fracture experiments and elastic-plastic fracture mechanics is used to quantify the fracture process.

Chapter 4 begins the domain size investigation into silica glasses. Development of a table-top laser-generated flyer plate impact setup is described. This setup is employed to conduct planar shock experiments on silica glass plates to establish a threshold of polymorphic activity in the bulk material, before proceeding on to the micro scale structures. Chapter 5 provides a detailed account of the uniaxial quasistatic compression of fused silica and soda lime glass nanopillars. Significant plasticity is reported in both materials along with low-stress crystallization in soda lime glass. Chapter 6 illustrates the adaptation of the table-top laser generated flyer plate setup to shock

load microstructures. This enables the silica micropillars to be loaded with sufficiently higher stress levels and XRD investigation further reveal successful polymorphic activity under shock conditions.

Chapter 7 finally concludes this dissertation and provides possible direction for future work.

Chapter 2. Influence of Nano / Micro Sample Size on the Strain-rate Sensitivity of Plastic Flow in Tungsten

The plastic flow characteristics of body centered cubic metals, which is dominated by the motion of screw dislocations, generally exhibits strong strain rate dependence. In-situ scanning electron microscopy compression tests are performed on tungsten (W) single crystal nano and micro pillars, with diameters in the range 100-2000 nm. We demonstrate here that by reducing sample size, the strain rate sensitivity of plastic flow, including not only the yield strength but also the strain burst statistics, is reduced. It is found that the strain rate sensitivity of the flow stress scales with the sample size d as $d^{0.67}$. Statistical analysis of the strain burst size displays truncated power law scaling with a lower exponent at higher strain rate for micron size pillars. Nano size pillars (<500 nm) show near universal scaling exponent of 1.50 ± 0.07 at all applied strain rates. The strain hardening rate and deformation morphology are found not to be very sensitive to the strain rate. This external pillar sample size effect is further compared with the internal grain size in nanocrystalline W in order to guide the design of new materials by tuning the characteristic length scale (external or grain size).

2.1. Introduction

Tungsten (W) has long been of great technical interest because of its high melting point, low sputtering rate, good corrosion resistance, and high strength at high-temperatures. It is widely used in high-temperature and radiation-shielding applications, such as light bulbs, cathode-ray tube, plasma-facing components and rocket engine nozzles. In many applications and during long-term

service, the strain rate can range from the typical creep strain rate ($\approx 10^{-6}s^{-1}$) to very high strain rates ($\approx 10^{6}s^{-1}$). As a typical body centered cubic (BCC) metal, the plastic flow behavior of W generally exhibits strong strain rate sensitivity [25–27]. Thus, the influence of the strain rate on plastic flow characteristics is also an important factor in the design of W components.

The strain rate sensitivity of W is associated with the motion of screw dislocations, because their non-planar core structure leads to very slow mobility, as compared to edge dislocations [5, 7–9]. Our recent work demonstrates that the role of screw dislocations in controlling plastic flow in bcc metals can be tuned by changing the external sample size [28]. At small scales, it is easy for screw dislocations to glide out of a free surface, which can drastically reduce stored screw dislocations. Thus, the mix of stored edge and screw dislocations can be controlled by changing sample size, in direct contrast to the traditional notion of a dislocation microstructure dominated by screw dislocations in bcc metals. In addition, the high flow stress due to the size effect helps screw dislocations to overcome the high Peierls stress. This finding of size dependent screw dislocation behavior leads to the hypothesis that the strain rate sensitivity in W may also be size-dependent. This implies that even though we may not be able to change the strain rate that a W component is subjected to in service, we can design the component with a characteristic length that renders it more resilient.

This hypothesis is to some extent supported by recent experimental results. For example, recent compression tests on bcc Fe pillars shows that the strain rate sensitivity of the yield stress decreases with the reduction of sample size [29].The strain rate sensitivity parameter (m) of bcc metals has also been reported to decrease with decreasing grain size, especially in nanocrystalline metals. [30] observed that the strain rate sensitivity of ultra-fine grained W is reduced to half the value of the

large grain size W. [31] observed a decrease in the value of m from 0.04 for conventional Fe to 0.004 when the grain size of ultrafine-grained Fe was reduced to 80 nm. [32] reported similar behavior with nanocrystalline grain size for bcc Mo. They attributed this behavior to an increase in the density of mixed and edge dislocations, and the decrease in the density of screw dislocations with decreasing grain size, thereby reducing the strain rate sensitivity. This explanation is consistent with our recent findings of dislocation dynamics simulations on W single crystal nano pillars [10].

One might then wonder whether a similar trend is also observed in nano and micro scale W samples. It is interesting to contemplate if there is a critical size for the strain rate insensitivity of the yield strength. Furthermore, going beyond the yield strength, the influence of size on the strain rate dependence of other plastic flow characteristics needs to be clarified [7, 33, 34]. Firstly, strain hardening is usually a desirable behavior to avoid plastic instabilities. At small scales, there is currently a wide-ranging debate as to whether strain hardening is present for submicron single crystals under uniaxial compression. The experimental observations are summarized in Table 1 in [35] for face centered cubic (fcc) crystals and listed in Table 2.1 for bcc crystals. The combined effect of size and strain rate on the strain hardening behavior is unclear yet [36, 37], and quantitative data is still missing. Secondly, the stress-strain curve at the sub-micron scale is not smooth and exhibits significant intermittency at small scales [38–45]. Strain bursts and dislocation avalanches are widely observed at the nano- and micro-scales, and the underlying physics attract significant attention. Their statistics is found to be analogous to other non-equilibrium physical systems of vastly different spatial and temporal scales, implying the universality of the underlying physics [46]. The burst statistics of micron size BCC Mo pillar [6], fcc Au [47], and Nb pillars [48] compressed at lower strain rates ($10^{-3}s^{-1}$) are found to follow a universal power law scaling behavior. However,

it has been reported that this universal behavior is not invariant under an applied strain rate. The strain-rate effects of cross-slip-driven relaxation phenomena were first proposed and simulated in coarse-grained continuum dislocation density models by Papanikolaou et al. [49], and then more detailed simulations showed consistent effects in [43, 50]. The combined strain-rate and dislocation density effect on the burst statistics was thoroughly studied using two-dimensional discrete-dislocation dynamics (DDD) simulation [43, 50, 51]. The power law exponent is found to be influenced by the dislocation density, while different dislocation densities are expected under different applied strain rates. Recent compression tests on 2 μm Nb pillars demonstrate that the applied strain rate has a significant influence on both the burst frequency and burst size statistics, and can even lead to the intermittent-to-smooth transition of plastic flow [52, 53]. If by going smaller in size, we can reduce the strain rate dependence of yield stress, then it might be possible to observe similar trend for burst statistics. Namely, it may be possible to observe strain rate insensitivity of the burst statistics when the external size is small enough. Then, one may ask if the critical size for the strain rate insensitivity is the same as that for the yield stress.

The present work aims to answer these questions, and for the first time attempts to give a complete picture of the influence of sample size on the strain rate dependence of plastic flow in W. This includes the yield strength, the strain hardening rate, strain bursts, and dislocation avalanches. The chapter is organized as follows. In section 2.2, the experimental set up is described. Size tuned strain rate sensitivity of the yield strength and strain hardening behavior is addressed in section 2.3, followed with a discussion of the spatio-temporal intermittent plasticity in section 2.4. We then highlight the concerns surrounding FIB micromachining technique in section 2.5. The competitive role of size and strain rate is discussed in section 2.6. Concluding remarks are finally given in

section 2.7.

Table 2.1: Strain hardening (SH) data from uniaxial compression experiments on bcc single crystal micro and nanopillars. Here, ε represents strain value, T represents temperature

Material	**Crystal Orientation**	**Diameter** d (μm)	**Strain Hardening**
Mo [47]	[001]	0.20 - 0.98	Decrease with reducing d
Mo [54]	[111]	0.20 - 1.20	Similar for different d
Mo, Ta [55]	[001]	0.20 - 1.00	Presence when $\varepsilon < 5\%$, absence for large ε.
Ta [11]	[111]	0.50 - 5.00	Ta has weak SH at $25°C$, more significant SH for $d = 0.5\mu m$ at $200°C$
W [11]	[100]	0.50 - 5.00	Weak SH for $d = 5.0\mu m$, relatively larger SH for $d = 0.5\mu m$
W [55]	[001]	0.20 - 5.00	Absence when $\varepsilon < 4\%$, presence for larger ε
Nb [55]	[001]	0.20 - 5.00	More significant SH for $d = 0.2\mu m$
Nb [56]	[001]	0.20 - 0.90	More significant SH for tension than compression
Fe, Nb, and V [57]	[001]	0.20 - 5.00	Increase with decreasing d, at 23°C and -80°C
Fe [58]	[010], [011]	1.00	Increase with decreasing temperature

2.2. Experimental Setup

Cylindrical micro and nano pillars of diameters ranging from 100-2000 nm were milled out of polished (100) W single crystal (9 mm diameter and 10 mm thick), purchased from Goodfellow Corporation. Pillars were made using the Focused Ion Beam (FIB) method with a gallium ion source operating at 30 kV, keeping the pillars axis along the [001]-orientation. The sample was first polished using 600 grit and 1200 grit silicon carbide abrasive discs until they became smooth

to the naked eye. Then, they underwent a final polish using 1 μm α-alumina powder. The local roughness of polished W surfaces is insensitive to alumina particle size [59]. According to the SEM observation, the local surface roughness is far smaller than the compression scale. Care was taken for locations of pillars to avoid any visible surface defects in the SEM. Using FEI Nova 600 DualBeam (FIB/SEM), pillars were made in 3 - 4 steps to minimize the taper and beam damage, as shown in Fig. 2.1. The multiple-step pillar milling procedure began with creation of the base well and viewing window for clearance and line of sight while performing in-situ compression. This first step was carried out at currents ranging from 0.5 nA to 5 nA, depending on the pillar diameter. The following steps to shape the pillar were performed at lower currents to reduce ion beam damage to the pillar. A final cleaning step to reduce taper was implemented at extremely low currents after all intermediate diameter-decreasing steps were completed, ranging from 1 pA for the smallest (100 nm) pillars to 100 pA for the micron sized pillars. The final milling step at pA level ion currents also helps in reducing the ion-beam damaged layer from the pillar surface. For pillars of diameters 500, 1000, and 2000 nm, the aspect ratio (length/diameter) was kept around 3. However, for smaller pillars of diameter 100 and 200 nm, this ratio was around 5 because of the difficulty in minimizing the side-wall taper. The taper in the pillars was $2.0 \pm 0.5^{\circ}$ for 2000 nm and 1000 nm diameter, $2.5 \pm 0.5^{\circ}$ for 500 nm, and $3.5 \pm 0.75^{\circ}$ for 200 and 100 nm diameters. The pillar taper in this work is similar to almost all other micropillar studies using FIB manufacturing technique [60–62]. Errors in the stress and strain as large as several percent can be expected due to ignoring column taper, rounding at the top and bottom of the column, and nonplanarity and friction between the diamond punch and column top [61, 63, 64]. Some aspects of the FIB induced complication will be further discussed in section 2.5.

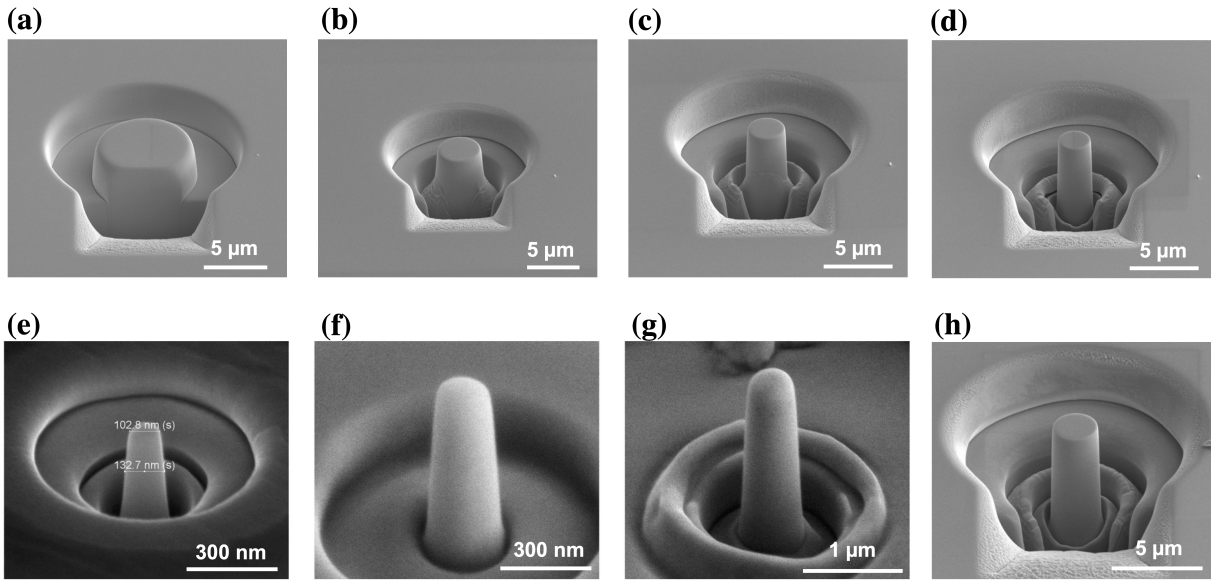

Figure 2.1: (a), (b), (c), and (d) are the SEM pictures of milling steps of a representative 2000 nm W pillar using a 4-step *in-situ* SEM FIB method. (e), (f), (g), and (h) are the SEM pictures of representative 100, 200, 500, and 2000 nm pillars respectively.

The uniaxial compression tests were performed using the Hysitron PI 85L PicoIndenter, equipped with a flat punch tip of 5 μm in diameter, inside FEI Nova 600 DualBeam (FIB/SEM). A displacement-controlled loading mode was selected for all experiments and the loading rates were chosen to achieve an applied strain rate range from 10^{-3} s^{-1} to 10^{-1} s^{-1}. The data acquisition rate was selected for each experiment based on the compression speed. Load displacement data obtained from the PicoIndenter software was converted to stress-strain plots using the measured lengths and diameters. The diameter was measured at the middle pillar section due to its tapered shape. In previous work, the maximum strain value in experiments is generally less than 20% [11, 55]. In the current work, compressions were performed for a wide range of strain values (20 % to 50 %) to give more complete information. For each size at each strain rate, 7-10 tests were carried out.

2.3. Size tuned strain rate sensitivity of flow stress

The stress-strain curves are shown in Fig. 2.2 for representative pillars at different strain rates. It clearly demonstrates that with the reduction of the sample size, the strain rate dependence changes significantly. For 2000 nm pillar, the stress-strain curves exhibit obvious strain rate effects (see Fig. 2.2a). When the pillar diameter decreases to 500 nm, the flows stress seems to be strain rate insensitive (see Fig. 2.2b).

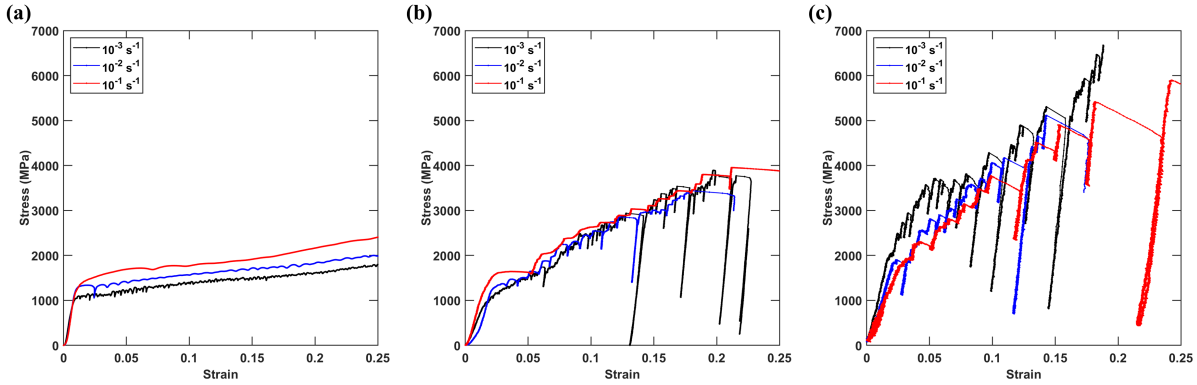

Figure 2.2: Typical engineering stress-strain curves of W pillars with diameters (a) 2000, (b) 500 and (c) 100 nm tested at different applied displacement rate of the compressor tip corresponding to strain rates of $10^{-3}, 10^{-2}$ and $10^{-1}s^{-1}$.

In the following subsections, the size-tuned strain rate sensitivity of the yield stress and strain hardening rate are further quantitatively analyzed.

2.3.1. Strain rate sensitivity of the yield strength

The yield strength of the bulk material is usually estimated as the stress value taken at 0.2% offset strain. With respect to the experimental tests at the micro and nano scale, the yield strength is generally measured at a strain value between 2% and 10% [4], to avoid the effects of initial microplasticity, misalignment, and the rounding of the tip especially in smaller diameter pillars

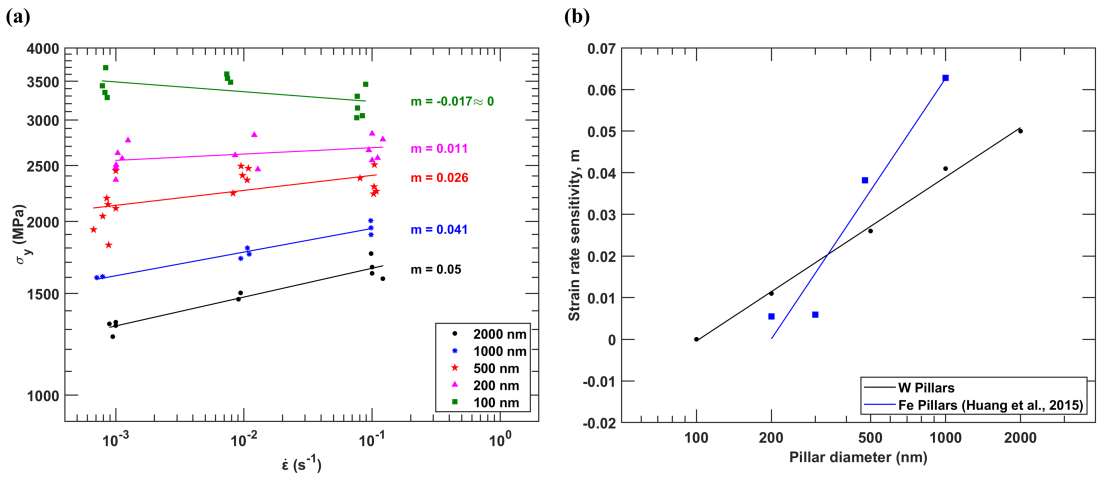

Figure 2.3: Strain rate and size dependence of the flow stress (at 8% strain), σ_y for W pillars. (a) Double logarithmic plot of flow stress, σ_y vs strain rate $\dot{\varepsilon}$ at different pillar diameters with the strain rate sensitivity parameter, m as the slope of the linear fit. (b) Semi logarithmic plot of the strain rate sensitivity parameter, m vs pillar diameter for W pillars and Fe pillars (taken from literature)

[65]. Accordingly, the stress at 8% strain is treated as the yield strength σ_y (flow stress) in this work. The yield strength data was then fitted as a function of the strain rate as, $\sigma_y = A\dot{\varepsilon}^m$, where A is the fitting constant, and $\dot{\varepsilon}$ is the applied strain rate. The strain rate sensitivity parameter m for the yield strength is given as,

$$m = \frac{\partial(\ln \sigma_y)}{\partial(\ln \dot{\varepsilon})} \tag{2.1}$$

Fig. 2.3(a) gives the yield strength as a function of the strain rate in a log-log plot. The strain rate sensitivity parameter m is obtained by fitting the slope of the corresponding data. As expected, m decreases gradually from 0.050 to 0.011 when the pillar size is decreased from 2000 to 200 nm. The 100 nm pillar shows a negative value of m ($= -0.017$). The low absolute value of this calculated negative strain rate sensitivity parameter is negligible compared to the typical scatter observed for such small pillar tests. For example, the large burst events in 100 nm, as evident in Fig. 2.2c, lead to higher scattering in the flow stress values obtained at 8% strain, compared to

larger sized pillars. Therefore, the yield strength of 100 nm pillars can be considered as strain rate insensitive, and m is close to 0. This size dependent strain rate sensitivity trend shown in Fig. 2.3(a) is consistent with other observations for Fe, where Huang et al. [29] reported a decrease in the value of m from 0.0628 to 0.0055, with a decrease in diameter from 1000 nm to 200 nm, as shown in Fig. 2.3b. Similar weak or no strain rate sensitivity of yield stress at submicron and micron scales is also observed in other BCC pillars [37, 66, 67]. A reduced m value with the decrease in sample size is also widely observed in nano-crystals [68], as summarized in section 3.

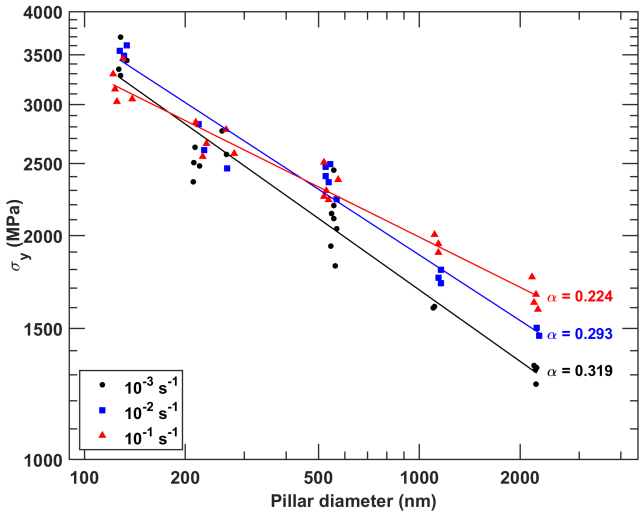

Figure 2.4: Double logarithmic plot of the flow stress, σ_y vs pillar diameter at different strain rates with size effect power law exponent, α as the slope of the linear fit.

On the other hand, the competition between the size and strain rate effects on the yield strength can also be interpreted through the strain rate dependence of the size. Based on this consideration, we alternatively plot the yield strength as a function of size at different strain rates. It is found from Fig. 2.4 that with the reduction of the sample size, the yield strengths at different strain rates start to overlap and then change their trend, due to a transition from a positive strain rate dependence to a negative one. Fig. 2.4 suggests that the size effect is more significant at lower strain rates.

Quantitatively, the size effect is described by,

$$\sigma_y = \sigma_0 + kd^{-\alpha} \tag{2.2}$$

where σ_0 is the bulk strength of the material [1], d is the characteristic length scale, k is a constant, and α is the power law exponent. As shown in Fig. 2.4, the power law exponent, α decreases from 0.319 to 0.224 with an increase in the strain rate from $10^{-3}s^{-1}$ to $10^{-1}s^{-1}$. This data is consistent with the one presented by [11], which shows a power law exponent of 0.33 at 25^oC and $10^{-3}s^{-1}$ strain rate for (100) W, using flow stress values at 2.5% strain. [5] report $0.44(\pm 0.11)$ power law exponent for flow stress at 8% strain in (100)W, whereas [55] report a value of 0.21 at 5% strain. Our data range is comparable with reported literature. Such strain rate dependent power law exponent illustrates that size effect is not an intrinsic parameter to the materials, which agree with the previous finding that the size effect exponent is sensitive to the initial structure and density of dislocations in the materials [69].

2.3.2. Strain rate dependence of the strain hardening rate (SHR)

The strain hardening rate (SHR) is calculated as the slope of the true stress-strain curve between 5% and 15% strain. This definition of SHR is similar to other studies of nanopillar compressions [60, 70]. According to the engineering stress-engineering strain curves shown in Fig. 2.2, the SHR is expected to increase with decreasing pillar diameter, which is consistent with previous studies on both fcc and bcc small size metals [66, 70]. This trend is quantitatively demonstrated in Fig. 2.5, which shows clear size dependence but weak strain rate dependence for 1000 nm and 2000 nm

[1] In the literature [11, 47], σ_0 has been taken as 0 while calculating the power law exponent α from the loglog plot of σ_y vs. d.

pillars, whereas for 100, 200 and 500 nm pillars there is no clear trend of the SHR at different strain rates. These results of size dependent SHR are similar to those reported by [11] for W pillars at 25^{o}C and 10^{-3} s^{-1} strain rate[2]. The general trend of the size dependence is attributed to the exhaustion of weak dislocation sources in smaller pillars leading to the requirement of higher stresses to activate new dislocation sources. Due to the existence of a very limited number of dislocation sources in small pillars, appreciable scatter of the data are observed in small pillars. This depends on initial concentration of dislocation sources which may be influenced by the ion damage caused by FIB milling process and can cause considerable scattering as is the case for 100, 200 and 500 nm pillars.

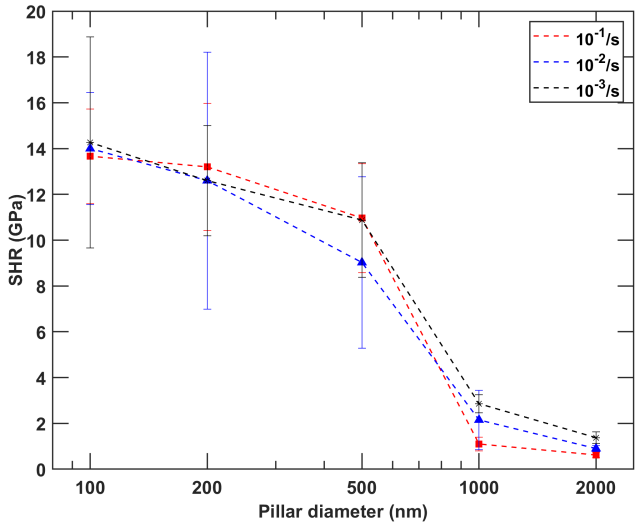

Figure 2.5: Plot of the strain hardening rate (SHR) as a function of the pillar diameter (log scale) at different strain rates.

2.4. Spatio-temporal Intermittent Plasticity

We discuss here the deformation morphology of compressed pillars. Observations of shape change during plastic deformation will be used to determine the extent of deformation localization and the

[2]Our absolute values of SHR are lower than their data, because they used engineering stress and strain data to calculate SHR.

spatial plastic instability. We will then discuss in this section the size tuned strain rate dependence of strain bursts, as such bursts reflect the extent of the temporal plastic instability.

2.4.1. Spatial scale: deformation morphology

Figure 2.6 shows post compression SEM images of representative W pillars as a function of pillar diameter and strain rate. These pillars were compressed to a strain of 20% to 25%. 2000 nm pillars show relative homogeneous deformation for all strain rates. The deformation morphology does not show significant strain rate dependence. For smaller pillars, 500 and 200 nm, the deformation is more localized at low strain rates and more homogeneous at high strain rates. At low strain rate, the deformation mainly occurs at the top and bottom region, while at high strain rate, more slip traces are also observed in the middle region of the pillar. This is consistent with our recent dislocation dynamics simulation results on the strain rate effect of the deformation behavior of W [71]. Recent work done by Song et al. [50] also supports the idea that higher strain rates correspond to less localization. Sparks et al. [53] found a clear trend of increasing delocalization with increasing strain rate in compressed Nb pillar, even when the pillar diameter reaches 2000 nm. Compared with the slip-line morphology shown in Nb pillars (bcc) [53] and Ni pillars (fcc) [72], the deformation localization extent in our W pillars is weaker.

It has been argued that the localized deformation may be attributed to the cylindrical shape of the pillar which can induce stress concentrations at the top surface. Recently, Xu et al. [73] investigated two types of pillars with conventional cylindrical shape or dog-bone shape under compression, at size scale > 2000 nm. They found that most of slip bands are initiated from the top region of the conventional cylindrical micropillars, whereas for dog-bone micropillars, slip bands begin at the gauge region and continuous slips happen. This work may lead to new ideas to eliminate the

effect of stress concentration at the top surface of cylindrical pillars on the deformation morphology. However, some local deformation features are still observed in their deformed dog-bone micropillars (such as Fig. 8 in Xu et al. [73]). Furthermore, it is unclear if the dog-bone pillar geometry would show homogenous deformation at size scales < 1000 nm. Therefore, in the current work, we chose the conventional cylindrical shape, which is widely used in most of the micropillar compression tests. This makes it be easy to compare with the available experimental results.

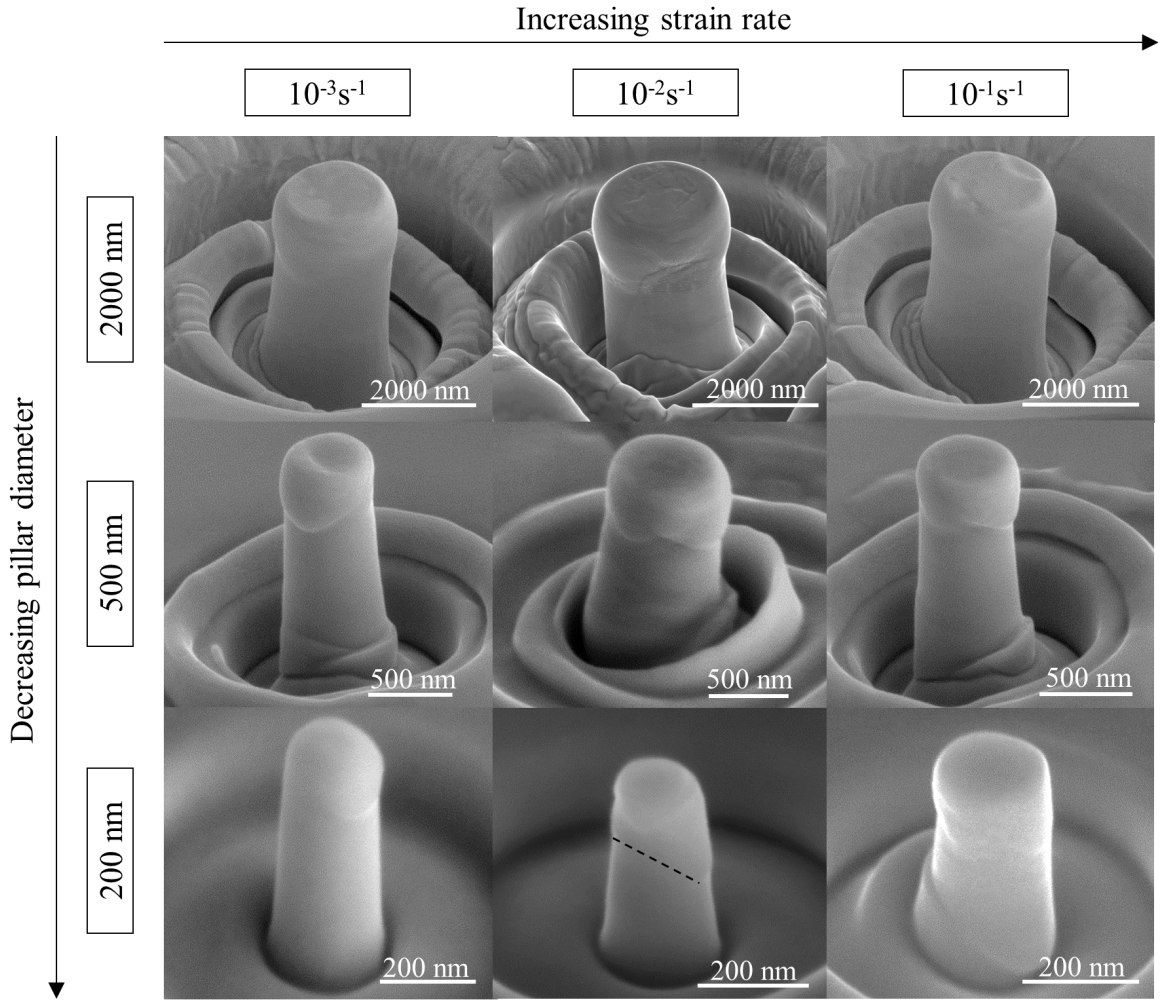

Figure 2.6: SEM images of representative post compression W pillars of diameters 2000, 500 and 200 nm, compressed at applied strain rates of $10^{-3}, 10^{-2}$ and $10^{-1}s^{-1}$. The dotted line in 200 nm pillar indicates the trace of a slip band.

2.4.2. Temporal scale: burst statistics

As evident from Figs. 2.2 and 2.7, unlike bulk single crystals with smooth stress-strain curves, smaller pillars exhibit an initial elastic region followed by an intermittent plastic region of discrete strain bursts. These plastic strain instabilities are attributed to rapid movement of dislocations when the internal strain rate becomes higher than the applied strain rate [71]. Therefore, it is expected that the strain rate will influence the observation of strain bursts.

In the following, we will first discuss the detailed method of distinguishing strain bursts from experimental data, and then address the question of burst statistics. Burst events were identified using the raw displacement time data $d(t)$ obtained from the Hysitron PI 85L PicoIndenter. This raw displacement-time evolution data are first smoothed using a low-pass filter to remove the high frequency noise, such as shown in Fig. 2.8a. The smoothed data is shifted in time to account for the filter delay and then differentiated using a MATLAB moving window function (John D'Errico, Mathworks File Exchange) to get a velocity time profile $v(t)$ of the top surface of the pillar during compression (see Fig. 2.8b). A strain burst event starting at time t_{start} and ending at time t_{end} is defined as [74–76],

$$\begin{aligned} v(t_{start}) = v(t_{end}) = v_{thr}. \\ v(t) > v_{thr}, \text{ for } t_{start} < t < t_{end} \end{aligned} \tag{2.3}$$

where v_{thr} is the threshold value of the displacement rate, which is related to the displacement rate of the compressor tip and is set higher than the displacement rate noise of individual experiments, as listed in Table 2.2. The internal strain rate $\dot{\varepsilon}_{internal}$ and the threshold strain rate $\dot{\varepsilon}_{thr}$, shown in

Fig. 2.7, are then calculated as

$$\dot{\varepsilon}_{internal} = \frac{v(t)}{h}, \quad \dot{\varepsilon}_{thr} = \frac{v_{thr}}{h} \tag{2.4}$$

where, h is the initial pillar height.

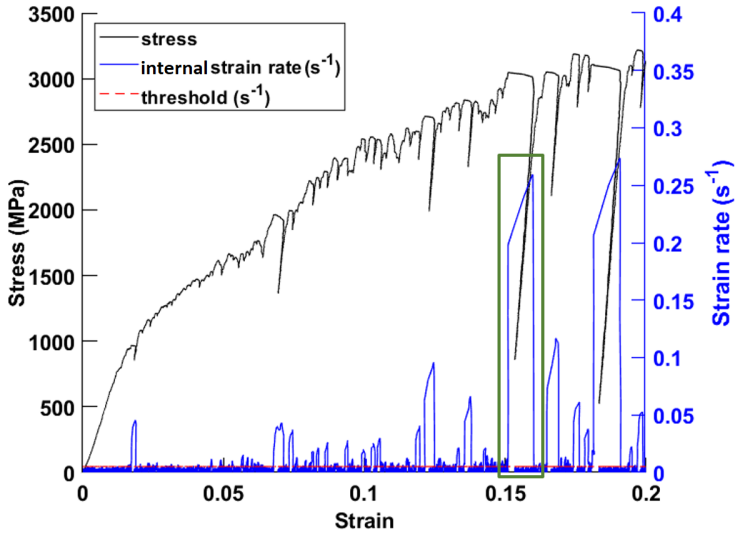

Figure 2.7: Evolution of the stress and internal strain rate during compression of a representative 500 nm pillar at an applied strain rate of $10^{-3}s^{-1}$.

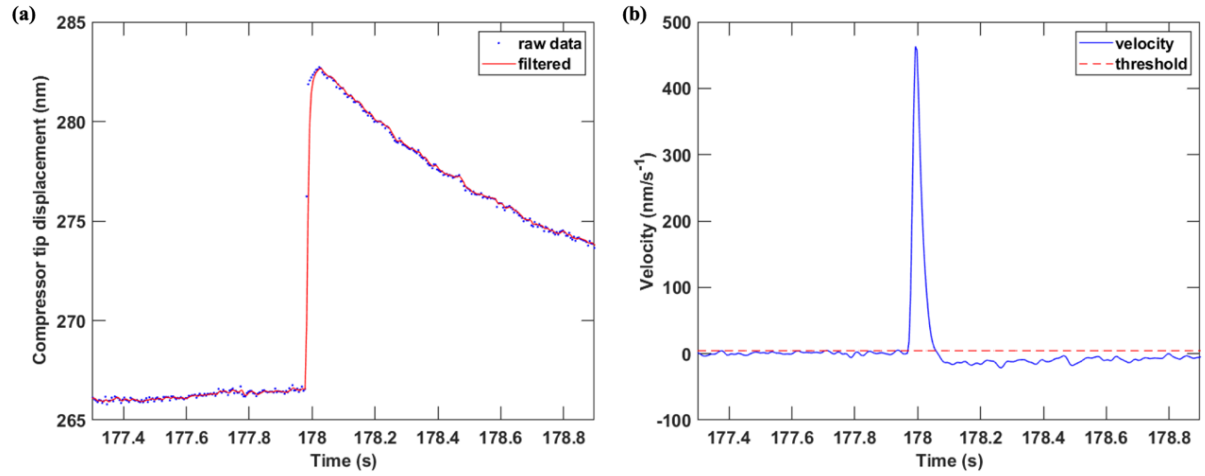

Figure 2.8: (a) Displacement-time and (b) velocity-time profiles for a single burst event, which occurred at a strain value of 0.15 (boxed in green) for the 500 nm pillar shown in Fig.2.7.

Accordingly, the strain burst size is calculated as,

$$S = d(t_{end}) - d(t_{start}) \tag{2.5}$$

Here, d and S can be any quantities related to the burst event. For example, if d is the displacement, strain, or time, then S will be displacement burst magnitude, strain burst magnitude, or burst duration. In the following, we will take the burst displacement as an example to analysis the burst statistics. The burst events are evident in the raw displacement signal (Fig. 2.8a) as jumps in the displacement magnitude located at corresponding start times, t_{start}. The burst event size computed using Eq. 2.5 was further carefully compared with the jump magnitude obtained from the displacement signal plots to ensure correct estimation of burst events.

We performed statistical analysis of the burst size by calculating the probability density function (PDF) and complementary cumulative distribution function (CCDF). PDF can clearly show whether the strain burst statistics follows the power law scaling, but it needs to introduce some artificial binning size. CCDF does not need to introduce the binning size, and can obtain the maximum resolution of the data without binning size. However, special care should be taken to analyze the power law scaling using CCDF, as discussed in detail in [75, 77]. These results of PDF and CCDF were compared with the mean-field theory (MFT) model predictions about the universal scaling behavior of bursts statistics. MFT model [75] predicts that the probability density function of burst size scales as,

$$P(S) \propto S^{-\kappa} f(S) \tag{2.6}$$

where S is the burst size, $\kappa = 1.5$, which is the universal critical exponent, and $f(x) \propto e^{-\lambda x}$ is a

scaling function to account for the truncation effect. Previous dislocation dynamics simulations [78], force-controlled compression experiments [6, 47] and displacement-controlled compression experiments [48, 79] agree with the universal value of power law exponent, κ. However, the strain rate effect is not carefully investigated in these studies. Our recent DDD simulations [77] and displacement-controlled compression experiments [52] have reported strain rate sensitivity of the power law exponent.

Fig. 2.9 shows PDF and CCDF plots of burst displacement for 1000 nm, 500 nm, and 200 nm pillars at different applied strain rates. More data are shown in the CCDF plot compared with PDF plot, because PDF shows the results with binning, while CCDF can show all the data [75, 77]. A truncated power law (TPL) distribution fit, $P(S) \propto e^{-\lambda S} S^{-\kappa}$ was obtained for each burst size data using the python Power-law package which performs a maximum likelihood estimation of the power law exponent κ and truncation factor λ [80]. λ acts as a cutoff for the power law fit of the distribution. In MFT, $P(S)$ follows the power law $S^{-\kappa}$ up to a stress dependent cutoff size, λ^{-1}. These parameters were found to be sensitive to the range of data, S_{min} and S_{max} used for fitting. Increasing the S_{min} increases the value of κ as the power law curve fitting happens on the heavy tail part i.e. the truncated part of the distribution. On the other hand, decreasing the S_{max} excludes the large burst events. Therefore, for uniformity in analysis, the value of S_{min} was chosen based on the standard deviation in displacement signal, measured during noise test of the instrument before each compression session, which was ≤ 0.5 nm. This S_{min} value was fixed for all pillars, and S_{max} was chosen as the largest burst size in each case. In this way, we were able to include all relevant burst events, from the smallest to the largest, for fitting the distribution functions.

Fig. 2.9 shows different power law exponents at different strain rates for 1000 nm pillars. Table

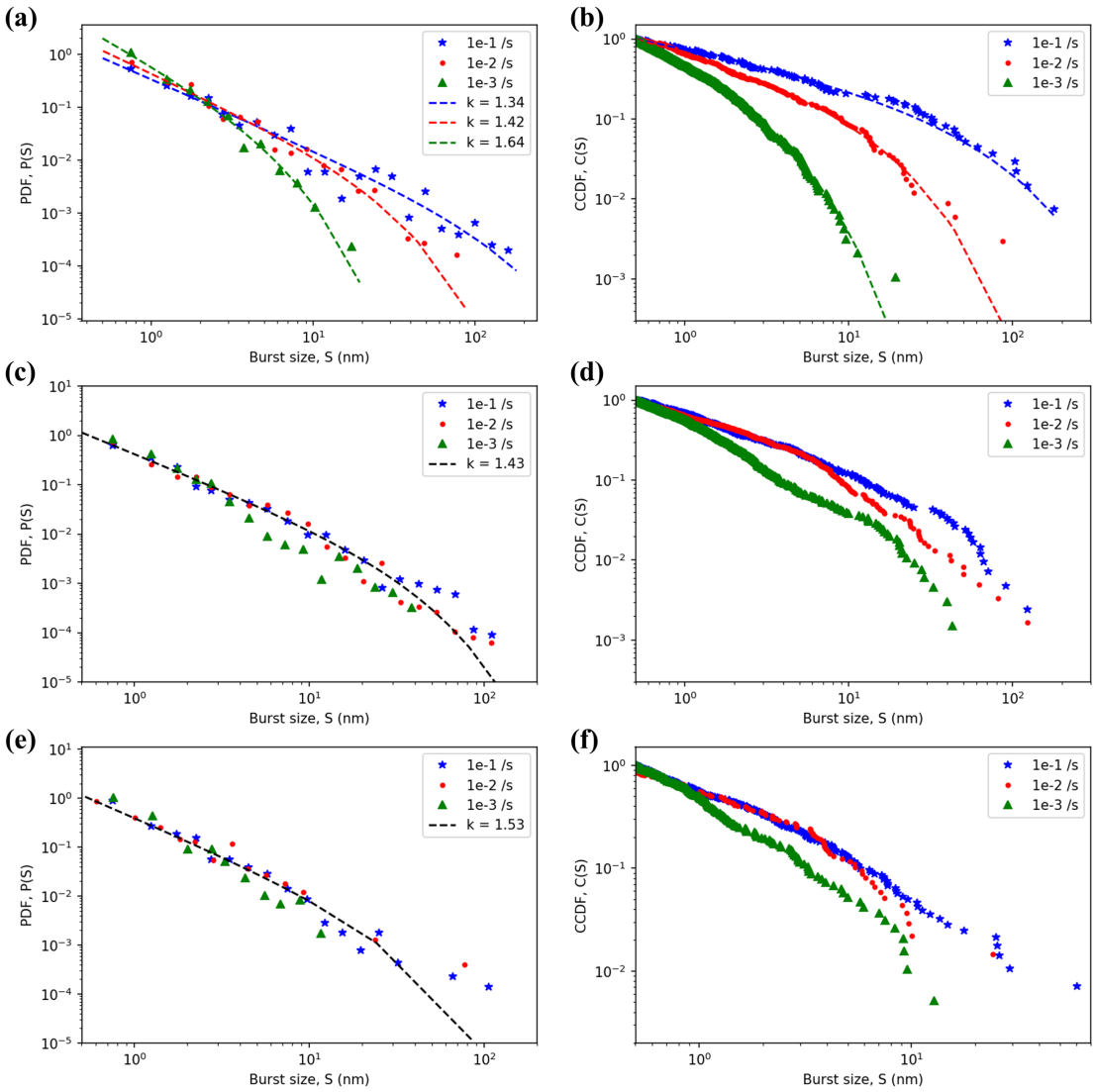

Figure 2.9: Statistical analysis of the strain burst size for 1000 nm (a-b), 500 nm (c-d), and 200 nm (e-f) W pillars at applied strain rates of $10^{-3}s^{-1}$, $10^{-2}s^{-1}$, and $10^{-1}s^{-1}$. Figures (a), (c), (e) display the probability density functions (PDFs) and figures (b), (d), (f) display the complementary cumulative distribution functions (CCDFs). Dashed lines in (a), (c) and (e) are the truncated power law fits on the PDF data obtained using the maximum likelihood estimator, where k is the power law exponent. The dashed lines in (b) are gamma functions obtained after integrating the corresponding truncated power law fit function.

2.2 shows all the parameters used and the obtained truncated power law function details for each pillar size at different applied strain rates. The exponents increase in magnitude from 1.34 to 1.64 with decreasing strain rate from 10^{-1} to $10^{-3}s^{-1}$, which is consistent with previous experimental [52] and DDD simulation results [50, 77]. However, for 500 nm and 200 nm pillars, the burst size

statistical scaling is insensitive to experimental strain rate, showing exponents of 1.43 and 1.53 respectively at all strain rates, close to the MFT model prediction of 1.5.

Table 2.2: Parameter details for fitting truncated power law functions for burst size PDF of each pillar at various strain rates

Pillar Diameter	**Displacement Rate**	**Threshold,** v_{thr}	S_{min}	**Power law exponent,** α	**Truncation factor,** λ
1000 nm	300 nm/s	400 nm/s	0.5 nm	1.34	6.33×10^{-3}
	30 nm/s	40 nm/s		1.42	4.47×10^{-2}
	3 nm/s	4 nm/s		1.64	2.44×10^{-1}
500 nm	150 nm/s	180 nm/s	0.5 nm	1.43	3.34×10^{-2}
	15 nm/s	18 nm/s			
	1.5 nm/s	3 nm/s			
200 nm	60 nm/s	120 nm/s	0.5 nm	1.53	4.33×10^{-2}
	6 nm/s	15 nm/s			
	0.6 nm/s	2 nm/s			

2.5. FIB micromachining challenges

FIB micromachining is a widely used fabrication technique for the majority of the pillar micro-compression studies. It is known to cause geometrical and material complications in the samples [55, 57, 63, 81, 82]. In the following, the geometrical complications induced by the combined effect of taper and aspect ratio is firstly discussed, followed by discussion on surface effects of ion bombardment during FIB milling.

2.5.1. Combined effect of taper and aspect ratio

It is very challenging or may even be impossible to completely remove the taper for FIB fabricated

pillars smaller than 1 μm [60, 62]. In the current work, the taper in the pillars was $2.0 \pm 0.5^{\circ}$ for 2000 nm and 1000 nm diameter, $2.5 \pm 0.5^{\circ}$ for 500 nm, and $3.5 \pm 0.75^{\circ}$ for 200 and 100 nm diameters. For pillars of diameters 500, 1000, and 2000 nm, the aspect ratio (length/diameter) was kept around 3. However, for smaller pillars of diameter 100 and 200 nm, this ratio was around 5 because of the difficulty in minimizing the side-wall taper. These ranges of taper and aspect ratio are well within the range of numerous similar-sized pillar compression studies with tapers around $2^{\circ} - 5^{\circ}$ and aspect ratio of $3 - 5$ [55, 57, 60–62].

In the following, the geometrical effects associated with taper and aspect ratio on the measured mechanical response will be analyzed. As shown in Fig. 2.10 (a), the top, middle, and bottom radius of the tapered pillar is r_t, r_m, and r_b, respectively. The aspect ratio $\alpha = h/(2r_m) = h/(r_t + r_b)$, where h is the pillar height, θ is the taper angle, $r_t = r_m(1 - \alpha tan\theta)$, $r_b = r_m(1 + \alpha tan\theta)$. The material parameters are: shear modulus μ = 161 GPa, Poisson's ratio ν = 0.28, elastic modulus $E = 2\mu(1 + \nu)$, and a tangent modulus E_t is used to represent the plastic response after reaching the yield stress of the material, σ_{my}. The stress in the horizontal cross section at y is

$$\widehat{\sigma}(y) = \frac{F}{\pi(r_b - ytan\theta)^2} \tag{2.7}$$

where F is the applied force, a superposed$\widehat{\ }$is used to represent variables corresponding to an infinitely small region centered at a specific horizontal cross section.

If the infinitely small region, corresponding to the horizontal cross section at y, is subjected to elastic deformation, the corresponding strain $\widehat{\varepsilon}(y) = \widehat{\sigma}(y)/E$, while if it is in plastic deformation, the corresponding strain $\widehat{\varepsilon}(y) = \widehat{\sigma}(y)/E_t + (1 - E/E_t)\varepsilon_{\text{mp}}$. Here, $\varepsilon_{\text{mp}} = \sigma_{\text{my}}/E$. For the tapered pillar, the plastically deforming zone will propagate down the post axis. The critical position

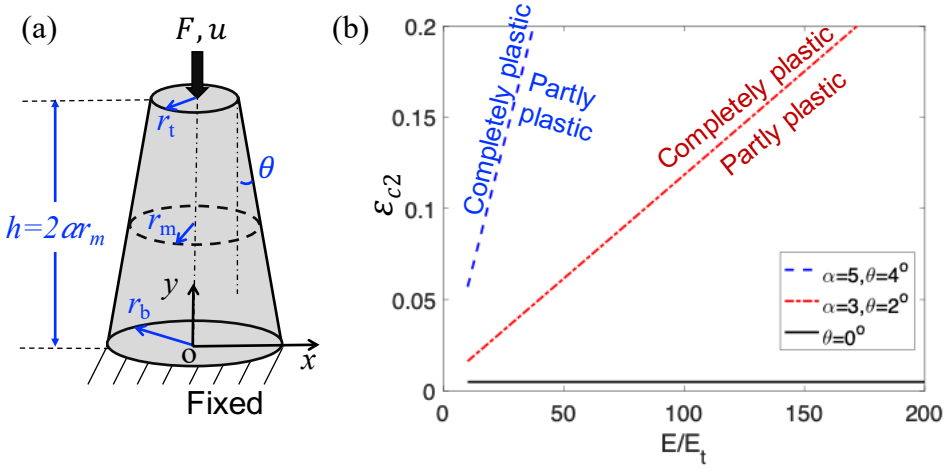

Figure 2.10: (a) Schematic showing the considered pillar with taper and key parameters, (b) The critical strain ε_{c2} as a function of the ratio between elastic modulus E and tangent modulus E_t, when the engineering strain ε is higher than ε_{c2}, the pillar completely enters the plastic deformation stage

is expressed using y_p, and plastic deformation occurs if $y > y_p$. One can easily find $y_p = (r_b - \sqrt{F/(\sigma_{\text{my}}\pi)})/tan\theta$. Upon integration of strain $\widehat{\varepsilon}(y)$ along y, one obtains the displacement u of the top surface,

$$u = \begin{cases} \frac{Fh}{E\pi r_b r_t} & \text{If} \quad F \leqslant \sigma_{\text{my}}\pi r_t^2 \\ \frac{F}{\pi(r_b - y_p tan\theta)}\left(\frac{y_p}{Er_b} + \frac{h-y_p}{E_t r_t}\right) + (1-\frac{E}{E_t})\frac{\sigma_{\text{my}}}{E}(h-y_p) & \text{If} \quad \sigma_{\text{my}}\pi r_t^2 < F < \sigma_{\text{my}}\pi r_b^2 \\ \frac{Fh}{E_t\pi r_b r_t} + (1-\frac{E}{E_t})\frac{\sigma_{\text{my}}}{E}h & \text{If} \quad F \geqslant \sigma_{\text{my}}\pi r_b^2 \end{cases} \tag{2.8}$$

In the experiments, the engineering strain ε is generally calculated as u/h, and the engineering stress σ is calculated by dividing the force with the area of the middle cross section, $\sigma = F/(\pi r_m^2)$.

According to Eq. 2.8, the relation between σ and ε is,

$$\sigma = \begin{cases} \frac{1}{1-p^2} E\varepsilon & \text{If} \quad \varepsilon \leqslant \varepsilon_{c1} \\ \sigma_{\text{my}} \left(\frac{-1+\frac{E}{E_t}+\sqrt{\frac{2}{1/p+1}(1-\frac{E}{E_t})+\frac{2E\varepsilon}{\sigma_{\text{my}}}(\frac{E}{E_t}\frac{1}{1/p-1}-\frac{1}{1/p+1})}}{\frac{E}{E_t}\frac{1}{1-p}-\frac{1}{1+p}} \right)^2 & \text{If} \quad \varepsilon_{c1} < \varepsilon < \varepsilon_{c2} \\ (1-p^2)[\sigma_{\text{my}} + E_t(\varepsilon - \frac{\sigma_{\text{my}}}{E})] & \text{If} \quad \varepsilon \geqslant \varepsilon_{c2} \end{cases} \tag{2.9}$$

$$p = \alpha tan\theta \tag{2.10}$$

$$\varepsilon_{c1} = \frac{\sigma_{\text{my}}(1-p)}{E(1+p)} \tag{2.11}$$

$$\varepsilon_{c2} = \frac{\sigma_{\text{my}}}{E}\left(1 + \frac{E}{E_t}\frac{2}{(\frac{1}{p}-1)}\right) \tag{2.12}$$

where p can be considered as a geometrical factor reflecting the combined geometrical effect of taper and aspect ratio on the mechanical response. ε_{c1} and ε_{c2} are critical strains. The pillar with a taper will deform elastically when $\varepsilon \leqslant \varepsilon_{c1}$, and then completely enters the plastic deformation stage only when $\varepsilon \geqslant \varepsilon_{c2}$. It can be found from Eq. 2.9 that the taper contributes to an increase of the apparent elastic modulus to $1/(1-p^2)$ times the corresponding values without taper during the complete elastic deformation ($\varepsilon \leqslant \varepsilon_{c1}$) , and a decrease of the apparent tangent modulus to $1-p^2$ times the corresponding values without taper during the complete plastic deformation ($\varepsilon \geqslant \varepsilon_{c2}$) regime. For the experimentally considered 100 nm pillar, $\alpha = 5$ and $\theta = 4°$, so $p = 0.35$, $1/(1-p^2) = 1.14$, $1-p^2 = 0.88$. For large samples ($\geqslant 500$ nm), $\alpha = 3$ and $\theta = 2°$, so $p = 0.105$, $1/(1-p^2) = 1.01$, $1-p^2 = 0.99$. Therefore, in these two regimes ($\varepsilon \leqslant \varepsilon_{c1}$, and $\varepsilon \geqslant \varepsilon_{c2}$), the error in the calculated stress induced by the taper is within $\sim 14\%$ for small pillar, and within $\sim 1\%$ for large pillar.

Due to the existence of taper, a significant percentage of the deformation corresponds to the partially plastic deformation regime ($\varepsilon_{c1} < \varepsilon < \varepsilon_{c2}$). Taking $\sigma_{\text{my}} = 2$GPa as an example, the value of ε_{c2} as a function of E/E_t is given in Fig. 2.10 (b). The measured SHR at strain range of $5\% \sim 15\%$ in experiments may belong to the partly plastic deformation regime and the complete plastic deformation regime. In the partly plastic deformation regime, the relation between engineering stress and engineering strain is not linear due to taper. The error of the calculated stress in this regime depends on not only the geometrical factor p, but also the modulus ratio E/E_t.

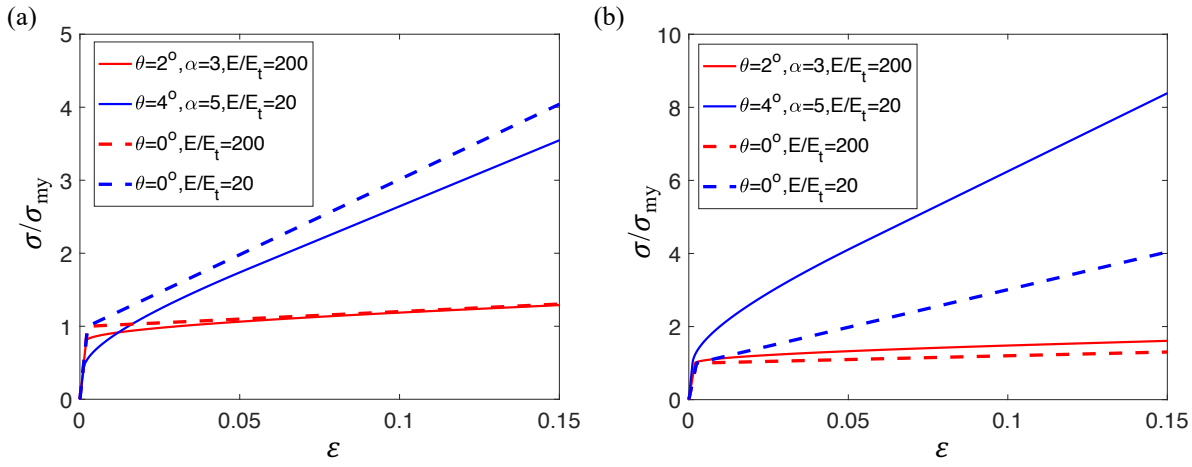

Figure 2.11: (a) Engineering strain and engineering stress calculated using the middle cross section area, (b) Engineering strain and engineering stress calculated using the top surface area. θ is taper angle, α is aspect ratio, E is elastic modulus, E_t is tangent modulus, σ_{my} is the material yield stress

In order to clearly show the effect of taper on the SHR, according to our experiments, two extreme cases are considered: 100 nm pillar with $\theta = 4°$, $\alpha = 5$, $E/E_t \sim 20$, and 2000 nm pillar with $\theta = 2°$, $\alpha = 3$, $E/E_t \sim 200$. The results are compared with the corresponding pillar without taper. It can be observed from Fig. 2.11(a) that the taper does not significantly change the strain hardening rate. The yield strength for the considered small pillars is underestimated due to the taper by about 12%. Considering the appreciable scatter of the mechanical response in small pillar, this error is acceptable. For the large pillars, much smaller error is observed. Note that in Zhang et

al.'s results [63], a much more significant taper effect on SHR is reported. This is possible because in their work, the pillar's top surface area is used to calculate the stress, instead of the middle cross-section area. As shown in Fig. 2.11(b), if the top area is used, the strain hardening rate is much more sensitive to the taper, compared with Fig. 2.11(a) where middle cross-section area is used. In addition, higher flow stress is observed in Fig. 2.11(b) for the pillar with taper, which is consistent with Zhang et al.'s results. The analysis above also shows the importance of using the middle cross-section area of the tapered pillar. In the current work, when the strain rate sensitivity is considered, the effect of taper for the same-sized pillar is similar under different strain rates. Therefore, the taper is expected to have weak influence on the strain rate sensitivity.

2.5.2. Other FIB effects

It is well known that FIB milling can introduce surface defects leading to material complication, which can potentially influence the strain hardening rate at the nanometer size scale, due to the Ga layer being deposited on the surface. As the ratio of surface area to volume increases with smaller sized pillars, the relative scale of the ion irradiated layer increases, causing its effects to become more noticeable. As a result, the dislocation density, due to higher density in the Ga damage layer rather than the single crystal W, also increases. Thus one may be concerned that the higher stress found in smaller pillars is not due to exhaustion of dislocations sources but rather this layer impeding motion of dislocation. However, postmortem images of 100 and 200 nm pillars show clear slip bands ejecting from the pillar, so for the considered case, Ga damage layer is not a strong barrier of dislocation motion. [83] also demonstrated using *in-situ* TEM compression that dislocations are not impeded by the Ga layer, and many other researchers [64, 84] report such mechanical annealing (dislocations escaping during compression) as well. Furthermore, the last milling step for ≤ 500

nm sized pillars is performed at $1-10$ pA levels, which help in cleaning the Ga layer away without causing any additional damage.

While it is unlikely that the increased relative size of the damaged layer causes the higher observed stress at small scale by being the load bearing element or causing dislocation pileup [60], it is possible that the abundance of dislocation sources from FIB milling lowers the strength required to initiate plasticity [81], resulting in the observed size effect in FIB manufactured pillar [85]. [81] demonstrated that chemically etched defect-free pillars with no surface damage, in contrast to FIB manufactured pillars, have yield strength independent of sample size close to theoretical strength. This is also observed by [86]. In addition, pillars created without Ga+ and containing initial dislocations exhibit a size effect akin to those fabricated by FIB [86, 87]. Therefore, size effect is thought to depend on initial, nonzero, dislocation density rather than the manufacturing method. For dislocation-free sample, plasticity is controlled by the dislocation nucleation process, while for the samples with initial dislocations, the plasticity is mainly dominated by the collective behaviors of the dislocations, which is the focus of the current work. Therefore, we did not try to eliminate the initial dislocations, and focused on the study of pillars with initial dislocations.

2.6. The competition between size and strain rate effects

The size effect of small-scaled single crystal has attracted attentions for several decades. However, how to take the advantage of size effect to real application is still an open question. The most straightforward way of introducing size effect in large-scaled component is through designing nano-to-micro lattice structures or grain-size engineering [88, 89]. However, there is limited efforts to investigate the difference between the response associated with the external size and the internal size, and which one is better to be chosen as the degree of design freedom to control the

specific mechanical properties of materials. Therefore, it is interesting to compare the size effect in single crystal and polycrystals. Even though there is difference in the deformation mechanism of single crystal and polycrystals, if one ignores the complicated dislocation-grain boundary interaction mechanism and simplifies the grain boundary as impenetrable boundary, each grain can be considered as a coated single crystal, whose coating layer is impenetrable to dislocations. From this point of view, comparing single crystals in terms of polycrystals can be simplified as discussing the coating effect. Most of the previous work focuses on the initial yield behavior and leads to the popular notion that "smaller is stronger". It is of interest then to understand the size effect on the strain rate sensitivity, because the strain rate sensitivity is used as a fingerprint for the thermodynamics and kinetics of plastic deformation [7, 90], a criterion to assess the possibility of superplastic behavior [91] and deformation localization [88, 92].

The experimental observations presented in this work demonstrate that with the reduction of the sample size, the strain rate sensitivity of the flow stress decreases. Similar size dependent strain rate sensitivity is consistent with previous observations in polycrystal W by grain-size engineering [88]. Considering that pillar diameters and grain size are typical examples of the external size and internal size, it will be very interesting to compare their roles in influencing the strain rate sensitivity. A quantitative comparison between the effect of sample size and grain size is given in Fig. 2.12 and Table 2.3. Note that increasing d in Fig. 2.12 does not means that it has to be close to the bulk behavior. Because d corresponds to the grain size of a polycrystal or the sample size of a single crystal, higher d means coarser grain or larger single crystal. Therefore, the discussion on the external sample size effect only considers the single crystal, without any grain boundary hardening effect, which is different from the typical bulk sample. Fig. 2.12 shows that the reduction extent of

strain rate sensitivity with decreasing sample size is even more significant in the single crystals by tuning external size, compared with polycrystals with changing grain size[3].

The difference of the role of the grain size and external size is also manifested by the different trend of strain rate hardening, as shown in Table 2.3. The SHR decreases with reducing sample size in polycrystals W [88], but increases with reducing external size in W pillars (see Fig. 2.2 and Fig. 2.5). In ultra fine grained polycrystalline W compression experiments by [93], flow softening ($SHR < 0$) is observed at higher applied strain rates ($> 10^3 s^{-1}$), which implies the occurrence of flow localization. According to Considere-Hart criterion, the propensity of a metal for flow localization under compression α can be estimated as $\alpha = (-SHR/\sigma_y - 1)/m$ [4]. Higher α corresponds to greater tendency for flow localization due to the suppression of the stabilizing mechanisms of strain and strain rate hardening. This simple relation implies that the size dependent strain hardening rate, yield stress σ_y, and strain rate sensitivity m all contribute to a more localized deformation for reduced grain size. In our W single-crystal pillars, we also observed more significant flow localization in smaller pillars, but it cannot be well explained by Considere-Hart criterion. In small-scale single crystals, the size dependence of plasticity is generally controlled by the limited number of dislocation sources due to surface annihilation, which is different from the grain boundary effect in polycrystal. Higher SHR values in smaller pillars do not imply more trapped dislocations, as described by the well-known Taylor relation, but is a manifestation of the gradual destruction of weak dislocation sources. We find that the smaller the pillar size, the more scarce are activated

[3]Note that the strain rate in our experiments ranges from 10^{-3} to 10^{-1}. The experimental data for ultrafine-grained and nanocrystalline bcc metals are obtained at strain rates that range from 10^{-3} to 10^{3}. Further dedicated efforts may be required to expand the strain rate regime that can be considered during small scale tests.

[4]In other studies, $\alpha = (SHR/\sigma_y - 1)/m$ [93]. This discrepancy is because we use σ_y to express the absolute value of yield stress, which is described as a negative value under compression in other studies. For compression experiments, the flow will be unstable when $\alpha > 0$. This is possible at high temperature and / or high applied strain rates when there is flow softening, i.e. $SHR < 0$

Table 2.3: Size dependent plastic flow of W single crystal pillars and polycrystals. Here, d is sample size or grain size

	Single crystal pillar	Polycrystal
Strain rate sensitivity m	m$\propto d^{0.67}$	$m \propto d^{0.31}$
Strain hardening rate SHR	Increased SHR for small d	Reduced SHR for small d [88]
Localization	More localized for small d	More localized for small d

dislocation sources, and the more significant is flow localization.

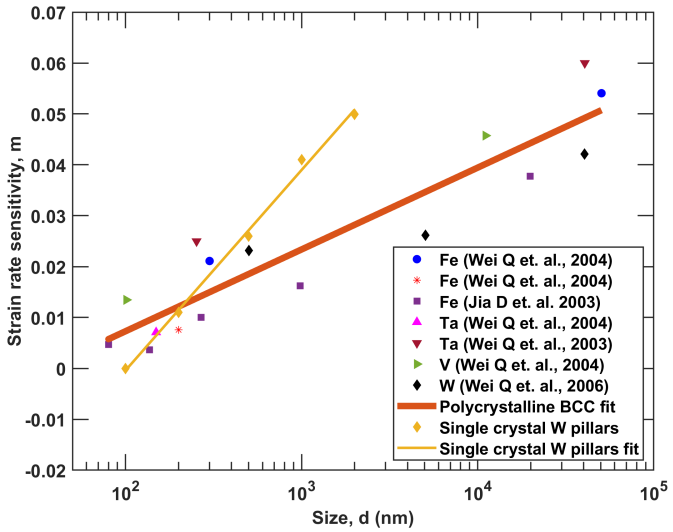

Figure 2.12: Strain rate sensitivity parameter, m, for polycrystalline ultra fine grained BCC metals from literature [30, 68, 92, 94] and our single crystal W, as function of d, which is the grain size for polycrystal or sample size for single crystal.

The influence of sample size on the strain rate sensitivity is generally explained based on the following model [68, 95]. The rate equation for plastic flow controlled by thermal fluctuations is written using an Arrhenius equation [96],

$$\dot{\gamma} = \dot{\gamma}_0 \exp\left(\frac{-\Delta G(\tau^*)}{k_B T}\right) \tag{2.13}$$

where $\dot{\gamma}$ and $\dot{\gamma}_0$ are the shear strain rate and pre-exponential factor involved in the thermal activation,

respectively. k_B is Boltzmann constant, T is temperature, ΔG is the activation energy as a function of the shear stress τ^*, which is defined as the applied shear stress minus the athermal internal stress stemming from long-range interactions. The activation volume V is then defined as the derivative of the activation enthalpy with respect to stress [97],

$$V = -\left[\frac{\partial \Delta H(\tau)}{\partial \tau}\right]_T = k_B T \left(\frac{\partial ln\dot{\gamma}}{\partial \tau}\right)_T = k_B T \left(\frac{\partial ln\dot{\gamma}}{\tau \partial ln\tau}\right)_T = \frac{k_B T}{\tau m} \tag{2.14}$$

Accordingly, $m = k_B T/(\tau V)$. This implies that the strain rate sensitivity is weaker when the applied stress is higher and/or the activation volume is larger. For BCC crystal, the activation volume can be calculated as $V = b^2 l$ [95]. Where b is the Burgers vector magnitude, l is the effective activation distance. At low homologous temperature($T < 0.3T_m$, T_m is melting point), screw dislocations are the dominant carriers of plastic deformation. The motion of the dislocation has to overcome Peierls lattice resistance, the barrier due to the interactions with forest dislocations, and the line tension barrier related to grain boundaries or free surfaces. Accordingly, $l^{-1} = l_p^{-1} + l_g^{-1} + l_f^{-1}$. Here, l_p is associated with the kink-pair mechanism as the critical span between two kinks [98], which is only about several tens of Burgers vectors. l_g is related with grain size or sample size d, l_f is associated with dislocation forest interaction mechanism, and is estimated as $1/\sqrt{\rho}$. When d is much larger than l_g (about several nanometers), and ρ is much smaller than about $10^{17} m^{-2}$, l is dominated by l_p. This critical span has an inverse square root dependence on applied stress, however, it levels off at very high applied critical stress. This critical stress level can be calculated by the screw dislocation mobility law [7, 10, 99]. For screw dislocations, the kink nucleation and motion is of the form

$$v_s = \frac{\tau_{rss} b}{A_s T} \exp\left(-\frac{\Delta G}{k_b T}\right) \tag{2.15}$$

where, v_s is the screw dislocation velocity, τ_{rss} is the resolved shear stress, b is the Burgers vector magnitude, A_s is the phonon drag constant, T is the test temperature, and ΔG is the Gibbs free energy for the kink pair nucleation. ΔG is given as [100],

$$\begin{aligned} \Delta G &= \Delta H - T\Delta S \\ &= \Delta H_0 \left[\left(1 - \left(\frac{\tau^\alpha}{\tau_P} \right)^p \right)^q - \frac{T}{T_c} \right] \end{aligned} \tag{2.16}$$

where ΔH_0 is the activation enthalpy at zero stress, p and q are two constants reflecting the shape of the Peierls potential, which can be determined by atomistic simulations and experimental data, τ_P is Peierls stress, τ^α is an effective resolved shear stress (rss), which takes non-Schmid effects into account [7, 26, 99]. The critical yield stress for W is calculated to be 900 MPa at 298 K, by setting $\Delta G = 0$ in above equations. Since the stress levels obtained in compression experiments for nanocrystalline W and our single crystal W micro and nanopillars are much higher than this critical value, we can conclude that the activation length, l (and hence V) quickly levels off and yield stress, τ becomes the controlling factor for m, where m decreases with increasing τ. This successfully explains the reduced strain rate sensitivity in bcc metals with smaller characteristic lengths.

The comparison of the strain rate sensitivity influenced by grain size and external size can be analyzed as follows. According to the Hall-Patch relation, in polycrystal W, the flow stress $\sigma_y - \sigma_0$ is proportional to $d^{-0.5}$. According to our results shown in Fig. 2.4, $\sigma_y \propto d^{-0.3}$ in single crystal W pillars. If one only considers the power law term of σ_y with respect to d, the flow stress seems to vary more significantly with respect to grain size, compared with external size. However, the value of σ_0 actually influences the power law exponent, which is not clearly discussed in previous work on polycrystalline W. Thus, based on the power law term alone, the extent of the size dependence

of flow stress remains uncertain. Experimental work reported that the flow stresses are 1.5 GPa and $2.5 \sim 3$ GPa, when grain sizes are 500 nm and 170 nm, respectively [101]. According to these limited data reported in the literature and compared with our data in Fig. 2.4, the size dependence of the flow stress in polycrystal W is close to that in single crystal W pillars. Therefore, the effect of flow stress may contribute to similar size dependence of the strain rate sensitivity in polycrystals. In polycrystals, the pile up effect of dislocations around the grain boundary will reduce the mean free path of the dislocation, compared with the free boundary condition in single crystal, so the value of l_g is expected to be smaller in polycrystals. If all other characteristic lengths are the same, the activation volume is expected to be smaller in polycrystals, and the strain rate sensitivity value should be higher. This is consistent with the small size regime (< 200 nm) shown in Fig. 2.12. However, this model cannot adequately explain the more significant size dependent strain rate sensitivity in single crystals, compared with that in polycrystals, as shown in Fig. 2.12 for size > 200 nm.

According to our recent dislocation dynamics simulation results [10], with the reduction of the sample size, the role of thermally activated screw dislocation motion gradually decreases. On one hand, the fraction of screw dislocations decreases sharply with the reduction of sample size due to the inability of small samples to store screw dislocations. Similar lower amount of screw dislocation fraction is also observed in nano-crystalline bcc Mo with the reduction of grain size [32]. On the other hand, the very high flow stress in small scale bcc crystals, together with the image force effect, can greatly enhance the mobility of screw dislocations. Therefore, the strain rate sensitivity model on the basis of a single thermally activated process cannot explain the whole story. The relative lower strain rate sensitivity in polycrystals for sizes ranging from about 300 nm to 2000 nm may be

because that the strong pile-up effect around the grain boundary on the screw dislocation activities prevails over the effect due to dislocation annihilation from free surface in singe crystal for this size regime. This analysis highlights further work that is required for fully understanding the similarity and differences between tuning external and internal sizes.

Going beyond the strain rate sensitivity of the yield stress, our experimental results also demonstrate that the strain rate dependence of dislocation avalanches statistics also become weaker for smaller pillars. This trend is also observed in our recent dislocation dynamics simulations [71]. For large sample size (such as 1000 nm in Fig.2.9), increasing strain rate gradually leads to a reduction of the power law scaling due to an increasingly smaller fraction of small avalanches [53], because a higher strain rate requires more correlated dislocation motion, and some small avalanches may merge at higher strain rates. Through comparing the role of screw dislocation and non-screw dislocations on dislocation avalanches at different strain rates, we find that screw dislocation activities are more important at high strain rates compared with low strain rates [71]. As the external size gets smaller, it becomes more and more difficult to store many screw dislocations and achieve highly correlated dislocation motion, even at very high strain rates. Therefore, the strain rate effect on dislocation avalanches is gradually overwhelmed by the size effect.

2.7. Summary and conclusions

In summary, systematic uniaxial in-situ SEM compression experiments were carried out on W micro and nano sized cylindrical pillars. For the first time, we reveal the size effect on the complete picture of the strain-rate-controlled plastic flow behavior in W. We included not only the yield strength, but also the strain hardening rate, and the strain burst statistics. The main finding is that with the reduction of the sample size, the strain rate sensitivity gradually decreases. The critical size of the

strain rate insensitivity is around 500 nm for all considered plastic flow behaviors. Such size-tuned strain rate sensitivity is also consistent with our previous finding on the size-tuned temperature sensitivity [10]. This external size effect is further compared with the internal grain-size effect with respect to the strain rate sensitivity, strain hardening behavior and flow localization. This leads to the possibility of obtaining better mechanical behavior at corresponding strain rate and temperature conditions by designing the external and internal size of the W component.

Additional conclusions of the present chapter are:

1. The flow stress, obtained at 8% strain, exhibits size and strain rate dependence. The power law exponent (α) for size effect decreases with increasing applied strain rate. The strain rate sensitivity parameter (m) decreases with decreasing pillar sizes, implying that the rate of loading has very little effect on the nano size pillars (< 500 nm).

2. The scaling exponent for strain burst statistics are loading rate dependent for micron size pillars (> 1000 nm), where the power law exponent decrease with an increase in the applied loading rate. Nano size pillars (< 500 nm) show near universal power law scaling ($\kappa = 1.50 \pm 0.07$) of strain bursts statistics, independent of the applied loading rate, supporting the observation that nano size pillars are insensitive to strain rates.

3. Micron size W pillars are shown to have homogeneous plastic deformation at all strain rates, whereas nano size pillars exhibit relatively more localized plastic deformation at low strain rates and homogeneous deformation at high strain rates.

Chapter 3. Fracture Toughness of Single Crystal Tungsten at the Nano- to Micrometer Scale

In previous chapter we showed at the sub-micron size scale, the role of screw dislocations for plastic behavior is found to be less dominant and their mobility is greatly enhanced. This can potentially lead to a size dependent fracture behavior. In this chapter, in-situ SEM bending tests on notched cantilevers of single crystal tungsten are reported. The beams were fabricated via FIB milling and had uncracked ligament sizes < 1 μm. We demonstrate here that the entire crack growth in notched tungsten beam is stable and ductile in nature at sub-micron size scale and room temperature. Elastic-plastic fracture mechanics approach is applied and crack resistance ($J - \Delta a$) curves are obtained. The critical J values measured as per ASTM guidelines do not satisfy the size requirements. Hence, a sample size dependent or "conditional" fracture toughness (K_Q) value of 11.76 ± 0.56 MPa m$^{1/2}$ is measured for the {110}<100> crack system in our submicron sized beams. This is lower than macroscopic fracture toughness value (K_{IC}) of single crystal tungsten for the same crack orientation (20.2 ± 5.5 MPa m$^{1/2}$). Alternatively, the K values obtained from the maximum J values of the resistance curve reach the macroscale K_{IC} range. The corresponding crack growth is around 200 - 300 nm which is similar to the crack growth value at critical J in larger specimen (>3 μm) reported in literature. Hence, the sample size at sub micron scale is too small to obtain the size independent material property of fracture toughness. Such sample size dependent fracture behavior is attributed to the large plastic zone ahead of the crack tip which engulfs the entire beam thickness. This is due to enhanced dislocation nucleation and mobility at the submicron scales in tungsten single crystal and the role of edge and mixed dislocations, dominating over screw

dislocations.

3.1. Introduction

The brittleness of tungsten at low temperature is a longstanding challenge that limits its wide application. Therefore, continuous efforts have been put to uncover the physical origin of its brittleness [102–104]. The Ductile-Brittle-Transition (DBT) of tungsten is generally believed to be controlled either by dislocation mobility or by the nucleation of dislocation [105]. In tungsten, the non-planar core structure of screw dislocation leads to high Peierls stress, which is difficult to be fully overcome by thermal activation alone at low temperature. As a result, high flow stress is required to drive the motion of screw dislocation through kink-pair mechanism. The activation energy for the process controlling the DBT (about 1.05eV) is found to be close to the activation energy for double-kink formation. This implies that screw dislocation mobility controls the DBT [106–108]. On the other hand, the availability of dislocation sources is also found to have an important influence on the cleavage resistance stress [109], supporting the idea that the lack of active dislocation sources prevents dislocation emission from effectively shielding the crack.

When the length scale of the material is decreased to submicron scales, both dislocation nucleation and motion exhibit different features from that of bulk counterparts. From the nucleation perspective, it is widely accepted that the number of dislocation sources are very scarce at small scales, implying more brittle behavior. However, from the dislocation motion perspective, the contribution of screw dislocation is found to decrease at small scales [10, 110]. In uniaxial compression experiments, as the sample size was decreased below 500 nm, the storage capacity of screw dislocations in the deformed pillars was significantly reduced due to significant surface annihilation effect. Furthermore, the motion of edge and mixed dislocations also play an important

role in the plastic deformation [10, 110, 111]. Since there is a significant enhancement in the yield strength of most crystalline materials due to the size effect at such small scales [4, 5], it is easier for dislocations to overcome the high Peierls stress. This raises a tantalizing possibility that perhaps one could optimize both strength and toughness in BCC metals at low temperature, below their DBT temperature. This would be especially interesting for tungsten whose yield strength increases more than triple from 1000 MPa to 3500 MPa when the characteristic length of its samples is reduced from few micrometers down to 100 nm [88, 111].

Fracture toughness behavior of tungsten has been studied extensively at the macro scale [102–104, 112–114] and it is known that {100} plane is the preferred cleavage plane for tungsten single crystals at room temperature, like most BCC metals. The secondary cleavage plane, {110} shows significantly higher fracture toughness at room temperature. There is additional anisotropy with respect to the crack propagation direction where <110> direction is the easier one compared to <100>. Consequently, a crack oriented as {100}<110> has lower and {110} <100> has the higher fracture toughness values at room temperature. Initially, such strong anisotropy was explained based on the lack of favorably oriented glide systems in {110} planes [115]. This justified the results of room temperature tests but could not hold at 77 K where {100} <110> and {110} <110> crack systems show similar toughness values. Hence, dislocation activity was ruled out as the possible origin of the fracture anisotropy in tungsten [114]. Via atomistic simulations coupled with continuum finite elements on BCC single crystal, Kohlhoff et al. [116] put forth the effect of lattice trapping where a crack remains trapped in its position beyond the Griffith value (K_G). They attributed the toughness anisotropy behavior to the presence of four easy crack propagation directions at 45º to the tough direction on {100} planes compared to one easy direction orthogonal

to the tough direction on {110} planes. It remains to be uncovered if such anisotropy exists at nano and micro size scales, and whether different crack orientations exhibit similar behaviors at small scales.

A limited number of fracture experiments on micron sized samples of tungsten single crystals have been reported in literature, as summarized in Table 3.1. On one hand, Ast et al. [117] reported size dependent fracture toughness of {100}<100> oriented crack in tungsten, where it decreases from 7.0 to 1.5 MPa $m^{1/2}$ as the initial uncracked ligament size is reduced from 28.5 μm to 500 nm. They attributed this decrease in toughness to the increase in local yield strength at smaller scales. This led to an absence of plasticity for 500 nm and 1 μm beams, and the toughness value followed the Griffith prediction for pure brittle failure. On the other hand, the smallest uncracked ligament size investigated for {110} cleavage plane is 35.2 μm by Bohnert et al. [118] (Table 3.1), and no results have been reported in the literature at submicron beams. One might then wonder if size effect in toughness can also be observed for {110} crack plane. It is interesting to contemplate if {110} crack plane can still show higher crack resistance than {100} planes at size scale of 500 nm – 1.0 μm, in consistence with their macro behavior. The present chapter aims to address the fracture behavior of tungsten at such size scales by performing in-situ SEM bending experiments on micro-cantilevers with notches along the {110} planes.

3.2. Experimental Procedures

Micro-cantilever beams were milled on the edge of polished single crystal tungsten samples via Focused Ion Beam (FIB) technique, with a gallium ion source operating at 30 kV. Using FEI Nova 600 DualBeam (FIB/SEM), beams were made in 4-5 steps as shown in Fig. 3.1. The sample edge was first sharpened (Fig. 3.1(a)) at 20nA Ga+ current and “fixed-beam” like structures were milled

Table 3.1: Fracture toughness data at room temperature from micro cantilever bending experiments on bcc tungsten single crystal samples. Results from macro scale experiments at room temperature for the corresponding crack systems are also shown for comparison.

Crack plane and propagation direction	**Uncracked ligament size** (μm)	**Fracture Toughness (MPa m$^{1/2}$)**	**Macro scale Fracture Toughness** [112]
{100}<100> [119]	2.1	12.5	6.2 ± 1.7
{100}<100> [117]	$2.9 - 28.5$	7.0	8.7 ± 2.5
{100}<100> [117]	$0.6 - 1.8$	$1.5 - 2.5$	8.7 ± 2.5
{100}<100> [120]	$3.5 - 4.0$	11.2	8.7 ± 2.5
{110}<110> [118]	35.2	13.3	12.9 ± 2.1
{110}<100> (Present Study)	$0.5 - 1.0$	$11.9 - 12.5$	20.5 ± 5.5
{110}<112> (Present Study)	$0.5 - 1.2$	$10.76 - 11.37$	–

at 5nA (Fig. 3.1(b)). The longitudinal direction of the beams was kept along <110> so that {110} <100> and {110} <112> crack systems were tested for fracture toughness. The following steps to cut and shape the beams were performed at currents ranging from 1nA to 100pA (Fig. 3.1(c)). The cantilevers were notched using a 2-step process at 10pA and 1pA currents, at a distance of 1.5 μm from the support. Fig. 3.1(d) shows the SEM image of a representative beam. A schematic of the beam along with the dimensions of the investigated samples are shown in Fig. 3.1(e). We have labelled the beams by their uncracked ligament length, $W'(= W - a_0)$ of values 500 nm and 1.0 μm. In this chapter, the “beam size" term is referred to W'.

Notch milling is of principal importance when it comes to fracture toughness determination. Majority of the published work either uses a side or top milling approach in line mode FIB. Side-milling results in an unequal notch depth on both sides of the beam and if milled for a longer time results in a rounded notch tip. Top-milling causes curtaining artifacts on the beam sides in the crack plane and would also lead to maximum Ga ion-beam damage at the notch tip. These

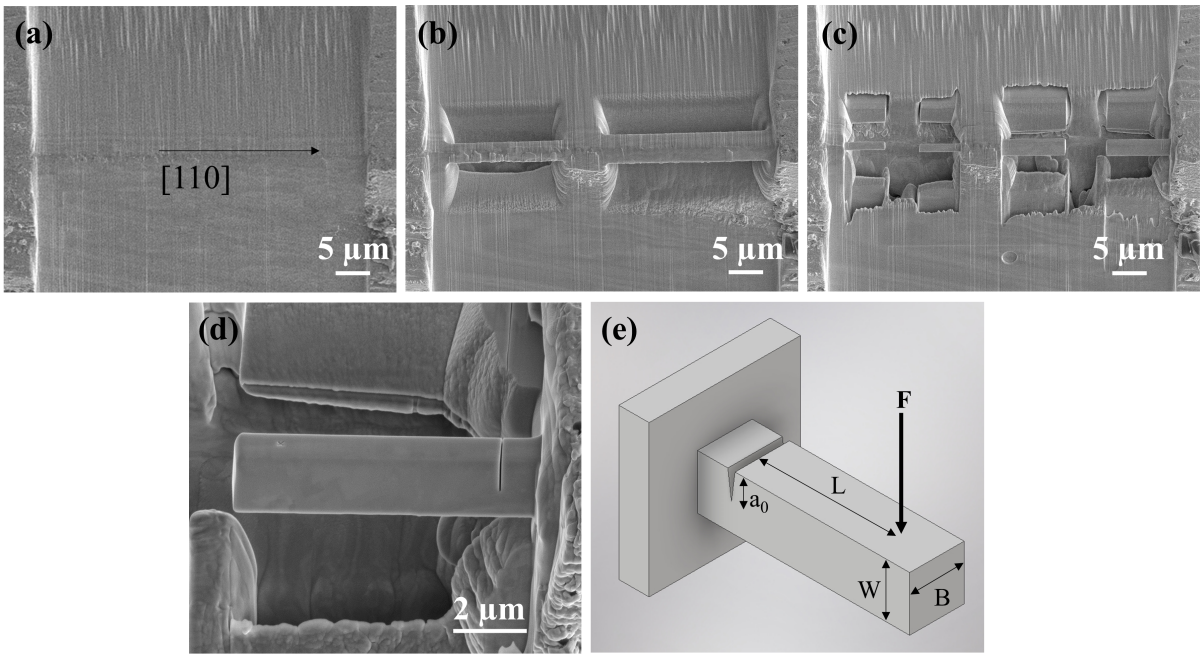

Figure 3.1: FIB fabrication steps for W microcantilever beams. (a-c) FIB milling steps for the cantilever beams. (d) An SEM image of representative 1 μm beam. (e) Schematic of the notched cantilever beam loading.

issues can lead to overestimation [121, 122] of the fracture toughness. In order to overcome these limitations, we employed a combination of both methods where an initial notch was made using side-milling at 10 pA as a first step and then the notch tip was sharpened using top-milling at 1 pA, as shown in Fig. 3.2(a). Notches were improved via testing repeatedly of tilt angles to ensure uniform notch depth through the cantilever thickness and ion-beam deflection from milling the notch. Angles were incrementally increased starting from 2° (Fig. 3.2(a)). Cantilever samples were then inspected from both sides to check notch depth on each surface. Initial cross-sections of notches with equal notch depth on front and back surfaces had a non-linear shape, mainly caused by ion beam deflection. Milling depth was increased by 2 times, then 4 times to move the location of the deflection from somewhere within the cantilever to eventually past it, at which point the ion beam no longer deflects, and tilt angle was then decreased slightly. Both parameters (tilt and depth)

were adjusted such that the final cross sections of the notch show a flat, thin notch of 30 nm width (Fig 3.2(b)), taking about 1-2 hours to mill for each sample. Subsequent 1pA top milling results in a final notch tip diameter of 16-18 nm diameter. This last step lasted for only about 10 seconds and hence the ion-beam damage to the notch tip was negligible. The final dimensions of the notched samples are given in Table 3.2.

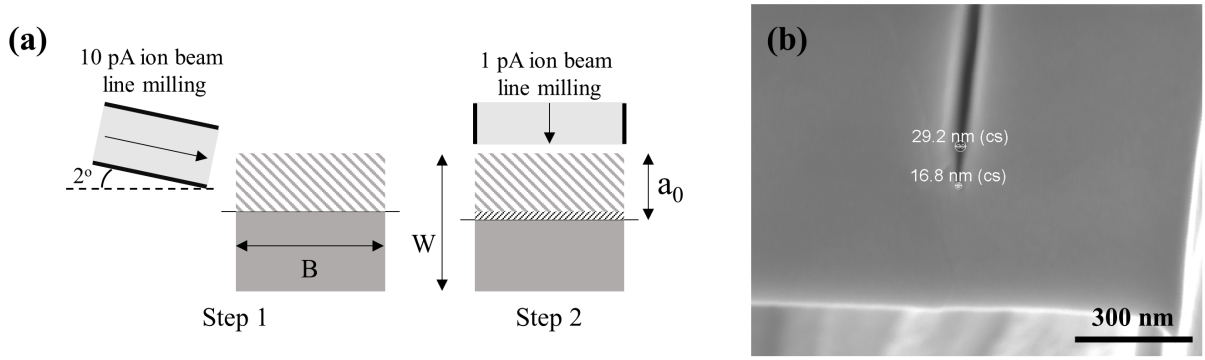

Figure 3.2: (a) The notch milling steps on the cross-section view of the crack plane, where step 1 consists of side milling and step 2 consists of top milling at 10 pA and 1 pA ion current, respectively. (b) SEM image of a 500 nm cantilever beam showing final notch tip diameter of 16.8 nm.

The in-situ loading of beams were performed using Bruker PI 85L PicoIndenter, equipped with a cono-spherical tip of 400 nm radius, inside FEI Nova 600 DualBeam (FIB/SEM). By using a rounded tip, the indentation into the beam was greatly reduced and prevented the sliding of the tip at large displacements. Several cycles of loading-unloading experiments were carried out to increase loads and individual tests were stopped once the compressor tip started to slip on the beam surface due to large inclination. The loading steps lead to crack propagation and the unloading steps were necessary for the measurement of this crack extension from the increasing cantilever compliance [118, 119]. A displacement-controlled loading mode was selected for all experiments and the loading/unloading rates were set at 10 nm/s for all specimens.

Table 3.2: Final dimensions of the tungsten samples taken from the SEM images. Dimension designations are based on the schematic shown in Fig. 1(e).

S. No.	Orientation	$L/W/B/a_0$ (μm)	$W' = W - a_0$(μm)
Sample 1-1	{110}<100>	3.02 / 0.91 / 0.53 / 0.45	0.46
Sample 1-2	{110}<100>	3.10 / 1.03 / 0.54 / 0.42	0.61
Sample 2-1	{110}<100>	6.01 / 1.79 / 1.05 / 0.89	0.90
Sample 2-2	{110}<100>	6.01 / 1.79 / 1.05 / 0.83	0.96
Sample 3	{110} <112>	3.02 / 0.87 / 0.56 / 0.43	0.44
Sample 4	{110} <112>	6.01 / 1.81 / 1.05 / 0.61	1.20

3.3. Experimental results and analysis

3.3.1. Force - displacement curves

Typical force-displacement curves for the notched micro-cantilever samples under bending are shown in Fig. 3.3. The unloading contact stiffness values at each unloading cycle are superimposed. The plots show initial elastic behavior during which there is no decrease in the stiffness. Thereafter the stiffness starts to decrease slowly and then rapidly along with decrease in force. The decrease in stiffness is indicative of crack growth initiation, which happened around the 5th unloading cycle. However, the crack extension is not visible in the SEM video recordings (supplementary material) of the bending tests until 10-15 unloading cycles are reached for each sample. One such example is shown in Fig. 3.4. This is because SEM can only show the front surface of the beam and in all cases the initial crack growth occurred away from the front surface, as discussed later.

3.3.2. Analysis of crack growth

The SEM images of crack surfaces of the cantilevers post-bending is shown in Fig. 3.5. As evident in the images, the crack surface is dimpled and irregular, suggesting the stable nature of crack

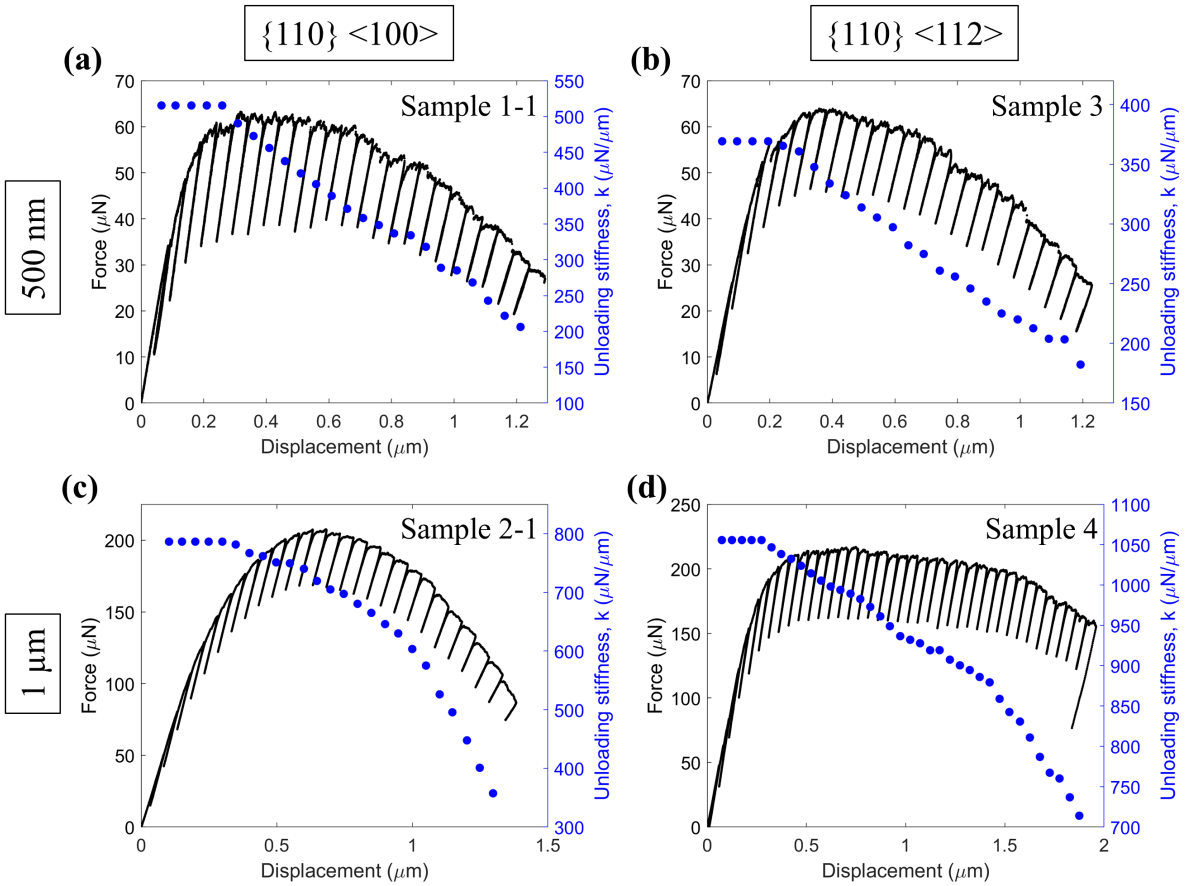

Figure 3.3: Force displacement curves along with unloading contact stiffness for (a) 500 nm and (b) 1 μm $(W - a_0)$ notched cantilevers. The initiation of crack growth is marked with dashed lines.

growth during the entire experiment. To analyze this stability, the raw displacement data was filtered and then differentiated using a MATLAB moving window function (John D'Errico, Mathworks File Exchange) to obtain the indenter tip displacement rate profile, shown for sample 1-1 and 1-2 in Fig. 3.6. Spikes in displacement rate profiles are observed which can be due to coalescence of microcracks as well as dislocation avalanches typically observed during deformation of crystalline materials at submicron scales [41]. Consequently, 500 nm beam (Fig. 3.6(a)) shows larger number of these velocity jumps than the 1 μm beam (Fig. 3.6(b)). No catastrophic cleavage fracture was observed, and the tests were stopped when the compressor tip started to slip from the beam surface due to its large inclination.

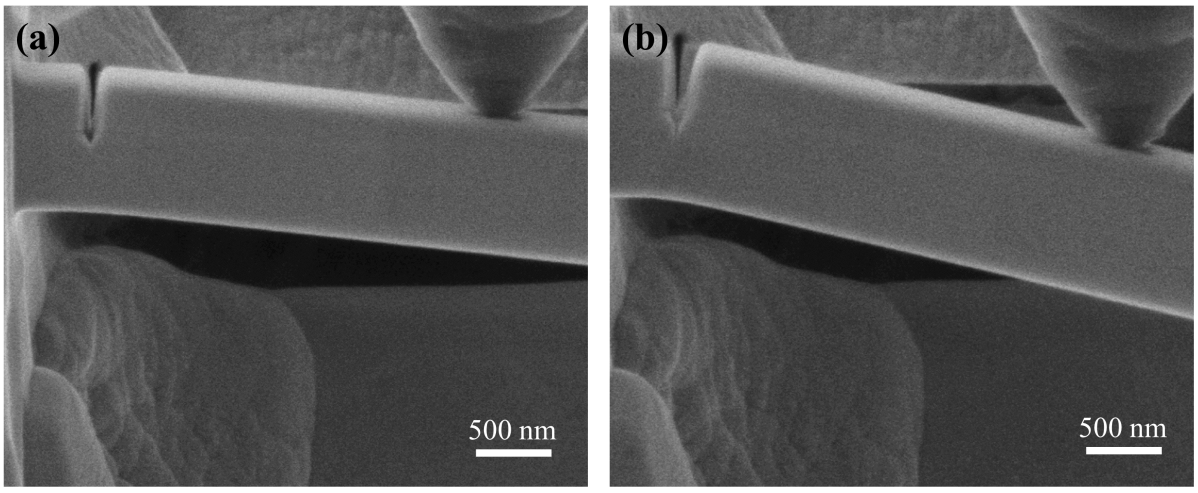

Figure 3.4: Snapshots during the in-situ SEM compression video of the 500nm beam (Sample 1-1) after (a) 5th unloading cycle where unloading stiffness first starts to decrease, and crack initiation takes place, and (b) 12th unloading cycle where crack extension becomes evident visually for the first time.

3.3.3. Analysis of fracture toughness

To determine the stress intensity factor from the experimental data, Linear Elastic Fracture Mechanics (LEFM) is initially applied to get a conditional value, Kq, LEFM. According to ASTM E399 [123],

$$K_{q,LEFM} = \frac{F_q L}{BW^{3/2}} f\left(\frac{a}{W}\right) \tag{3.1}$$

where F_q is the force determined at 95% construction line deviation from the initial linear-elastic loading, and the other parameters are defined in Fig. 3.1(e). The geometrical factor $f\left(\frac{a}{W}\right)$ was obtained via linear elastic FEM simulations using contour integral method for our sample geometries. This method is described in detail by Iqbal et al. [124]. Using the specimen dimensions measured from SEM images (Table 3.2), the obtained values for $K_{q,LEFM}$ are listed in Table 3.3. These values are not the final fracture toughness values as the plastic zone size around the crack tip needs to be evaluated and should satisfy the small-scale yielding condition in order for LEFM results to be

valid.

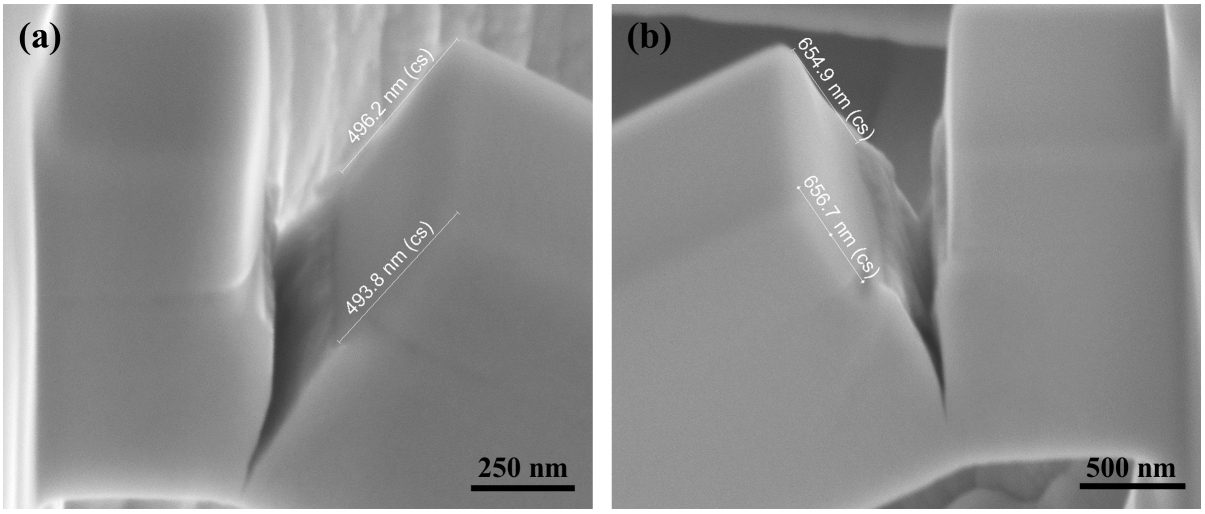

Figure 3.5: SEM images of the (a) 500 nm and (b) 1 μm cantilevers near the crack region taken from post-bending experiments.

The plastic zone size around the crack tip is given as [125],

$$r_p = \frac{1}{3\pi}\left(\frac{K_{IC}}{\sigma_{ys}}\right)^2 \tag{3.2}$$

where K_{IC} is the fracture toughness and σ_{ys} is the yield stress of the material. Due to the well-known size effect, the yield stress of single crystal tungsten can increase dramatically with decreasing size scale. By performing compression experiments on submicron pillar of tungsten with axial direction of <100>, Srivastava et al. [111] have shown that the yield stress can increase to 3500 MPa for 100 nm diameter pillars, compared to 900 MPa at macro scale [126]. Therefore, the plastic zone size (equation 3.2) would be much smaller at the size scales investigated in the present study. Considering the lowest measured $K_{IC} = 10.8$ MPa m$^{1/2}$ for {110} crack plane [112] and yield stress for 500 nm pillars, $\sigma_{ys} = 2000$ MPa, the smallest plastic zone size, r_p obtained using equation 3.2 is 3.09 μm. This value is larger than all the cross-sectional dimensions of our specimens and

one would expect some plastic flow activity near the crack tip. Ast et al. [117] and Bohnert et al. [118] observed slip lines on the side surface around the crack plane in the tungsten cantilevers of size 2.9 – 28.5 μm and 30 μm, respectively. This indicates that the plastic zone is large enough to reach far away from the crack tip on to the beam surface.

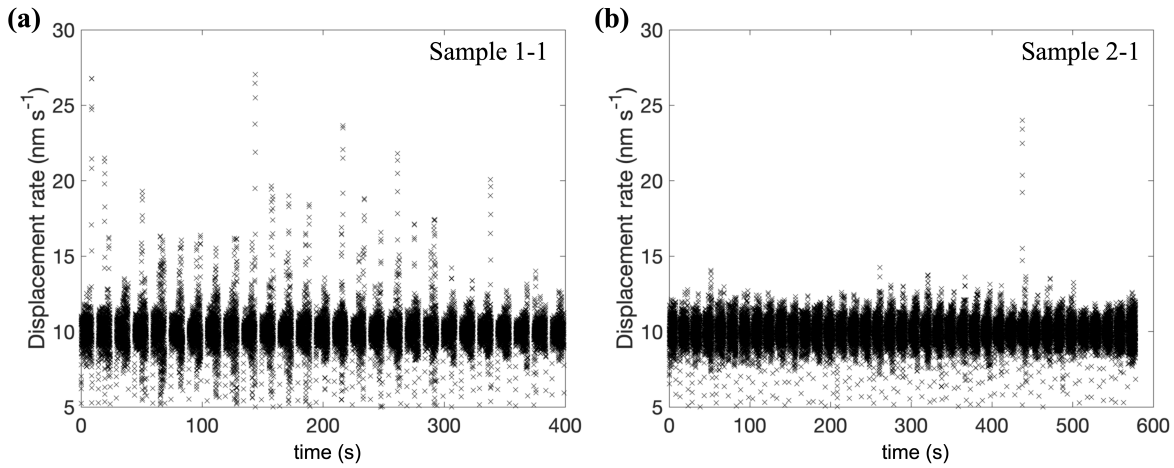

Figure 3.6: Displacement rates of the indenter tip obtained from the raw displacement data for (a) sample 1-1 and (b) sample 2-1.

The analysis above indicates that LEFM is not applicable here as the beam dimensions should be at least larger than $25r_p$ to satisfy the small-scale yielding condition [125]. The $K_{q,LEFM}$ values obtained via Eq. 3.1 then serve as the lower limit for the fracture toughness value and Elastic Plastic Fracture Mechanics (EPFM) technique of crack resistance curve needs to be employed. The crack resistance method used here follows ASTM E1820 [127], which shows J-integral can be calculated as,

$$\begin{aligned} J_i &= J_{\text{elastic, i}} + J_{\text{plastic, i}} \\ J_i &= \frac{K_{q,LEFM}^2(1-\nu^2)}{E} + \left[J_{\text{plastic, i-1}} + \frac{2(A_{\text{plastic, i}} - A_{\text{plastic, i-1}})}{B(W-a_{i-1})}\right]\left[1 - \frac{a_i - a_{i-1}}{W - a_{i-1}}\right] \end{aligned} \tag{3.3}$$

Here, E is the Young's modulus and ν is the Poisson's ratio. 'i' denotes the unloading sequence.

$K_{q,LEFM}$ is obtained from Eq. 3.1 using $F_{q,i}$ at the start of each loading cycle and geometrical factor, $f\left(\frac{a_i}{W}\right)$ which depends on the growing ratio of $\frac{a_i}{W}$. $A_{plastic,i}$ is the area under force-displacement curve excluding the elastic component in the i^{th} unloading. The crack length, a_i at the end of i^{th} unloading is calculated from the cantilever compliance, as described in [118, 119, 127, 128]. This growing crack length was compared with the SEM images obtained during the compression experiments, when the crack length was large enough to be measured in SEM, as shown in Fig. 3.7. It is very challenging to measure crack length at every unloading cycle via in-situ SEM images due to limited resolution as the crack increment is often on the order of nanometers after each loading/unloading sequence. There is expected difference between the two at the corresponding unloading sequence as the SEM images show crack length only on the front surface of the beam and the compliance method estimates the average crack length over the entire width [128]. The crack growth may occur early along certain parts of the crack edge compared to other parts and directly affect the measured compliance of the beam. Under plane strain conditions, the crack is prone to propagate faster in the center of the beam. As a result, the crack extension values measured from SEM images at the end of each loading sequence tend to initially fall behind the values obtained via cantilever compliance. Thicker the beam, more time it would take for the SEM measured crack growth to catch up to the compliance measured one (Fig. 3.7).

Figure 3.8 shows the evaluated crack-resistance ($J - \Delta a$) curve for the 500 nm and 1 μm cantilevers. These curves are very similar to the ones obtained for macroscopic samples. For comparison, a representative macroscopic sample result can be seen in Appendix A-9 of ASTM E1820 [127]. In order to obtain the conditional J value (J_Q) from the crack resistance curves, as per ASTM E1820, the first step is to draw blunting lines of slope $2\sigma_Y$, shown as dashed black lines in

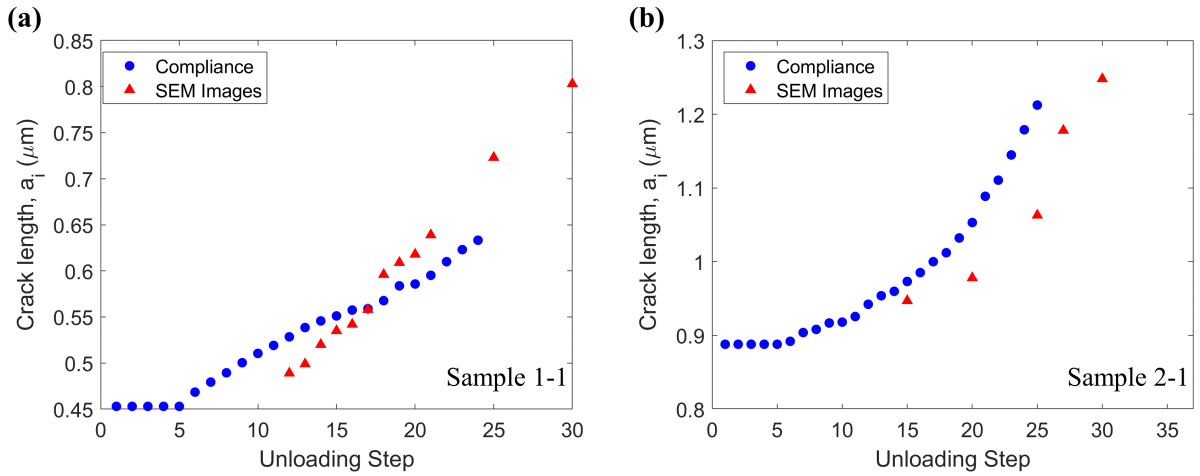

Figure 3.7: Comparison of crack growth values obtained from the increasing compliance method with the ones measured via SEM images, for (a) sample 1-1 and (b) sample 2-1.

Fig. 3.8. The yield stress (σ_Y) values used here are 2000 MPa and 1600 MPa for 500 nm and 1 μm cantilevers, respectively. These values are taken from the micropillar compression experiments of single crystal tungsten [111]. The next step is to shift the blunting line by a 0.2 mm offset in crack extension, which is not possible for the micro cantilever beams. As a result, two different methods for our size scales to determine the critical J value, J_Q from literature have been employed. In method 1, the blunting line offset is calculated as 0.5 CTOD (crack tip opening displacement) as described in [118, 128], and its intersection with the crack resistance curve is taken as J_Q (method 1), shown as dashed green lines in Fig. 3.8. The CTOD was measured from the video snapshot of the SEM recorded at the beginning of the unloading cycle when the first drop in stiffness was observed (Fig. 3.4(a)). The CTOD values thus obtained are 11 ± 4 nm for 500 nm samples and 16 $\pm$ 3 nm for 1 μm samples. The crack growth (Δa) values at this J_Q were <100 nm. For method 2, Ast et al. [117, 120] used an arbitrary crack extension length of 200 nm as the abscissa for J_Q. They showed that the ion damage due to the FIB milling at 30 kV and 1nA caused amorphization of the single crystal tungsten up to 30 nm depth, whereas dislocations were generated up to 250 nm

depth. Since notches were made at much lower current range of 1-10 pA in our samples, the ion affected depth is expected to be well below 100 nm. Therefore, we chose an abscissa of 100 nm for J_Q (method 2) in our case, shown as dotted black lines in Fig. 3.8.

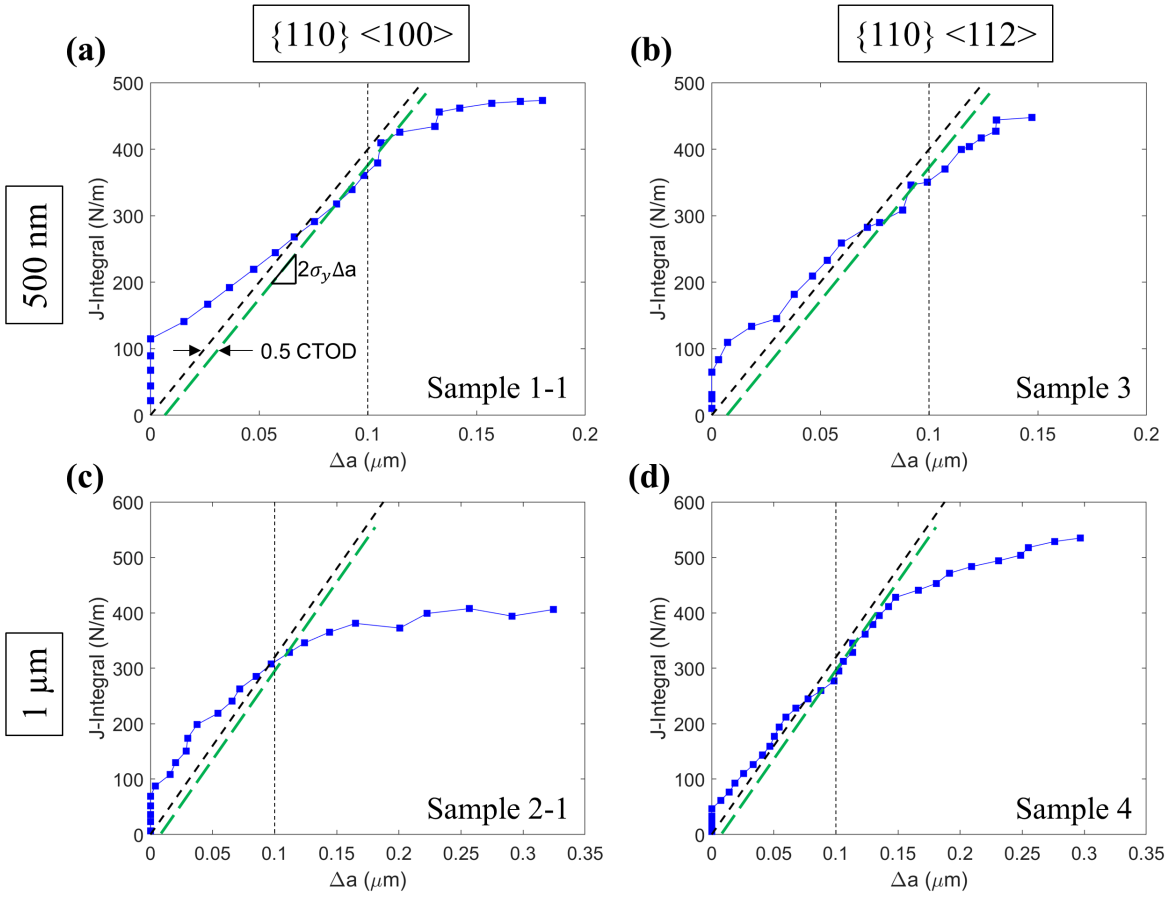

Figure 3.8: Crack resistance $(J - \Delta a)$ curves for 500 nm and 1 μm cantilevers of (100) and (112) samples. The black (thinner) dashed lines indicate the blunting lines ($2\sigma_Y$ slope) according to ASTM E1820 [127], using the microscopic yield stress data [111], whereas the green (thicker) dashed lines are the offsets to the blunting lines by $0.5 \times CTOD$ (method 1 for J_Q). The dotted black line marks the 100 nm crack growth (method 2 for J_Q).

In order for J_Q to be sample size independent and qualify as J_{IC}, all sample dimensions $(W, a_0, W - a_0, B)$ must be larger than $10J_Q/\sigma_Y$ [127]. This condition could not be satisfied in any of the tested samples. Therefore, sample size dependent, "conditional" fracture toughness $K_{Q,J}$

values are reported in Table 3.3, obtained via the following equation using J_Q (method 1),

$$K_{Q,J} = \sqrt{\frac{EJ_Q}{1-\nu^2}} \tag{3.4}$$

The $K_{Q,J}$ values thus obtained are much smaller than the macroscopic fracture toughness (K_{IC}) value of tungsten for the {110}<100> crack orientation. As an alterative approach, maximum J values were taken from the resistance curves to obtain K_{Jmax} (Table 3.3) which, within experimental errors, were found to be in the range of macroscale K_{IC}. The crack growth (Δa) at J_{max} was in the range of 200 - 300 nm. These are similar to the crack growth values at critical J, i.e. J_{IC}, obtained for larger beam specimen (uncracked ligament >3 μm) reported in literature [117, 120, 122, 129] for other crack systems in tungsten.

3.4. Discussion

3.4.1. Anisotropic fracture behavior at small scales

In Fig. 3.9(a), a clear anisotropy in the fracture toughness behavior of single crystal tungsten can be seen at small scales. The {110} <100> oriented crack shows the highest fracture toughness at bulk scale as well as at the sub-micron scale, among the four low-index crack systems shown in Fig. 3.9(a). The {100} cleavage plane, though has the higher surface energy, has lower fracture toughness than the {110} cleavage plane. This deviation from Griffith theory has been attributed to the presence of four orthogonal easy crack propagation directions on the {100} plane than only one on the {110} plane [112]. For the fracture tests in a pre-cracked single crystal, the crack plane and the propagation directions are predefined, e.g. {110} and <100> in the present work, respectively. As a result, the initial crack growth which directly impacts the toughness measurement, has a

predefined direction as well. The anisotropy which arises from different propagation directions (Fig. 3.9(a)) can be explained via the process of lattice-trapping, which quantifies the stress range over which the crack is stable [130]. Due to the discrete nature of the bond breaking process, the lattice trapping process better explains the fracture anisotropy behavior than the continuum-based Griffith theory.

Table 3.3: Conditional fracture toughness values obtained for the W micro cantilevers in the present study. For comparision, the macroscale K_{IC} value for {110}<100> crack system in tungsten is 20.2 ± 5.5 MPa m$^{1/2}$ [112].

Sample ID	**Crack orientation**	$W' = W - a_0$ (μm)	$K_{Q,LEFM}$ (MPa m$^{1/2}$)	J_Q **(Method 1)** (N/m)	$K_{Q,J}$ **(Method 1)** (MPa m$^{1/2}$)	K_{Jmax} (MPa m$^{1/2}$)
Sample 1-1	{110}<100>	0.46	4.18	317.8	11.90	14.53
Sample 1-2	{110}<100>	0.61	4.50	319.2	11.93	14.43
Sample 2-1	{110}<100>	0.90	4.12	328.8	12.11	13.63
Sample 2-2	{110}<100>	0.96	3.91	350.2	12.50	14.17
Sample 3	{110}<112>	0.44	4.11	289.9	11.37	14.28
Sample 4	{110}<112>	1.20	3.22	259.6	10.76	15.43

The lattice-trapping range, ΔK is defined as [131],

$$\Delta K = \frac{K_+}{K_-} - 1 \tag{3.5}$$

where, K_+ and K_- are the upper and lower limit values of stress intensity factor between which an atomically sharp crack remains "lattice-trapped" during loading and unloading, respectively. Hiremath et al. [131] performed molecular statics simulations for fracture process in single crystal tungsten and computed the value of ΔK for all four low-index crack systems (listed in Table 3.1). They found that the {110} <100> crack system has the highest value ofΔK and hence the highest

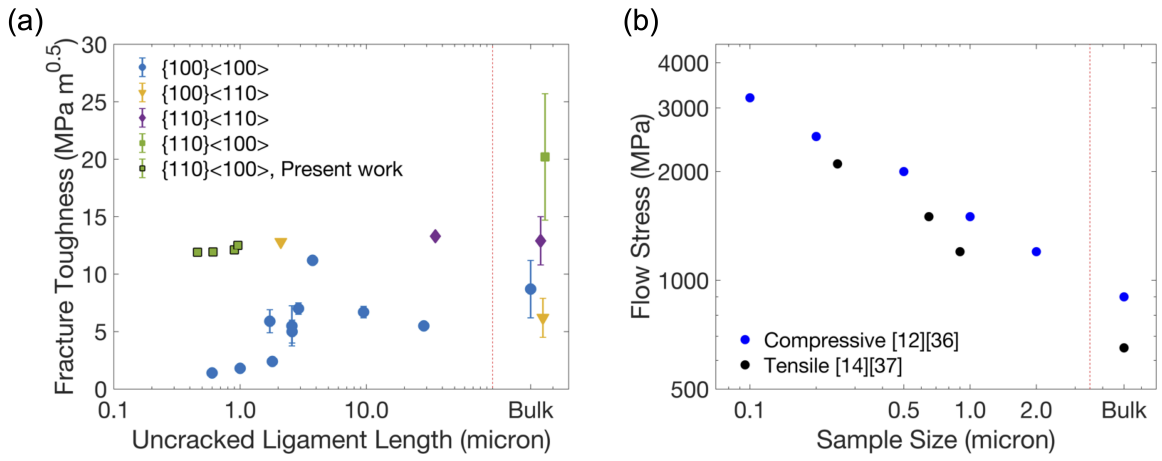

Figure 3.9: (a) Microcantilever fracture toughness tests conducted on tungsten at room temperature, with respect to the uncracked ligament size, as compared with the macro scale tests at room temperature. The literature results were taken from [112, 117–120]. (b) Yield stress vs. pillar size obtained from nanopillar compression and tension tests conducted on single crystal tungsten and compared with the corresponding macroscale values.

fracture toughness value, among all four. ΔK couldn't be computed for the {100} <100> crack system as the crack deflected on to the {110} plane in 7 out of 9 potentials they simulated. In the remaining 2 potentials, ΔK for {100} <100> were obtained as 0.33 and 0.51, whereas for {110} <100>, ΔK were obtained as 1.44 and 1.30. Furthermore, higher lattice trapping was observed in models with potentials corresponding to higher peak stresses required to overcome the cohesive strength, which can be considered analogous to smaller sample size and higher yield strength below 2-micron size scales (Fig. 3.9(b)). One can then expect the fracture anisotropy to get more pronounced for sub-micron sized samples, as is observed in Fig 3.9(a) and Table 3.1.

3.4.2. Stable crack propagation

All samples exhibited micro-ductile crack propagation, where it started with the crack tip blunting followed by the formation and growth of micro cracks [132]. The coalescence of these micro cracks which lead to further slow stable tearing, is evident via crack surface irregularities seen in SEM images (Fig. 3.5) as well as abrupt jumps in the measured displacement rate plots (Fig.

3.6). On one hand, this is a stark contrast from tungsten's macroscopic fracture behavior at room temperature where crack initiation is followed by cleavage fracture with no stable crack growth, and the final failure is catastrophic [112]. As a result of this pure brittle behavior, LEFM analysis is sufficient to characterize the fracture toughness in macroscopic samples of tungsten. On the other hand, stable crack propagation similar to the present study has been observed in all micro cantilever studies of tungsten at room temperature [117–120], with samples as small as 1.7 μm $(= W - a_0)$ showing stable crack growth of ≈ 500 nm. Via HR-EBSD and TEM imaging, Ast et al. [120] and Kalácska et al. [129] have shown that the ductile-brittle-transition (DBT) temperature for {100} <100> oriented crack in single crystal tungsten is just below the room temperature (21° C) at micron size scale. The activation energy of the process controlling DBT was calculated to be 0.36 eV, much lower than that of bulk tungsten samples (1.05 eV) [106]. This remarkable observation at beam size of ≈ 4 μm $(= W - a_0)$ was attributed to enhanced screw dislocation mobility as a result of high flow and shear stresses, providing definite proof that brittle BCC materials like tungsten exhibit ductile behavior at micron size scales. As the size is further reduced to sub-micron levels, the flow stresses are so high (> 1 GPa) that the mobility of screw dislocations is enhanced further close to that of edge dislocations and the mechanism transitions from thermal activation to phonon drag [10]. Therefore, reducing the sample size becomes a proxy for increasing temperature. The phenomenon of small scale leading to ductility has been observed in other macroscopically pure-brittle materials as well [133–135].

Note that stable crack growth was not observed for < 1 μm sized beams of tungsten for {100} cleavage plane [117], whereas in the present study of {110} crack plane, ≈ 150 nm and ≈ 300 nm of stable crack growth occurred in 500 nm and 1 μm samples, respectively, as shown in Fig. 3.8.

The absence of onset of instability and catastrophic failure in previous work [117] can be attributed to their loading method. Bohnert et al. [118] performed standard method (monotonic) as well as compliance method (cyclic) loading of {110}<110> oriented notched tungsten beam samples of same dimensions ($W - a_0 = 35.2$ μm). In the former loading case, unstable crack growth followed by cleavage fracture after a relatively short stable growth was observed, whereas there was no onset of instability in the latter case. This behavior is expected because the displacement-controlled unloading sequences stabilize the crack growth at the end of each cycle, which is required for elastic-plastic fracture analysis [118, 136, 137]. Ast et al. [120] performed room temperature monotonic loading coupled with sinusoidal displacement at different loading rates and observed that reducing loading rate can completely suppress cleavage fracture.

3.4.3. Size dependent fracture toughness in tungsten

As shown in Fig. 3.9(a) and summarized in Table 3.1, there is a clear effect of sample size on the conditional fracture toughness ($K_{Q,J}$) of single crystal tungsten along both primary cleavage planes, {100} and {110}. The $K_{Q,J}$ value decreases below the macroscopic fracture toughness value (K_{IC}) when the uncracked ligament length is reduced to below 2 μm. Interestingly, this is also the threshold sample size at which the flow stress of single crystal tungsten rapidly increases (Fig. 3.9(b)) as per the power law relation [111],

$$\sigma_y \propto d^{-0.32} \tag{3.6}$$

where d is the sample size. Therefore, the size dependent behavior of fracture is associated with the increasing yield strength. A direct visualization of the plasticity ahead of the crack tip was

given when Kalácska et al. [129] provided 3D shape of the plastic zone via density of geometrically necessary dislocations (GND) obtained from HR-EBSD imaging. The GND density was highest near the free surface of the beam ($W - a_0 = 3$ μm) which spread over a longer distance along the crack propagation direction as compared to the center of the beam. This high-density region had a depth of 1 μm into the beam thickness. Since all our samples have thickness less than or equal to 1 μm, this strong free surface effect is expected to spread over the entire thickness of the beam. Therefore, the observed free surface effect along with high dislocation mobility (discussed in previous section) at submicron scales cause the dislocations generated at the crack tip to immediately leave the beam thereby effectively reducing the shielding of the crack. As a result, the conditional fracture toughness ($K_{Q,J}$) value is lowered for beam sizes below 2 μm ($= W - a_0$). On the other hand, the K values obtained from the maximum J values of the resistance curve seem to reach the macroscopic fracture toughness (K_{IC}) of tungsten for the same crack system (Table 3.3). Hence, the sample size in our study at submicron scale is too small to obtain sample-size independent material property of fracture toughness.

3.5. Conclusion

In this chapter, in-situ SEM bending experiments of single crystal tungsten nano and micron sized notched cantilever beams were presented. Via multi-step FIB milling, samples with uncracked ligament length from 500 nm to 1 μm were fabricated with the notch-tip radii as small as 8 nm. The notch in each beam was oriented to investigate one of the preferred cleavage planes of tungsten, $\{110\}$ with the crack propagation directions of <100> and <112>. During the bend test using a cono-spherical indenter, the main finding is the stable crack growth observed in all the notched samples, contrary to pure cleavage failure observed in macro sized tungsten samples. This behavior

is attributed to the enhanced screw dislocation mobility to be close to that of edge dislocation and transition of mobility mechanism from thermal activation to phonon drag, due to very high flow stresses at size scales below 2 μm. This finding can also be used to understand the lower brittle to ductile transition temperature for tungsten single crystal at micro scale.

Due to significant plasticity ahead of the crack, elastic plastic fracture mechanics approach was employed to determine the conditional fracture toughness values ($K_{Q,J}$). For all the submicron samples, $K_{Q,J}$ values were obtained to be 11.76 ± 0.56 MPa m$^{1/2}$, which is lower than the macroscale K_{IC} value of 20.2 ± 5.5 MPa m$^{1/2}$ for {110} <100> crack orientation. The size effect on fracture toughness behavior is observed. The lower conditional fracture toughness at small scales is attributed to the plastic zone size being larger than the sample dimensions ($B, W - a_0$). This is due to improved dislocation nucleation and mobility as well as strong surface effect and limited sample size. These $K_{Q,J}$ values are not material constants as they don't satisfy the size requirements. Nevertheless, they are still crucial in providing a quantitative idea towards fracture behavior in similar sized structural components of W in real world applications such as MEMS devices.

Chapter 4. Stishovite Nucleation at Low Shock Pressures in Soda-lime Glass Plates

In previous chapters, the effect of domain size on plastic and fracture behavior of single crystal BCC Tungsten was analyzed and presented. The size dependent dislocation activity was attributed as the cause of such behavior. Now, the focus will be shifted towards amorphous silica glasses, namely Fused Silica (FS) and Soda Lime Glass (SLG), and how small scale would influence their inelastic behavior, in complete absence of dislocations. Mainly, the polymorphic activity in silica is analyzed in this work. FS is known to transform to high-pressure crystalline phase called Stishovite at shock pressures of 34 GPa [138], at macroscale. However, no such threshold is known for SLG. In the current chapter, we report nucleation of the crystalline Stishovite phase in shock-loaded SLG plate samples at a remarkably low shock compressive stress of 7 GPa. Although it falls within the reported Hugoniot Elastic Limit of SLG between 2.5 GPa and 7 GPa, it is significantly below the crystallization threshold of 34 GPa observed for fused silica. SLG plates were shock loaded by impacting them at 1-2.5 km/s using a table-top experimental setup in which 1 mm-dia Al micro flyer plates of 25-50 μm thickness were generated and propelled using a top-hat Nd:YAG laser pulse of 8 ns duration. The shocked samples were imaged using High Resolution Transmission Electron Microscopy (HRTEM) and further analyzed using Selected Area Electron Diffraction and FFT analyses. All samples showed nucleation of 4 nm Stishovite crystals distributed within the amorphous SLG matrix. The stress state was determined by directly measuring the flyer speed, particle velocity, and shockwave speed by using a state-of-the-art Photonic Doppler Velocimeter (PDV).

4.1. Introduction

Recently the shock response of soda-lime glass (SLG) has received much attention in the armor research community because of its potential to absorb substantial shockwave energy by transforming into its crystalline Stishovite phase. This phase transformation is accompanied by almost 40% volume reduction and is similar to that uncovered in silica glasses. Roshdy et al. [16] subjected a stack of SLG layers to a hypervelocity penetrator and analyzed the debris left behind in the channel created by the projectile. Prior to the X-ray analysis, the debris was washed in a hydrofluoric acid bath in which the Stishovite phase dissolves very poorly. The analysis confirmed the formation of the Stishovite phase. By subjecting SLG samples to shock pressures up to 110 GPa, Gorfain et. al. [17] found that the high pressure Hugoniot of SLG displayed stiffness that was similar to that of pure Stishovite. Alexander et. al [18] measured the release response of SLG from pressures as high as 40 GPa and observed a change in the shock release dynamics when compared to the fused silica response. Their work suggested that the network modification of silica due to the presence of alkali oxides in SLG inhibits transition to the Stishovite phase. However, the high-pressure steepness in the Hugoniot curve, similar to Stishovite hydrostat, suggested a quick reversible transition that prevents freezing of the Stishovite phase.

In all of these previous studies the entire volume of the sample is transformed into the crystalline phase which is then spotted through the change in continuum-level mechanical response. However, among recent studies on shock response of SLG, Renganathan et. al. [19] provided a different picture of continuum response at high stress levels (37 – 120 GPa). The linear shock velocity – particle velocity ($U_s - u_p$) model in their study shows that the Hugoniot states do not match the stiffness of the Stishovite phase as observed in fused silica. The aim here is to determine

the threshold stress state at which the Stishovite crystals are nucleated from the amorphous SLG phase. The continuum Hugoniot response is not sensitive enough to spot the onset of any crystalline transformation. We determined the Stishovite nucleation stress by subjecting a series of SLG glass plates to increasing stress amplitudes from well-defined rectangular stress pulses of 8ns and 16ns duration. These stress pulses were generated by impacting the samples by laser-generated and propelled microflyer plates at 1-2.5km/s. Each shocked sample was then carefully analyzed using a combination of atomic resolution Transmission Electron Microscopy and FFT analysis to spot for any nucleated Stishovite nanocrystals. In this chapter, we report the formation of Stishovite crystals of 4nm in size at a threshold stress of 7 GPa which is above its lowest reported Hugoniot Elastic Limit of 2.5 GPa [139].

4.2. Experimental Setup and Procedure

A cross-sectional view of the sample assembly that was used to load SLG plates by an Al microflyer plate is shown in Fig. 4.1. The micro flyer plate was generated by impinging a 8 ns duration, Nd:YAG laser pulse, onto a 1 mm diameter spot on the back surface of a 25 μm thick Al foil which was bonded to a transparent borosilicate glass window of 6 mm thickness. The absorbed optical radiation at the foil's rear surface creates plasma and leads to punching out of an aluminum microflyer disc of approximately the laser-impinging diameter [140]. This microflyer disc then accelerates through the air (or vacuum) due to the rapid expansion of the plasma on its rear surface and impacts the SLG sample that is stationed about 500 μm in front. The flyer plate attains its maximum velocity within 100 ns. To create space for the accelerating flyer, the SLG sample was axially separated from the glass window by using edge spacers. The entire assembly was secured inside a sample holder (Fig. 4.2). A Nd:YAG pulse laser of 2 J max energy and 12 mm output

beam diameter was used as the launch laser. Following the procedure outlined by Brown et al [140], the output pulse from the YAG laser with a Gaussian energy profile with a M2 value of 2 was first converted into a "top-hat" beam using diffractive optics. The top-hat beam output was then focused on the back surface of the Al foil using an aspheric lens. This is an important part of the experimental procedure because the use of a Gaussian profile pulse results in the generation of non-uniform spatial stresses within the flyer plate volume and results in its complete disintegration prior to its arrival at the SLG target. The top-hat beam has a significant number of hot spots in its profile but they were found not to affect the launch and the planarity of the flyer plate [140].

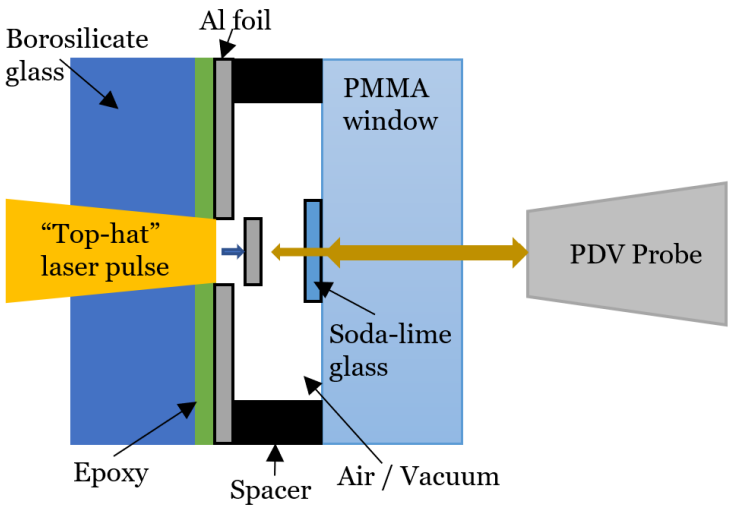

Figure 4.1: Cross-sectional view of the sample assembly showing punching of the flyer disc by the impinging top-hat laser pulse, and the probe beam from PDV for measuring the flyer velocity and shock arrival at the sample's back surface.

The stress state, σ, in the sample was obtained by measuring the flyer velocity, particle velocity u_p at the sample's back surface (that is struck by the flyer plate), and the shock velocity U_s through the sample, by using a state-of-the-art Photonic Doppler Velocimeter (PDV). A schematic of the PDV along with other optical components that were used in training the interferometric and the launch laser beams, to and from the sample surface, are shown in Fig. 4.2. Details of PDV

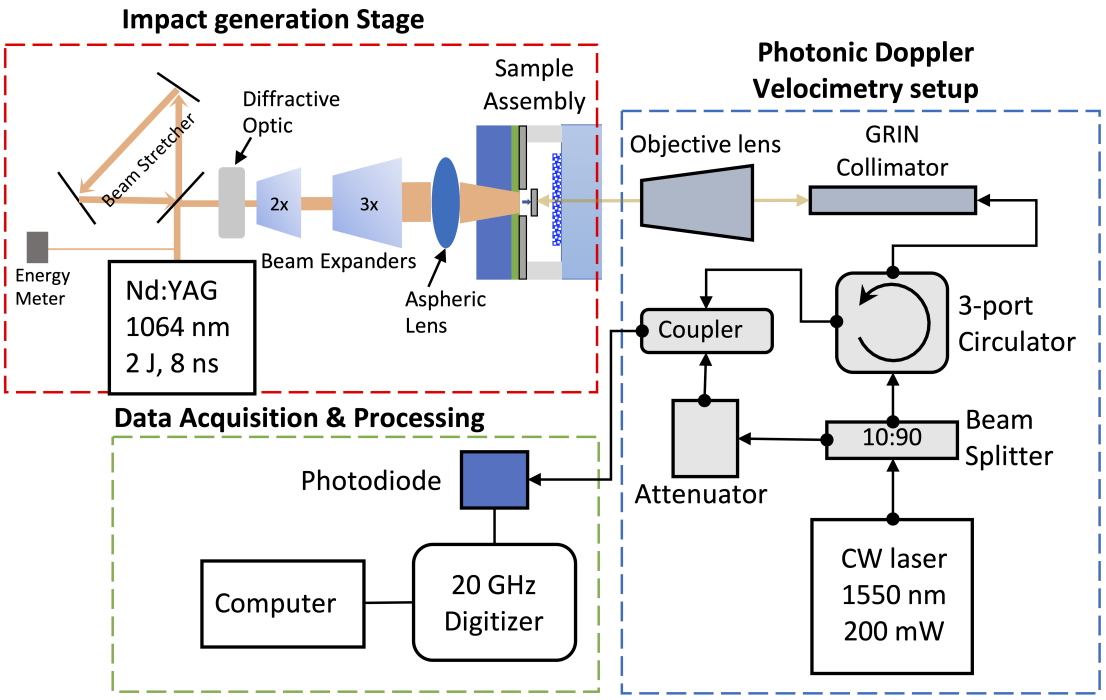

Figure 4.2: Schematic of the laser generated flyer plate setup along with that of the Photonic Doppler Velocimeter (PDV). Black arrows in PDV setup denote single-mode optical fibers for 1550 nm wavelength.

construction and its working principle can be found in the literature [141, 142]. In our study, a combination of GRIN collimator and a microscope objective was used as the probe. The PDV beam from the 1550 nm CW laser source (Fig. 4.2) was first collimated to 500 μm diameter and then focused onto the front surface of the Al foil using an objective lens. The focused spot was ~78 μm with a long Rayleigh length of about 12 mm. This arrangement ensured that the microflyer disc remained in focus during its entire flight distance of 500 μm before it struck the SLG sample. The pulse and the probe beams were perfectly aligned using lasers to ensure that the probe beam was focused right at the center of the launched microflyer plate.

The stress, σ, in the sample was calculated using,

$$\sigma = \rho_0 U_s u_p \tag{4.1}$$

Here, ρ_0 is the initial density of the sample, which was measured to be 2.497 g/cc for our SLG samples. The particle velocity (u_p) was taken as the velocity of the flyer plate immediately after the impact. The transparency of the SLG sample allowed simultaneous measurements of the flyer velocity and the shock velocity. This was accomplished by coating the front (PDV) side of the SLG sample with a semi-transparent Au layer of 15 nm thickness [143]. As shown in Fig. 4.2, the transmitted part of the PDV beam tracked the movement of the flyer while the part that was reflected by the Au layer detected the arrival of shockwave at the front surface of the sample. With known sample thickness, this allowed accurate determination of the shock velocity through the sample.

Tests were performed using 25 μm and 50 μm thick flyer plates which resulted in stress pulses of 8 ns and 16 ns duration, respectively. These flyer plates were launched with 50-150 J/cm^2 laser fluence which resulted in a peak flyer velocity of 2.5 km/s.

4.3. Experimental Results

Figures 4.3 (a) and (c) show PDV signals that were acquired when SLG plates were struck with 25 μm thick and 50 μm thick flyer plates, respectively. Both these flyers were propelled using a laser fluence of 100 J/cm^2. Figures 4.3 (b) and (d) show the corresponding velocity spectrograms that were obtained after reducing the raw data in Fig 4.3 (a) and (c), respectively, by using the moving window Fourier transform routine. As seen in Fig. 4.3 (b) and (d), there is a sudden drop in the flyer's velocity which corresponds to the time of impact with the sample. The planar shock generated in the sample can be observed in the spectrogram as the period of constant velocity immediately after the impact. This was recorded as the particle velocity, u_p. Consistent with the standard flyer plate setups, the generated shockwave in the sample has a duration that is equal to the shockwave round trip time in the microflyer plate, which is 8 ns and 16 ns, for the 25 μm and 50 μm

thick flyer plates, respectively.

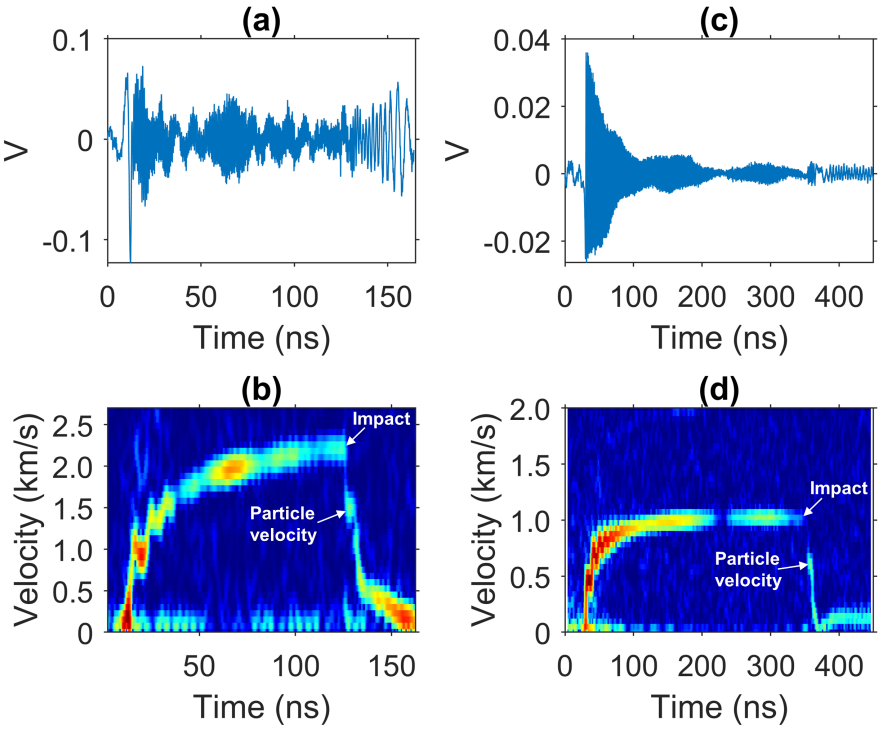

Figure 4.3: Representative PDV signals for flyers launched at 100 J/cm2 laser fluence. (a) and (b) display the probe signal and its corresponding spectrogram, respectively, for a 25 μm flyer, whereas (c) and (d) show the same for a 50 μm flyer that was launched with the same laser fluence. Point of abrupt drop in the velocity spectrogram coincides with the flyer impact (shown via arrow). The short duration of constant velocity (particle velocity shown via arrow) following the flyer impact represents the period of shock generation in the sample.

The Hugoniot equation of state results for SLG from our impact experiments are shown in Fig. 4.4 along with those obtained using the conventional gas-gun launched plate impact setups from the literature. The maximum shock pressure achieved in our tests was 22 GPa which corresponded to the micro flyer impact velocity of 2.5 km/s. Our micro flyer data tracks data from other investigators fairly well. However, our data is at strain rates ($10^7 - 10^8$ s^{-1}) that are about two orders of magnitude higher. It should be noted that we can take hundreds of shots in a single day, if needed. In contrast, in traditional plate impact setups, one is limited to no more than 10 shots per day because of the complexities associated with reloading the multi-stage gas guns. Another advantage of the micro

flyer impact setup is that the glass sample remains intact after impact as the damage is localized to only 1 mm-dia region of the 25mm-diameter glass plate. This allows microscopic examination of the severely deformed and micro-cracked region of the otherwise intact plate. Figures 4.5 (a)-(c) show the results of such an analysis for a crater that was caused by a 50 μm thick flyer disc. This sample was subjected to 1.0 km/s impact, resulting in a peak pressure of 7 GPa for 16 ns. A summary of the impact experiments is shown in Table 4.1.

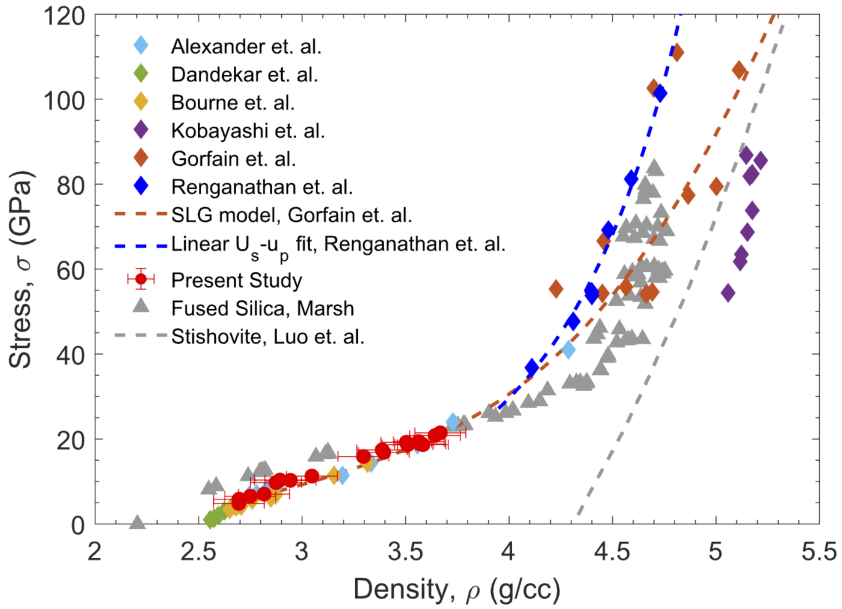

Figure 4.4: Shock Hugoniot curve for Soda-lime glass (SLG). Red circles with error bars represent the results from the present study. Strain rate was 1.25×10^8 s^{-1}. Hugoniot for fused silica and pure Stishovite obtained by various investigators are also shown for comparison.

To spot for any polymorphic changes, the microstructures of the samples that were shocked to 7 GPa, 10 GPa, and 20 GPa pressure were examined using a FEI-Titan Scanning/Transmission Electron Microscope (STEM) at 300 kV. The TEM specimens were prepared from the center of the impacted region by FIB micromachining as shown in Figs. 4.5 (d)-(f). Atomic-scale imaging and Fast Fourier Transform (FFT) analyses confirmed the presence of nanocrystalline regions, about 4 nm in size, distributed within an amorphous matrix. These were found in all samples. Such regions

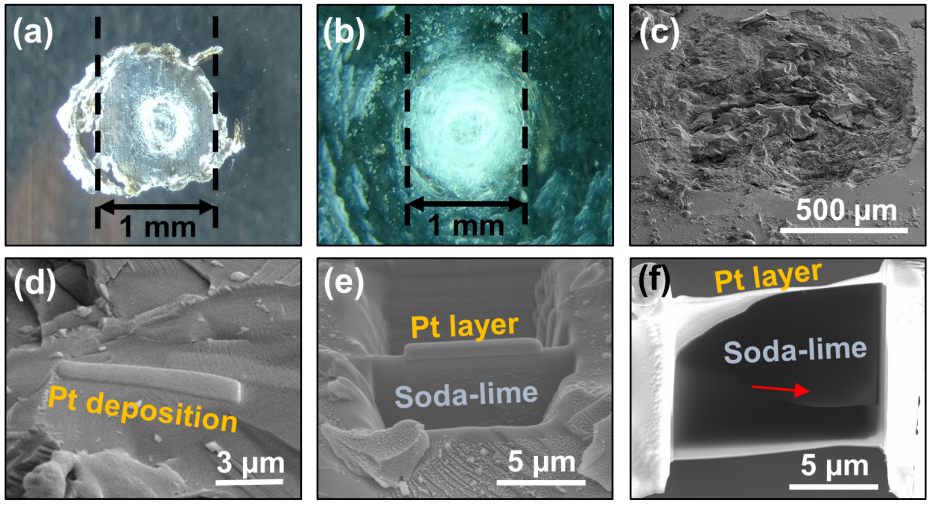

Figure 4.5: (a) Optical micrograph showing a recovered 50 µm thick flyer disc. It impacted the sample at 1.0 km/s to result in a planar shock pressure of 7 GPa for a duration of 16 ns. Optical (b) and SEM (c) images of the impact site on the sample. (d), (e), and (f) show TEM sample preparation steps using FIB. Red arrow in (f) points to region where HRTEM images were taken.

from each sample are shown in Fig. 4.6. The indexed FFT results from one such region from a sample that was shocked to 7GPa is shown in Fig. 4.7. It shows diffraction spots corresponding to the crystalline phase, in addition to the amorphous rings. The experimentally measured interplanar d-spacing from this analysis matched closely with those known in the literature for tetragonal Stishovite. Table 4.2 shows such a comparison. The very small difference between the two confirms these nanocrystalline regions to be that of Stishovite.

To rule out any electron beam irradiation related crystallization effects, as known in Si [144], we performed a control test by exposing SLG samples to 300 kV electron beam for 0, 7 and 12 minutes. The TEM examination of these samples did not reveal any crystalline phase as shown in Fig. 4.8.

4.4. Discussion

Our results provide first visual confirmation of Stishovite crystallization from amorphous SLG microstructure at extremely low shock pressure of 7 GPa. While these pressures are still above

Table 4.1: Summary of laser generated flyer plate impact experiments on SLG samples. Flyer, particle, and shock velocities were measured directly using the PDV. The stress and density values were calculated using the Hugoniot relations. Experiment (Expt.) number (No.) starting with designation fp25 and f50 correspond to flyer plates of thickness 25 μm and 50 μm, respectively.

Expt. No.	Flyer velocity (km/s)	Peak Particle Velocity u_p (km/s)	Shock Velocity U_s (km/s)	Peak Stress σ (GPa)	Density ρ (g/cc)
fp50-700	0.68	0.41 ± 0.01	5.62 ± 0.20	5.81 ± 0.26	2.70 ± 0.12
fp50-1000	0.94	0.59 ± 0.01	4.77 ± 0.20	7.03 ± 0.29	2.82 ± 0.12
fp25-750	1.47	0.90 ± 0.01	5.00 ± 0.20	11.27 ± 0.43	3.05 ± 0.12
fp25-1000	2.01	1.24 ± 0.01	5.12 ± 0.20	15.88 ± 0.60	3.30 ± 0.12
fp25-1100	2.11	1.34 ± 0.01	5.05 ± 0.20	16.85 ± 0.64	3.39 ± 0.13
fp25-1100-1	2.11	1.36 ± 0.01	5.16 ± 0.20	17.45 ± 0.66	3.39 ± 0.13
fp25-1100-2	2.18	1.47 ± 0.01	5.09 ± 0.20	18.65 ± 0.70	3.51 ± 0.13
fp25-1200	2.30	1.51 ± 0.01	5.01 ± 0.20	18.83 ± 0.71	3.57 ± 0.13
fp25-1200-1	2.22	1.49 ± 0.01	5.18 ± 0.20	19.22 ± 0.72	3.50 ± 0.13
fp25-1200-2	2.46	1.62 ± 0.01	5.15 ± 0.20	20.81 ± 0.78	3.64 ± 0.14
fp25-1200-3	2.51	1.69 ± 0.01	5.19 ± 0.20	21.90 ± 0.80	3.67 ± 0.14

Table 4.2: Interplanar (d) spacings measured from FFT analysis and its comparison with the known values for Stishovite from the literature. The index numbers refer to the ones shown in Figs 4.6 and 4.7.

S.No.	d measured (nm)	d Stishovite (nm)	h k l	Int.	Error (%)
1	0.29	0.2958	110	100	2.0
2	0.22	0.2249	011	22	2.2
3	0.15	0.1531	121	37	2.0

the Hugoniot elastic limit (HEL) of SLG [18, 139, 145], they are significantly below the 34 GPa threshold for transformation to the Stishovite phase from fused silica as reported in a recent conclusive study of Tracy et al. [138]. Recognizing that the in-situ XRD analysis performed during the shock loading in the Tracy et al. [138] study is not sensitive enough to record the nucleation of

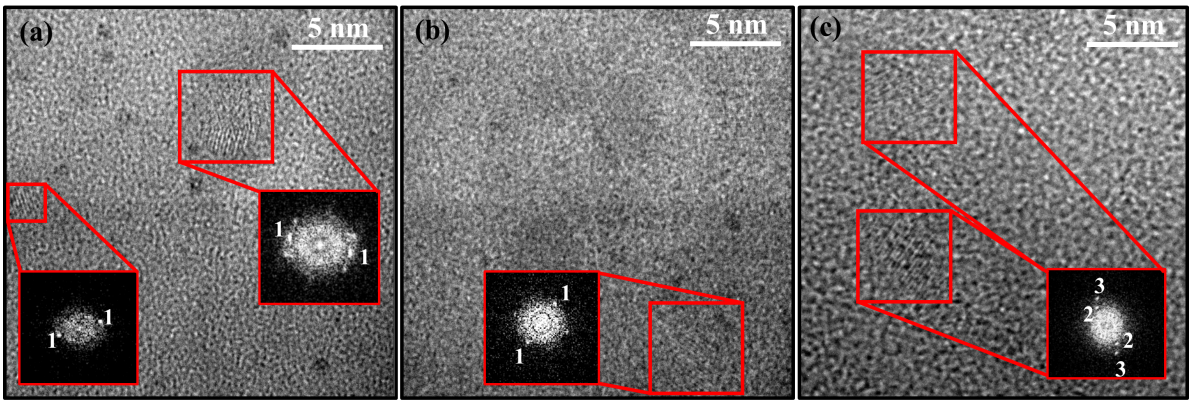

Figure 4.6: HRTEM images of nucleated Stishovite crystals of approximate 4nm in size in a series of Soda-lime glass samples that were subjected to planar shock pressures (duration in parenthesis) of (a) 7 GPa (16 ns), (b) 10 GPa (8 ns), and (c) 20 GPa (8 ns), resulting from impact velocities of 1.0 km/s, 1.5 km/s, and 2.5 km/s, respectively. HRTEM images were taken from near the bottom region of the respective samples, similar to that marked in Fig. 4.5 (f). The insets show FFT images of the nanocrystals, with diffraction spots (marked as 1, 2 and 3, with reference to Table 4.2) which were all confirmed to correspond to the Stishovite phase.

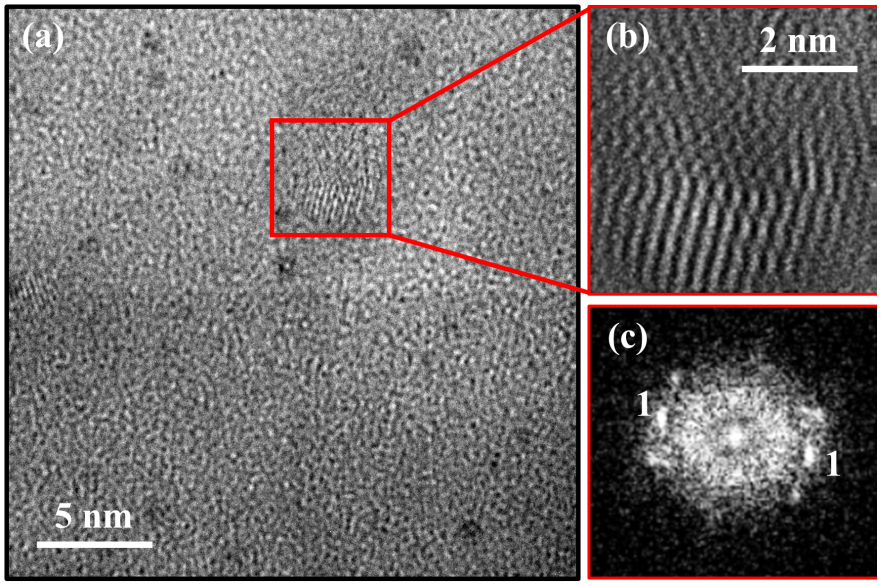

Figure 4.7: Stishovite nucleation in the Soda-lime glass sample of Fig. 4.5 that was subjected to 7 GPa pressure for 16 ns. (a) High Resolution TEM image from the region marked with a red arrow in Fig. 4.5 (f), showing crystalline regions distributed within an amorphous SLG matrix. (b) zoomed-in image of one of the nanocrystals of 4 nm size. (c) FFT analysis of the region shown in (b) with diffraction spots marked as 1 (Table 4.2) which corresponds to a d-spacing value of 0.29 nm for Stishovite.

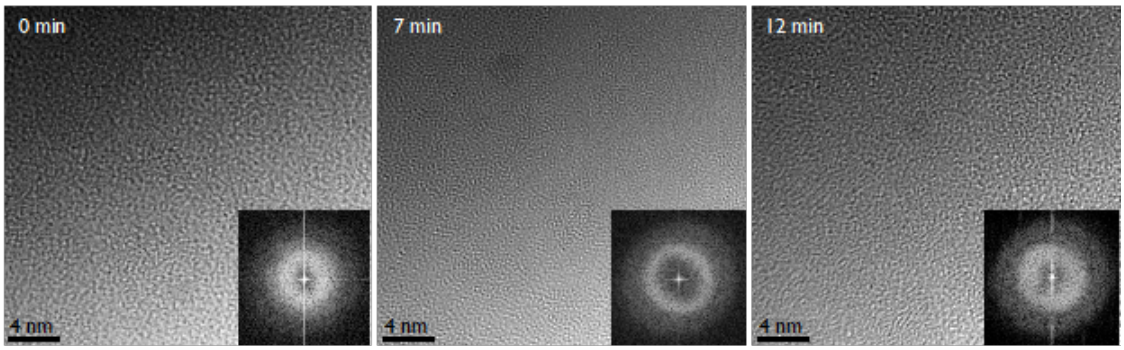

Figure 4.8: TEM images along with their FFT analysis results (insets) for three bulk soda-lime glass samples that were exposed to electron beam for 0, 7 and 12 minutes. No crystalline phase is observed in any sample. These results prove that the crystalline phases found in the shock-loaded SLG samples are not due to any electron beam irradiation effect.

small number of Stishovite nanocrystals, we repeated the micro flyer experiments by replacing the SLG plates by fused silica plates of identical dimensions. The subsequent TEM and FFT analyses did not reveal nucleation of any Stishovite nanocrystals even when the samples were stressed to 20 GPa.

4.4.1. Plastic flow under shock compression

The low Stishovite nucleation stress may be related to the known unusual elastic-plastic response of SLG compared to other materials. Sundaram and Clifton [146, 147] and Clifton et al. [148] have reported a drop in shear resistance of SLG for longitudinal compressive stress greater than 3.5 GPa. Measurements by Alexander et al. [139] indicate that the longitudinal stress remains elastic up to 7.5 GPa despite a loss of shear resistance (strength) around 3.5 GPa. Applying the standard definition that the HEL is the stress at which a material experiences plastic deformation, Alexander et al [139] assigned HEL of SLG to be around 3.5 GPa since with no shear resistance, even the smallest shear stress will lead to plastic deformation. The highly pulverized material under the flyer in our experiments should result in the generation of such shear stresses. The material thus flows

like a fluid under these conditions. This resulted in the samples displaying extreme ductility with strain to failure exceeding 60%. In the dynamic experiments reported here the energy supply for such deformation is shut off at 8-16ns depending upon the flyer thickness.

The occurrence of phase transformation within such a short duration is consistent with the MD simulation work of Shen et al. [149] in fused silica who report Stishovite nucleation to occur in 0.2 ns with subsequent grain growth occurring at 6 nm-ns^{-1}. Grujicic et. al [150] also observed an increase in the Si coordination number from 4 to 5 in a matter of 10 ps in a SLG sample that was shocked to 4 GPa. They however did not observe any Stishovite nucleation. These short durations suggest that such transformations arise from local correlated motions of atoms as opposed to longer length scale diffusive rearrangements. Dremin and Breusov [151] explain how fluid-like material flow upon plastic deformation provides transport of the atoms to the nuclei of the new phase to allow atomic intermixing and growth of the nucleated phase. This large-scale diffusion-like movement is accomplished through plastic deformation albeit at extremely short durations in the absence of regular diffusion. According to this scheme, when two layers of a substance are displaced relative to one another, on account of fluid-like plastic flow, the nuclei of a new phase located between them, can be regarded as a kind of a roller about which oscillations are executed. Since the time required for the rearrangement of electron shells (10^{-13} to 10^{-14} s) is much shorter than the time required for contact between atoms (10^{-12} s), it follows that all atoms in their weak chemical bonding states passing in the immediate vicinity of the nucleus/crystallization centers have sufficient time to combine with the latter forming the new phase. Thus, in contrast to the usual diffusional growth of crystallization centers, in which each atom must find its way to the new phase, pushing apart its neighbors with the available thermal energy, the formation of the new phase during shock

compression occurs by transport of the entire mass of the initial phase, by plastic flow, to the vicinity of the crystallization centers or activated complexes. The required atoms then combine selectively with the particles of the new phase, thus undergoing continuous growth during this process.

The aforesaid process also controls the mobility of both the highly mobile Na^{+} and Ca^{2+} ions in SLG to form dissimilar Na-Ca pairs [152] to form regions of pure silica from which the Stishovite crystals can be nucleated. The large compositional difference between the amorphous SLG (SiO_2-Na_2O-CaO-....) and crystalline Stishovite (SiO_2) also assists in the diffusion process [153, 154].

The low-pressure for observing Stishovite nucleation in SLG can be attributed to its more open and weaker network structure compared to fused silica. When alkali oxides, such as Na_2O and CaO, are added to pure SiO_2 to form SLG, the existing Si-O bonds are broken to incorporate the added oxygen ions in the network while the cations (Na^{+} and Ca^{2+}) remain close by to form the weaker ionic bonds. As a result, overall concentration of "non-bridging" oxygen ions increases, which are absent in the fused silica network [18].

4.4.2. Localized hotspot formation

In addition to the shear stress, shock-induced local temperature rise could have also driven the nucleation of the Stishovite nanocrystals in our experiments. Using MD simulations, Shen et. al. [149] have shown that the nucleation and growth kinetics of the Stishovite phase are a strong function of the shock temperature. Specifically, they found that the dependence of the Stishovite nucleation rate on temperature could be expressed using the standard Volmer-Weber nucleation model as,

$$\dot{N} = A\left[\exp\left(-\frac{\alpha T_m^2}{T(T_m - T)^2}\exp\left(-\frac{Q_n}{T}\right)\right)\right] \tag{4.2}$$

where, α and A are constants, Q_n is the activation energy, and T_m is the melting temperature. The rate of nucleation thus increases with the temperature (T), however, as the temperature approaches the melting point, the lower free energy released from nucleation provides a weaker driving force for the phase transition [149]. Once nucleated, the subsequent grain growth rate follows the standard Arrhenius dependence. Based on the MD simulation results of Grujicic et al [155], the temperature rise in our samples is expected to be in the 500-1200 K range. These are low values. However, movement of the atoms under shear stress, as discussed above, can lead to the formation of hot spots due to lattice friction where the temperature can be significantly higher than that predicted by the Hugoniot relations. This is similar to the “hot-spot crystallization" to Stishovite observed in porous sandstone by Mansfeld et al. [156] which they attributed to frictional heating and melting, followed by rapid quenching in those localized hot spots. Zhao et al. [157] have provided an analytical model to estimate this shear-driven local temperature rise in shock-compressed boron carbide crystals and found it to be significantly higher (1500 K) than the bulk temperature rise (500 K) at 45 GPa of shock compression. MD simulations of Devries et. al. [158] reproduced Zhao et al. results. They observed that when the alloy was shocked to 70 GPa, the temperature at the hot spots shot above the melting point (2000 K) while the bulk temperature remained below 900 K. They attributed this local temperature rise as the main contributor towards the dramatic loss of shear strength and amorphization in boron carbide. Therefore, in light of these works, the local temperature rise at the nucleation sites in our SLG samples is also expected to influence Stishovite formation.

The nanosecond shock duration and subsequent cooling of the sample after recovery in our experiments directly influences the size and volume fraction of the crystals formed. In-situ time-resolved diffraction experiments of shocked fused silica by Gleason et. al. [159] have

shown that Stishovite crystals revert to amorphous state within a fraction of nanosecond to 7 ns after the onset of the release wave, due to their limited thermal stability. Therefore, only trace amount of Stishovite crystals is expected to be present in the recovered samples. The presence of chemical impurities in SLG further limits the homogenous nucleation of Stishovite growth to only localized "cation-free" regions. This would explain why the Stishovite transformation is not uniform across our TEM samples and the largest crystal we obtained is only ~ 4 nm in size.

4.5. Summary

Soda-lime glass plates were shock loaded by impacting them using laser-generated and propelled 1mm-dia. Al microflyer plates of 25 – 50 μm thickness at 1 – 2.5 km/s. The stress state was determined by measuring the flyer speed, particle velocity, and shockwave speed by using a state-of-the-art PDV. The Hugoniot states obtained corresponded well with the conventional gas-gun launched plate impact experiments. The shocked samples were imaged using HRTEM and further analyzed using Selected Area Electron Diffraction and FFT analyses. All samples showed nucleation of 4 nm Stishovite crystals distributed within the amorphous SLG matrix. Surprisingly, a compressive stress of only 7 GPa corresponded to such nucleation events. Although this low stress falls within the reported Hugoniot Elastic Limit of SLG between 2.5 GPa and 7 GPa, it is significantly below the crystallization threshold of 34 GPa observed for fused silica. The low nucleation stress as well as the small size of the nucleated crystals is attributed to the presence of cation impurities, high localized shear stress, and shear-driven temperature rise.

Chapter 5. Polymorphic Activity in Silica Glass Nanopillars under Uniaxial Compression

In this chapter, effect of domain size on polymorphic activity in silica glass is explored by performing *quasistatic* compression of Soda Lime (SLG) and Fused Silica (FS) nanopillars of ∼500 nm diameter, fabricated via Focused Ion Beam (FIB) method. Remarkably, there is complete absence of brittle behavior during compression in both FS and SLG pillars, with plastic strains achieved over 50% without failure. Furthermore, we show for the first time that amorphous SLG nanopillars undergo polymorphic transformation to the densest crystalline Stishovite phase at only ∼5 GPa of normal stress and room temperature, by observing the post-compression pillars via high-resolution transmission electron microscopy (HRTEM) imaging. These findings of plasticity and crystallization support the conclusions of dislocation dynamics simulations [10] and compression / bending experiments (ref. chapters 2 and 3) on W pillars / beams which show that small domain size acts as a proxy for high temperature, thereby inducing ductility and reducing the pressure threshold of crystal nucleation. However, no crystallization is observed in the HRTEM imaging of fused silica nanopillars post-compression. This difference in polymorphic behavior between FS and SLG is attributed to the diffusion of impurity ions (Na^{+}, Ca^{2+}, etc.) under high shear stresses in SLG nanopillars creating easy nucleation sites of Stishovite. Once the metal ions diffuse away, free oxygen ions remain to form more Si-O bonds increasing the coordination number of Si atoms facilitating the formation of Stishovite. Coordination number of Si atoms in Stishovite is 6 compared to 4 in FS and SLG. Hence the nucleation is a combined process of densification, increase in coordination number of Si, and atomic rearrangement.

5.1. Stishovite Formation at Very Low Pressures in Soda-Lime Glass Nanopillars

5.1.1. Sample Preparation and Experimental Results

Commercial SLG in the form of thin microscopic cover slip was used for this study. Sub-micron glass pillars around 400 nm in diameter and aspect ratio between 1:2 and 1:3 were machined from the SLG by Focused Ion Beam (FIB). The FEI Nano 600 dual beam Scanning Electron Microscope/ Focused Ion Beam (SEM/FIB) was used for this purpose. A series of concentric annular milling patterns with different currents were applied to minimize the tapering. SEM images of the as-fabricated pillars in Figs. 5.1A and 5.2A show the characteristic tapering and rounded tip that are known to result from FIB milling.

Microcompression tests were conducted at room temperature under displacement control mode and at a strain rate of 10^{-3} s^{-1} using a PI 85 SEM PicoIndenter (Hysitron Inc.) with a 5 μm flat punch diamond probe. In order to avoid any overestimation of the measured stress due to pillar tapering, diameter at half-height was used to estimate the stress inside the pillars. Figure 5.3 shows representative engineering stress-strain plots for the two SLG pillars at room temperature when loaded at a strain rate of 10^{-3} s^{-1}. After reaching a peak stress of around 1000 MPa, both pillars show a remarkable capacity for plastic deformation, accommodating almost $\sim 60\%$ strain, with no evidence of any fracture. Figures 5.1B and 5.2B show SEM images of the deformed pillars. A maximum normal stress of 4.8 GPa and 4.2 GPa was calculated for pillars 1 and 2, respectively, by using their mid-height diameters. Besides the unusual plastic deformation, both pillars show a remarkable strain hardening effect which cannot be attributed to pillar tapering alone. This might

be indicative of the formation of a much harder phase during compression.

5.1.2. TEM Analysis

TEM samples from top to bottom of the compressed pillars were prepared by FIB as shown in Figs. 5.1C and 5.2C. These images reveal that excessive compression is accommodated inside the pillars through the formation of localized shear bands which are visible at the pillar surface as indicated by black arrows in Figs. 5.1C and 5.2C. TEM analysis was carried out using a FEI-Titan Scanning/Transmission Electron Microscope (STEM) operating at 300 kV. Using HRTEM and Fast Fourier Transform (FFT) analysis, we confirmed the presence of nanocrystalline regions, about 4 nm in size, distributed within an amorphous matrix (Fig. 5.1D). Its indexed FFT in Fig. 5.1E reveals four diffraction spots in addition to the amorphous rings. We have identified these crystalline phases as stishovite by comparing the experimentally measured interplanar spacings (Table 5.1) with those expected for the tetragonal stishovite. The relative errors between the measured and tabulated interplanar spacings (Table 5.1) are quite low which further confirm our main finding. Two stishovite crystals separated by a grain boundary (highlighted by a white arrow) can be observed in the atomic resolution TEM image in Fig. 5.1F as confirmed by its indexed FFT (Fig. 5.1G). Their corresponding interplanar spacing measurements are also collected in Table 5.1. It is interesting to note that edge dislocations (marked in yellow) are located on the 011 planes of the stishovite suggesting a deformed stishovite crystal during compression, where the slip planes are oriented about 45° with respect to the loading direction (LD). In addition to finding the stishovite crystals within the pillar volume, we also found them just below the base of the compressed pillars inside the SLG substrate. Figure 5.2D shows the HRTEM image of one such region below Pillar 2. Its indexed FFT (as inset) and their interplanar spacing measurements (Table 5.1) confirm that this crystalline

phase also corresponds to stishovite. The possibility of electron beam induced crystallization in SLG has already been ruled out in Chapter 4 (Fig. 4.8).

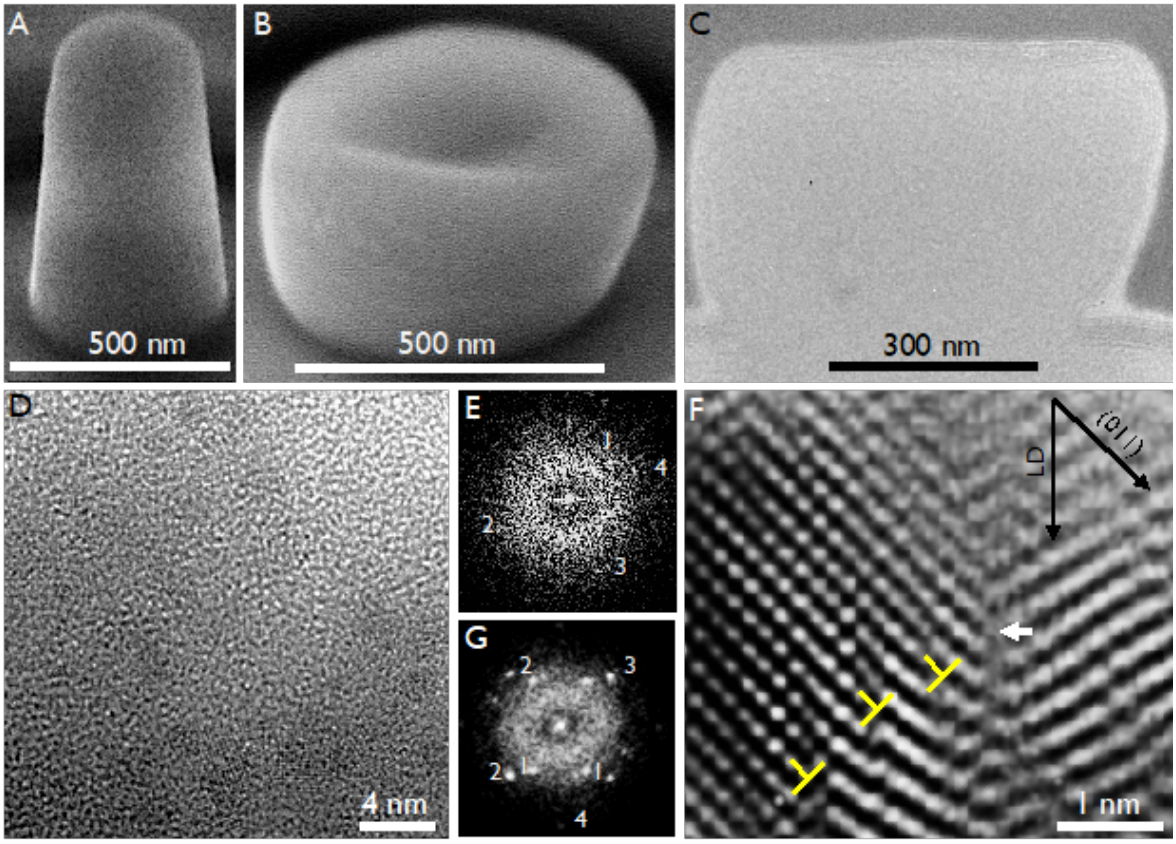

Figure 5.1: Stishovite formation in a sub-micron SLG pillar after 4.8 GPa of compressive stress. A, B, 35° tilted-view SEM images of glass pillar 1 before and after compression test. C, Thin film FIB prepared from the compressed pillar shown in B. D, High-resolution TEM image from the center of the pillar showing nanocrystalline regions in the compressed amorphous matrix. E, Fast Fourier transform (FFT) of the image shown in D displaying some crystalline spots in addition to the amorphous rings. F, Fourier filtered atomic resolution TEM image of Stishovite phase as reveals its FFT shown in G. Interplanar spacing measurements from E and G are collected in Table 5.1. Note edge dislocations (marked in yellow) located on the {011} planes of the Stishovite.

5.1.3. Discussion

The extremely low stishovite nucleation stress in SLG compared to that in fused silica of 34 GPa shock stress [138] is very surprising especially because in SLG in addition to atomic rearrangement one must also move the Na^{+} and Ca^{2+} ions to create cation-free regions into which pure stishovite

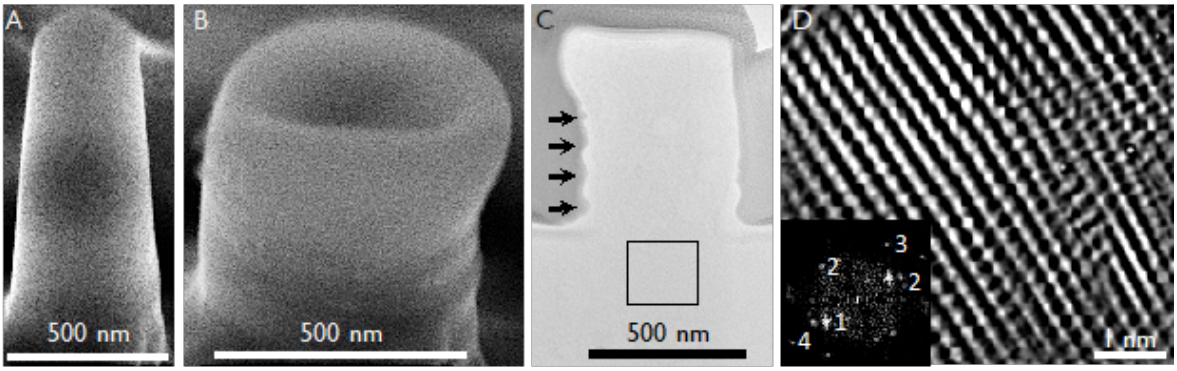

Figure 5.2: Stishovite formation in a sub-micron SLG pillar after 4.2 GPa of compressive stress and in the glass substrate underneath. A and B, 35° tilted-view SEM images of glass pillar 2 before and after compression test. C, TEM sample prepared by FIB from the compressed pillar shown in B. Shear bands are visible at the pillar surface indicated by black arrows. D, High-resolution TEM image of the substrate region highlighted by a square in C. Inset is its FFT showing diffraction spots corresponding to Stishovite phase as confirmed by their interplanar spacing measurements collected in Table 5.1.

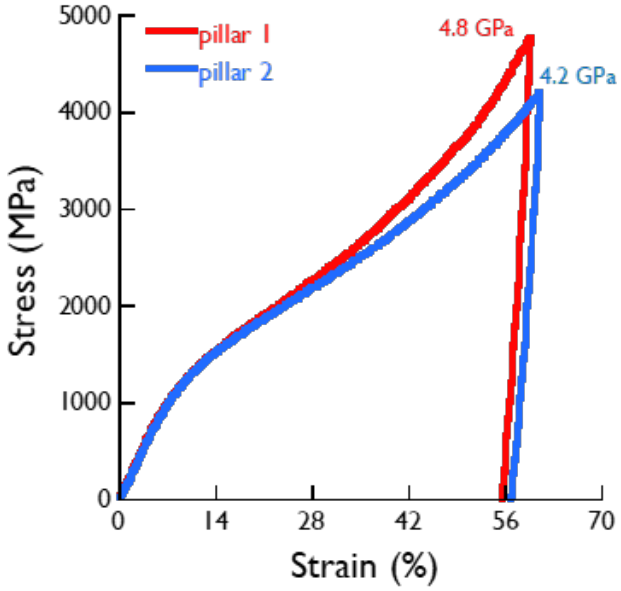

Figure 5.3: In-situ SEM nanocompression tests of sub-micron SLG pillars. Engineering compressive stress-strain curves reaching 4.8 and 4.2 GPa as the maximum compressive stress at around 60% of strain for pillars 1 and 2, respectively.

crystals can be nucleated. Thus, we require both high local stresses for enhanced atomic mobility as well as diffusion of Ca and Na ions to create cation-free regions. Interestingly, there is support for both these mechanisms as discussed below.

Table 5.1: Interplanar (d) spacings measured from FFT analysis and its comparison with the known values for Stishovite from the literature. The index numbers refer to the ones shown in Figs 5.1 and 5.2.

S.No.	d measured (nm)	d Stishovite (nm)	h k l	Int.	Error (%)
		FFT data from Fig. 5.1E			
1	0.29	0.2958	110	100	2.0
2	0.25	0.2600	001	7	3.8
3	0.22	0.2249	011	22	2.2
4	0.20	0.1981	111	38	1.0
		FFT data from Fig. 5.1G			
1	0.30	0.2958	110	100	1.4
2	0.22	0.2249	011	22	2.2
3	0.20	0.1981	111	38	1.0
4	0.15	0.1531	121	37	2.0
		FFT data from Fig. 5.2D			
1	0.29	0.2958	110	100	2.0
2	0.22	0.2249	011	22	2.2
3	0.20	0.1981	111	38	1.0
4	0.15	0.1531	121	37	2.0

For amorphous materials such as metallic glasses, the plastic deformation at room temperature is characterized by the formation and movement of highly localized shear bands [160, 161]. It has been suggested that the plastic flow within the shear bands destroys the short-range compositional order existent in the glass [162]. It can be understood as mechanical deformation-induced crystallization as reported for Al-based metallic glasses [163]. In this case, the large plastic strain during mechanical milling induces atomic displacements and enhanced atomic mobility. Therefore, plastic flow in silicate glasses requires shear deformation involving the breaking of interatomic bonds and the

formation of new bonds (equivalent to dislocation motion in metals) or densification, which involves simply a collapse of the structure into a more close-packed arrangement by minor bond rotation and changes of bond angles [163, 164]. Such a mechanism is clearly plausible in the intensely sheared regions of SLG in our experiments.

It is well known that among the three types of crystallization of amorphous solids, (primary crystallization, eutectic and polymorphous), primary crystallization requires atomic diffusion due to the large compositional difference between the amorphous phase and its crystallized product [153, 164]. SLG contains about 16 wt.% Na in the form of Na_2O and 10 wt.% Ca in the form of CaO in addition to SiO_2 [154, 165]. Therefore, during crystallization of stishovite from SLG, atomic diffusion of cations such as Na^+ and Ca^{2+} might be involved due to the large compositional difference between the amorphous SLG (SiO_2-Na_2O-CaO-....) and crystalline stishovite (SiO_2).

Previous studies on cation diffusion in SLG have reported that Na^+ ions are always more mobile than the Ca^{2+} ions [152, 166]. The peculiar diffusion behavior of Ca^{2+} is explained based on the formation of dissimilar Na–Ca pairs in soda lime silicates observed by nuclear magnetic resonance (NMR) studies [152]. We believe that the formation of these Na-Ca bonds provides the SLG with localized cation-free regions, where the stishovite phase can be formed. That would explain why the stishovite transformation is not uniform along the entire pillar but only in localized regions within the pillar as well as in the substrate just below the pillar.

In summary, we have demonstrated for the first time that small domain size can substantially reduce the pressure threshold for transformation at room temperature to the highly dense crystalline Stishovite phase in SLG.

5.2. Uniaxial Compression of Fused Silica Nanopillars

5.2.1. Sample Preparation and Experimental Results

Pure amorphous SiO_2 also known as Fused Silica (FS) used in this study was sourced from University Wafers Inc. FS nanopillars of ∼500 nm diameter were prepared using Focused Ion Beam (FIB) milling, based on the same recipe as the SLG pillars. SEM image of a representative as-fabricated pillar (Pillar 3) is shown in Fig 5.4(a). Uniaxial compression tests were performed in-situ SEM at room temperature under displacement control mode and at a strain rate of 10^{-3} s^{-1}. A PI 85 SEM PicoIndenter from Hysitron Inc. with a 5 μm flat punch diamond probe was used for this purpose. SEM image of the deformed representative pillar (Pillar 3) post compression is shown in Fig 5.4(b). A total of 3 pillars (Pillar 1, 2 and 3) were tested and their force displacement data generated by the equipment software were converted to normal stress strain curves using the mid height diameters of the respective pillars (Fig 5.4(c)).

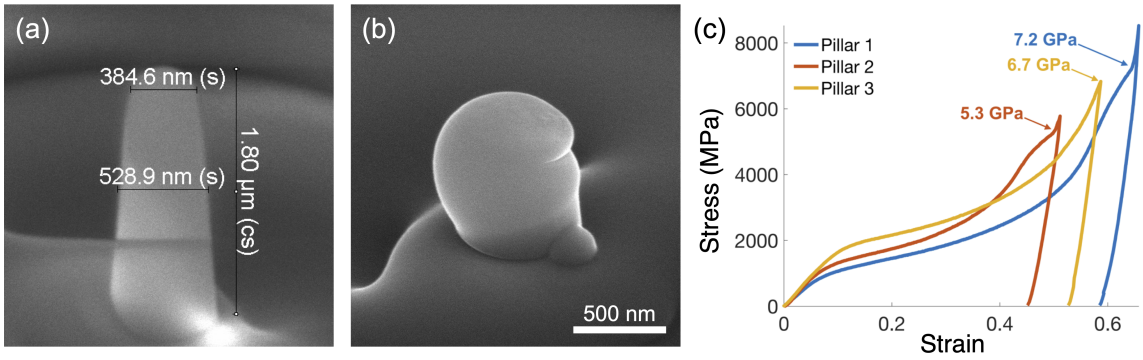

Figure 5.4: In-situ SEM uniaxial compression of Fused Silica Nanopillars. (a) and (b) show the SEM images of the representative pillar (Pillar 3) before and after compression, respectively. (c) shows the normal stress strain curves of all three pillars (Pillar 1-3). The sudden increase in stress towards the end of loading in Pillar 1 and 3 is due to the indenter probe contacting the bulk of the sample.

When compared with results of SLG nanopillars from previous section (Fig. 5.3), the stress

levels at similar strains are higher in FS pillars (Fig. 5.4(c)). This is expected because FS has a more compact and closed Si-O network structure whereas SLG has an open Si-O network due to the presence of ionic impurities (Fig. 5.5) [18]. Similar to our observation in SLG nanopillar (ref. sec. 5.1), FS also shows significant plasticity during compression, accommodating tremendous normal strains upto 60% with visible shear banding and complete absence of fracture (Fig. 5.4 (b) and (c)). This is a direct result of small domain size (< 1μm) inducing ductility in a macroscopically brittle solid. FS is known to behave in a semi-brittle manner even at sizes as small as 3 μm [167], with plastic strains up to 20% before fracture and no shear banding. Significant strain hardening is also observed in FS nanopillars which is due to the characteristic irreversible densification process in silica glasses under both quasistatic [167, 168] and shock [169, 170] loading conditions.

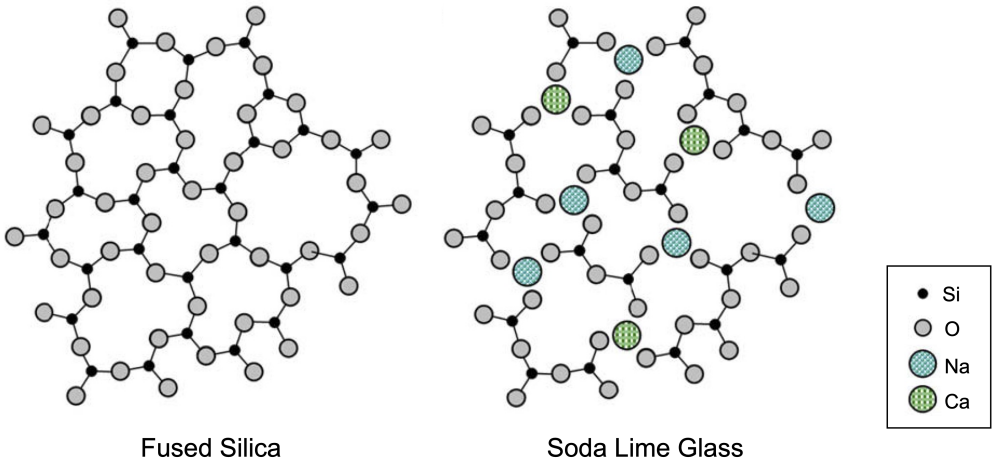

Figure 5.5: Schematic representation of fused silica and soda lime glass atomic network. In SLG, the Si atoms are replaced by Na and Ca ions, which act as network modifiers. Image taken from [18].

To spot for any polymorphic changes in the FS nanopillars, TEM sample from top to bottom of the pillar compressed to 7.2 GPa normal stress (Pillar 3) was prepared by FIB, as shown in Fig. 5.6 (a) and (b). SEM image in Fig. 5.6 (b) reveal that excessive compression is accommodated inside the pillars through the formation of localized shear bands which are visible at the pillar surface. TEM

analysis was carried out using a FEI-Titan Scanning/Transmission Electron Microscope (STEM) operating at 300 kV. Using HRTEM and Fast Fourier Transform (FFT) analysis, no crystalline regions could be detected in the entire FS pillar (Fig. 5.6(c)), in contrast to our observations in SLG (Fig. 5.1 and 5.2).

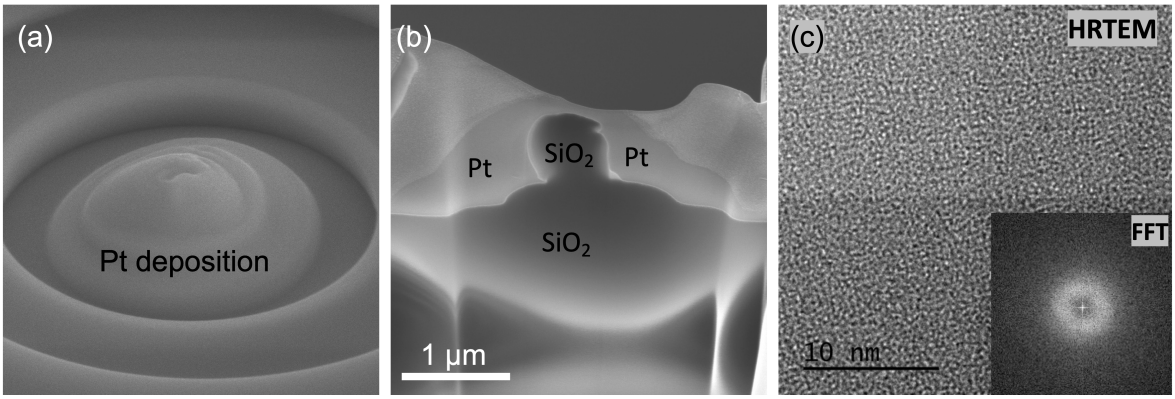

Figure 5.6: TEM analysis of Fused Silica nanopillars post compression. (a) shows deposition of Pt layer over the deformed pillar, followed by FIB slicing in (b) before mounting the entire sample on the TEM sample holder. (c) shows the HRTEM image of the pillar with FFT analysis. No crystalline regions could be observed in the entire pillar region.

5.2.2. Discussion and Conclusion

Formation of crystalline polymorphs of silica such as α-Quartz, Coesite and Stishovite from amorphous phase follows the aforementioned permanent densification process as the pressure or temperature or both are increased beyond a threshold [169]. In pure amorphous SiO_2 (i.e. FS), the pressure threshold for crystallization is known to be ∼34 GPa [138]. Interestingly, SLG (which is ∼70 % pure SiO_2) is shown to be able to crystallize at ∼7 GPa at macroscopic scale (ref. sec. 4.4) and at ∼4 GPa at submicron scale (ref. sec. 5.1.2). Hence, when the size is reduced from macro to micron scale, the pressure threshold for stishovite formation in SLG is reduced by 40%. As presented in this chapter, no such observations could be made in FS at similar stress levels. Therefore, there is a clear effect of microstructure along with domain size which facilitates crystallization in SLG

plates and nanopillars at lower stress levels, as explained in previous sections (sec. 4.4 and 5.1). The highly compact structure and lack of mobile ions in FS requires higher pressure / stress levels to increase Si coordination number from 4 to 6 to achieve crystalline stishovite phase. If one assumes that reducing domain size to micron levels can reduce pressure threshold of stishovite formation by 40% in FS (same as SLG), the required pressure at micron scale would be at least 13.6 GPa (40% of 34 GPa). Such stress levels could not be achieved under uniaxial nanopillar compression even at 60% strain levels, reported in this chapter. Potentially, this could be achieved either by reducing the pillar diameter even below 100 nm or applying shock loading via high speed plate impact experiments on the pillars. One advantage of the plate impact experiments is that very high stress levels can be achieved by increasing the impact speeds ([17, 171, 172]). This potential research was explored and the results are presented in the next chapter.

In conclusion, quasistatic uniaxial compression tests were performed on fused silica nanopillars of diameter $\sim$500 nm with remarkable plastic strains reaching up to 60%. Significant shear banding was observed and brittle failure was completely suppressed. HRTEM analysis of the entire deformed pillar did not reveal any crystallization in FS, which is a stark difference from the SLG behavior. Such behavior is attributed to insufficient stress levels achieved in micro-compression of FS given its highly compact microstructure.

Chapter 6. Polymorphic Activity in Silica Glass Micropillars under Shock Compression

Formation of crystalline phases such as Stishovite in fused silica occurs under extreme conditions of pressure, temperature and / or strain rates. This is commonly observed during meteorite strike in nature, shape charge explosions or bullet strike on glass windows. In sec 5.1, we concluded that microscopic domain size could potentially reduce the pressure threshold for crystal formation in silica glass. However, the highly compact molecular structure in fused silica still requires higher stress levels than those achieved in quasistatic compression at sub-micron scale (sec. 5.2). Thus, shock compression via plate impact would be an obvious choice to achieve the required high stress levels. This is because the stress in material under shock is directly proportional to impact speed of the flyer plate. Laser generated flyer plate impact setup has become a powerful tool in conducting table-top miniaturized planar shock wave experiments. The diameter and speed of the flyer plate can be easily controlled by adjusting the parameters of the launch pulse laser. In this chapter, we employ our previously developed table top flyer plate impact setup (sec. 4.2) to directly load micron sized pillars of fused silica with well-defined planar shock waves. Impact speeds and corresponding shock stresses achieved were in the range of 0.5-3.8 km/s and 3.5-30 GPa, respectively. The shocked micropillar samples were analyzed using X-ray diffraction and crystalline peaks corresponding to Stishovite were detected at stresses as low as 15.24 GPa. This is significantly below the 34 GPa threshold observed in bulk fused silica samples [138]. The low stress threshold for Stishovite formation is attributed to high shear flow in the pillars causing localized melting followed by rapid cooling due to large temperature gradient with the bulk material.

6.1. Sample Preparation

Fused Silica micropillars were made using the cleanroom process of photolithography. It was chosen over FIB due to its ability to make thousands of pillar structures over a large sample wafer in a significantly lesser time period. Another advantage is that all pillars are standing over the sample surface and can be directly impacted with the flyer plate, whereas in FIB all pillars are below the surface. The entire fabrication process via photolithography was completed in 9 steps, as explained in Fig. 6.1. These steps can be divided into 3 categories: deposition, exposure and etching. 3 and 4 inch commercial fused silica wafers, purchased from University Wafers Inc., were used as the starting sample. The target was to make pillars of diameter 3, 5, 10 and 15 μm with aspect ratio of 1. This could only be achieved by very deep and vertical etching of silica and hence required hard metal masks to be coated on the bare wafer. Hard masks serve the purpose of transferring the "user-designed" photomask pattern to wafer with very high selectivity. Al was selected as the hard mask as it has a selectivity of ∼20:1 with silica [173], meaning with every 20 nm etching of silica, only 1 nm of Al will be etched away. The thickness of the sputtered Al layer depended on the required fused silica pillar height, for example, for 15 μm height, Al layer had 800 nm thickness. In next steps, a positive photoresist was spin coated over the Al layer, followed by UV exposure through the photomask. The photomask was put in hard contact with photoresist coated face of the wafer during the exposure. The exposed part of the photoresist became cross-linked and the unexposed part was then dissolved away in the first step of the etching process. The pillar pattern was now available on the photoresist layer. Through two consecutive Deep Reactive Ion Etching (DRIE) processes, this pattern was first transferred to Al and then on to the fused silica. The final pattern achieved on the fused silica wafer is shown in Fig. 6.2. The pillars with identical dimensions

were grouped in either circular (or square) patterns of 1 mm diameter (or side).

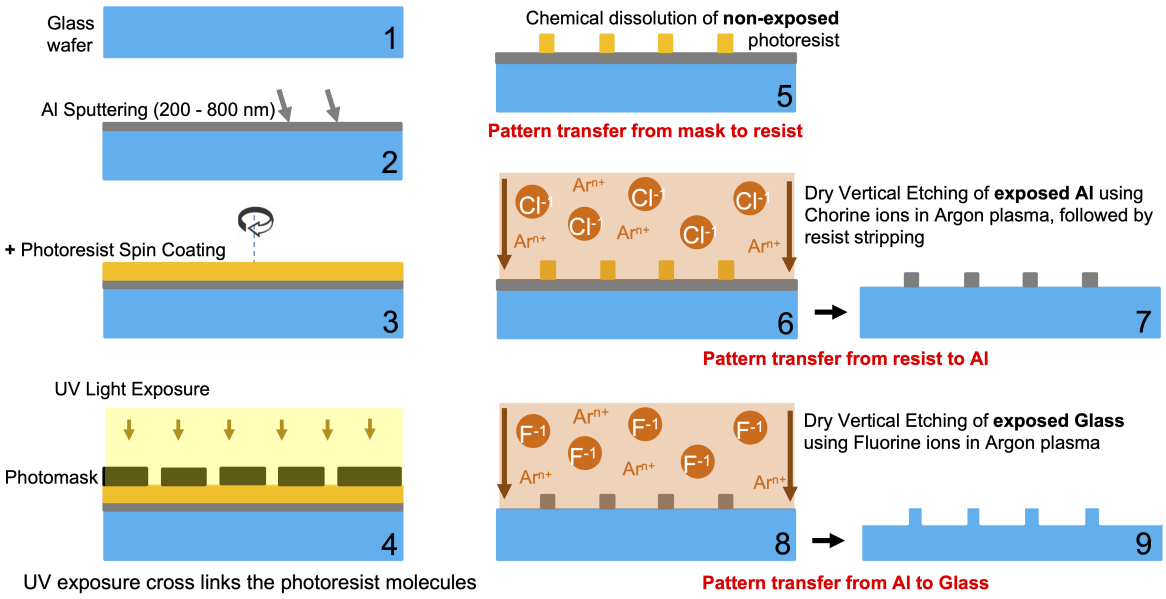

Figure 6.1: Fused silica micropillar fabrication via photolithography, completed in 9 steps, categorized under deposition (1-3), exposure (4), and etching (5-9).

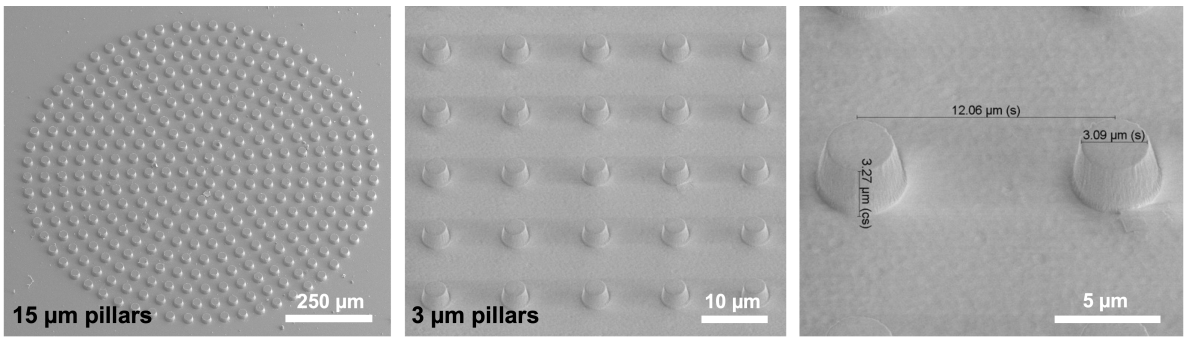

Figure 6.2: SEM images of the fused silica micropillars showing the pillar pattern achieved at the end of the photolithography process.

6.2. Experimental Setup and Results

Shock compression of the fused silica micropillars was performed using the previously described laser generated flyer plate impact setup. A schematic of the setup along with the cross section view of the sample assembly is shown in Fig. 6.3. The 3 and 4 inch fused silica wafers were diced into smaller pieces of 15 mm x 15 mm. In each impact experiment, one such piece was placed inside

the sample assembly (Fig. 6.3 (b)) flushed with the PMMA window and pillar side facing the Al foil. The gap between the foil and the pillars was fixed to be ∼400 μm using precision spacers. The working mechanism of the setup was previously described in sec. 4.2. The only update from the previous setup is that the flyer diameters were now reduced to ∼ 800 μm by reducing the pulse laser focused spot size at the glass-foil interface. This increased the laser fluence and hence the maximum speed attained by flyer from 2.5 km/s to 3.8 km/s. Since the pillar patterns were spread over 1 mm regions, a 800 μm flyer ensured that only the pillars will be impacted and not the bulk material.

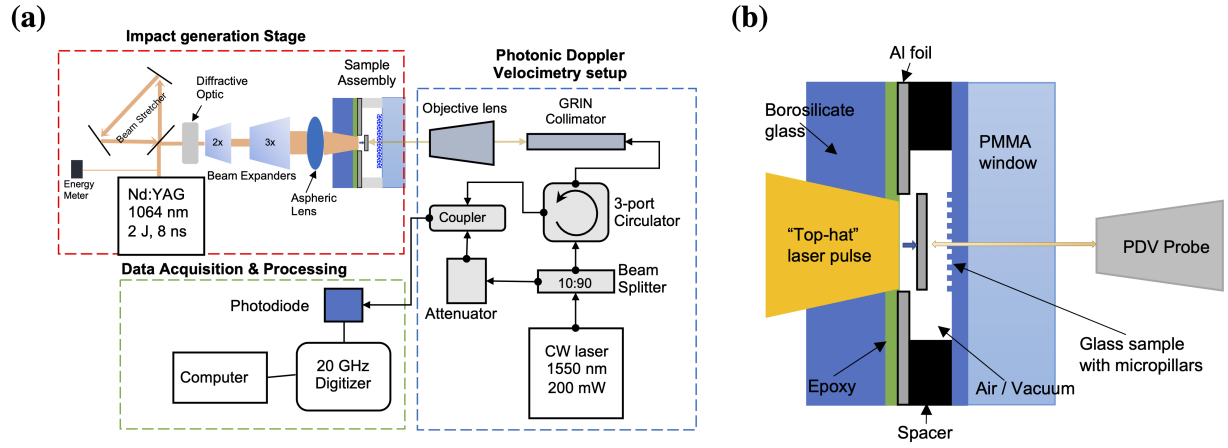

Figure 6.3: (a) Schematic of the laser generated flyer plate setup along with that of the Photonic Doppler Velocimeter (PDV). Black arrows in PDV setup denote single-mode optical fibers for 1550 nm wavelength. (b) Cross-sectional view of the fused silica micropillar sample assembly showing punching of the flyer disc by the impinging top-hat laser pulse, and the probe beam from PDV for measuring the flyer velocity.

Photonic Doppler Velocimeter (PDV) was used to record the entire flyer plate flight after launch and impact speeds from 500 m/s to 3.8 km/s were measured, depending on the launch laser energy. However, the PDV couldn't record any signal from the flyer post impact due to loss of its surface planarity upon impact with the pillars. As a result, no particle velocity (u_p) and shock velocity (U_s) could be measured from the signal. Fig 6.4 (a) and (b) show representative PDV signals and their velocity spectrograms when flyers impacted the micropillars at 2.5 km/s and 3.5 km/s, respectively.

Due to loss of signal post impact, there is no point of particle velocity visible in the spectrograms. Alternatively, impedance matching technique was used to calculate shock stress in the pillars using the Hugoniot equation of state parameters of the Al flyer and the fused silica sample, taken from [138, 174] and compiled in Table 6.1.

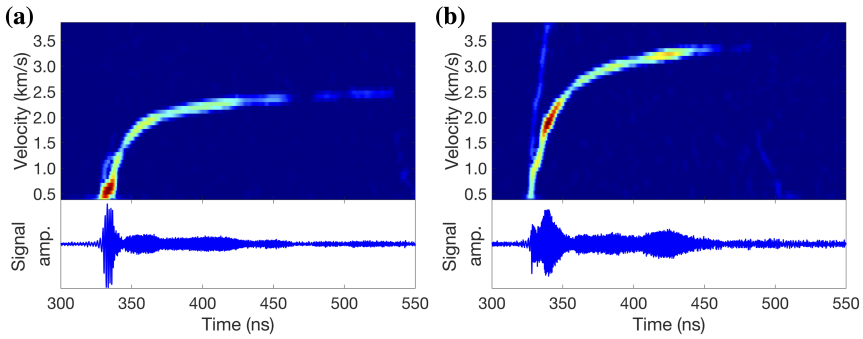

Figure 6.4: Representative PDV signal for shock compression of fused silica micropillars with flyers of impact speed (a) 2.5 km/s and (b) 3.5 km/s. After the point of impact, there is a complete loss of signal.

Fig. 6.5 (a) shows the impact face of the recovered flyer after the experiment where the impact speed was ∼500 m/s. At such low speeds, the flyer was still intact and the pillar pattern of the target sample was found to be indented on it. This confirmed a direct planar impact with the pillars. At speeds above 2 km/s, the flyer couldn't be recovered due to extensive damage suffered at high stress levels resulting from high impact speeds. The impact site of one such experiment is shown in Fig. 6.5 (b).

6.2.1. Impedance matching between flyer and micropillars

The following formulation to obtain the shock stress from known parameters from equation of state of the flyer and target material is taken from [172]. The shock stress is given as,

$$\sigma = \rho_0 u_p U_s \tag{6.1}$$

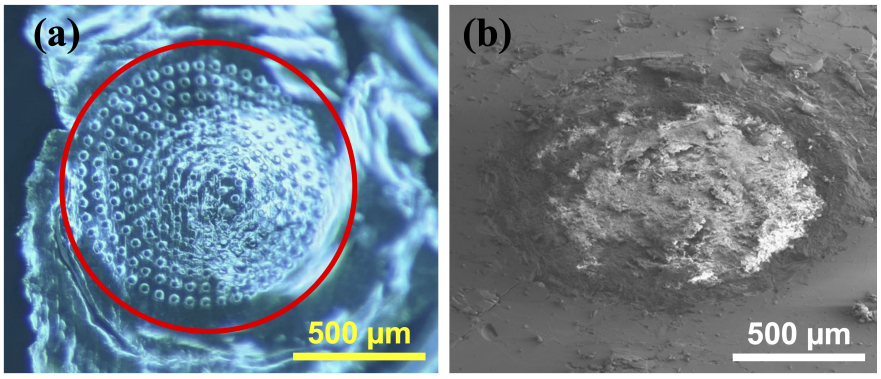

Figure 6.5: (a) Recovered flyer post impact with pillars at 500 m/s showing penetration of 15 µm pillars into the flyer. (b) SEM image of the impacted area on fused silica substrate with pieces of glass pillars scattered all over the area. Impact speed recorded was 2.5 km/s.

where, ρ_0 is the initial density, u_p and U_s are the particle and shock velocities in the material, respectively. There is a linear relationship between the particle and shock velocities,

$$U_s = C_0 + s u_p \tag{6.2}$$

where C_0 is the ambient pressure bulk sound velocity and s is a constant, given in Table 6.1. Lets denote flyer (Al) as material A and target (FS) as material B. Also assume that the flyer impact velocity is u_{fp} and the particle velocity in the target after impact is u_p. The backward moving particle velocity in the flyer can then be written as, $u_{pA} = u_{fp} - u_p$. Combining eqs. 6.1 and 6.2, the stress in flyer at the impact interface can calculated as,

$$\sigma_A = \rho_{0A} \left(u_{fp} - u_p\right) \left(C_{0A} + s_A (u_{fp} - u_p)\right) \tag{6.3}$$

Similarly, the impact stress in the target (FS) at the interface is given as,

$$\sigma_B = \rho_{0B} u_p \left(C_{0B} + s_B u_p\right) \tag{6.4}$$

Table 6.1: Shock and particle velocity parameters for the Al flyer and the fused silica target.

Material	C_0 (km/s)	s	u_p range (km/s)
Al 1100 (flyer) [174]	5.380	1.340	
Fused Silica (target) [138]	5.231 ± 0.030	-0.099 ± 0.019	$0.772 - 2.211$
	3.205 ± 0.165	0.855 ± 0.066	$2.245 - 2.728$

Since the stresses in both materials are equal at the interface, the two above equations can be equated to solve for u_p as follows,

$$u_p = (-x - \sqrt{x^2 - 4yz})/2y \tag{6.5}$$

where,

$$x = -C_{0A}\rho_{0A} - C_{0B}\rho_{0B} - 2s_A\rho_{0A}u_{fp} \tag{6.6}$$

$$y = s_A\rho_{0A} - s_B\rho_{0B} \tag{6.7}$$

$$z = u_{fp}\rho_{0A}\left(C_{0A} + s_A u_{fp}\right) \tag{6.8}$$

6.2.2. Polymorphic activity in fused silica micropillars

To spot for any polymorphic changes in the FS micropillars due to shock compression, post-impact samples (Fig. 6.5 (b)) were inspected using XRD scans and interestingly, peaks corresponding to Stishovite crystals were detected (Fig. 6.6) above certain threshold. The lowest impact speed at which Stishovite peaks were detected under XRD for 15 and 10 μm pillars was 2.5 km/s, whereas for 5 and 3 μm pillars it was 2.0 km/s. The corresponding impact stresses for 2.5 and 2.0 km/s were calculated to be 19.37 GPa and 15.24 GPa, respectively. Since the shock stress threshold for the formation of Stishovite in Fused Silica is 34 GPa [138], the XRD results prove that the microscale

domain size can reduce this threshold.

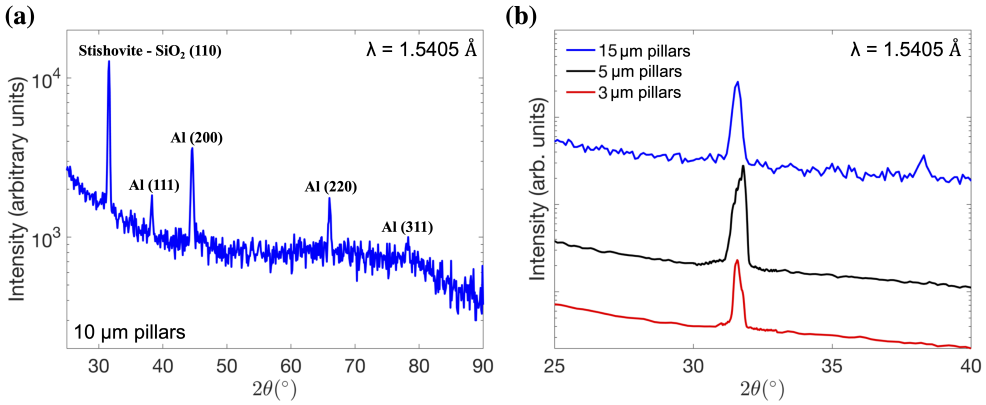

Figure 6.6: XRD scan of the impact zone showing Stishovite presence due to crystallization of the Fused Silica pillars. (a) shows the XRD results for the 10 μm pillars. Impact speed recorded was 2.5 km/s. Al peaks are due to the pieces of Al flyer stuck to the target as a result of laser pulse heating. (b) shows the XRD results for the 15, 5 and 3 μm pillars samples after flyer impact with speeds 2.5, 2.0 and 2.0 km/s, respectively. The peaks correspond to that of Stishovite.

6.3. Discussion

The above remarkable observations can be explained by two consecutively occurring mechanisms. First, there is structural heterogeneity associated with the micropillar pattern over the bulk material similar to "surface porosity". Such heterogeneity leads to localized high shear strains during shock compression causing tremendous frictional heating and hot spot formation [175–177]. Kowitz et al. [177] have shown that porous quartz can melt at shock pressures as low as 5 GPa as a result of hot spots in the veins of porous material, compared to 45 GPa required in bulk quartz single crystal. Second, there is nucleation of high-pressure phase crystals from these hot spots as they undergo rapid cooling due to large temperature gradient with the surrounding material [178, 179]. The cooling rate, which is highly sensitive to the domain size of the hot spot region, is critical as the temperature should reach below the melting point of the crystalline phase within the shock duration [180].

Both these mechanisms were analyzed in depth by Mansfeld et al. [156] by subjecting porous sandstone (quartz 89% by vol., porosity 25 - 30 %, pore size 20 - 100 μm) to planar shock compression to 7.5 and 12.5 GPa stress levels. They analyzed thin lamellas of the post-shock samples via back-scattered electron (BSE) and TEM imaging and confirmed presence of Stishovite crystals localized in amorphous silica veins. The size of the crystals ranged between 5 to 200 nm. The observed fluidic texture of the veins surrounding the crystals confirmed localized melting of quartz. The temperature within these veins would then be above the solidus of silica ($\sim$3000° C) much higher than that in surrounding material (500 - 1000° C for shock pressures 7.5 - 12.5 GPa). Such temperature gradient and microscopic size would cause rapid cooling of the vein to below the melting point of Stishovite within the shock duration causing it to crystallize.

Another important observation by Mansfeld et al. [156] was that the veins upto thickness of 700 nm and 1.5 μm were able to crystallize under 7.5 GPa and 12.5 GPa shock stress, respectively. This was attributed to slower rate of cooling in thicker veins leading to solidification time longer than the shock duration. Hence higher stress was required to raise the melting point and thereby reducing the solidification time. This would also explain why the 3 and 5 μm diameter pillars in our study were able to crystallize at 15.24 GPa whereas 10 and 15 μm pillars crystallized at 19.37 GPa.

6.4. Conclusion

Fused silica micropillars were shock loaded by impacting them using laser-generated and propelled 800 μm dia. Al microflyer plates of 25 μm thickness at 0.5 – 3.8 km/s. The stress state was determined by measuring the flyer speed by photonic doppler velocimetry and impedance matching between flyer and target. The shocked samples were analyzed using X-ray diffraction. Stishovite peaks were detected in 10 and 15 μm diameter pillar samples having impact stresses as low as 19.37

GPa, whereas in 3 and 5 μm pillars as low as 15.24 GPa. These stress levels are significantly below the crystallization threshold of 34 GPa observed in bulk fused silica. The reduction in pressure threshold for Stishovite formation is attributed to shear-driven localized hot spot formation within pillars which leads to melting, followed by rapid cooling due to large temperature gradient and small domain size of the pillars.

Chapter 7. Conclusions and Future Work

7.1. Summary

In this work, effect of domain size on the mechanical behavior of two different class of materials was studied: a crystalline metal (tungsten) and an amorphous compound (silica glass). Based on the previous works of dislocation dynamics simulations and laser shock experiments on metallic nanopilllars, a hypothesis was developed whether "decreasing domain size to microscale can be a proxy to increasing temperature". To validate this hypothesis, the two selected class of materials provided a much generalized approach and conclusion. The results and observations from this work would lead to development of advanced structural components with superior strength and ductility in NEMS/MEMS devices.

Tungsten (W) is a model BCC metal which is inherently brittle at macroscale. If the above hypothesis is true, W would behave in a ductile manner at micro scale. To explore this possibility, nano / micro characterization tests were performed on single crystal W, explained in chapter 2. Using focused ion beam (FIB) milling technique, pillars were carved out of a pristine W (100) sample. Their diameters were between 100 nm to 2 μm, with an aspect ratio of 3. In-situ SEM uniaxial compression tests were performed on the pillars and their stress strain behavior was recorded at three different strain rates of $10^{-3}, 10^{-2}$, and 10^{-1} s^{-1}. By analyzing the stress strain curves, the size effect on the complete picture of the strain-rate-controlled plastic flow behavior in W was revealed. We included not only the yield strength, but also the strain hardening rate, and the strain burst statistics. It was found that there is a critical size of 500 nm (pillar diameter) below which the plastic flow characteristics become strain rate independent.

The observed strain rate insensitivity was attributed to the potential ductile nature induced at small scale in BCC W, as a result of enhanced screw dislocation mobility under high flow stresses. This was further explored by analyzing the fracture behavior of W single crystal at nano / micro scale, presented in chapter 3. By employing FIB milling technique, notched cantilever samples of W (100) were made. The uncracked ligament was kept around 500 nm and 1 μm with the remaining dimensions scaled according to well defined ratios. The notch in each beam was oriented to investigate {110} cleavage plane of W, with the crack propagation direction towards <100>. As a result, the final crack orientation was {110}<100>. Bending test were performed using a cono-spherical indenter. Remarkably, stable crack growth was observed in all the notched samples, contrary to pure cleavage failure observed in macro sized tungsten samples. Elastic plastic fracture mechanics (EPFM) approach was employed to determine the conditional fracture toughness values ($K_{Q,J}$). These were conditional values because the size requirements of EPFM were not satisfied in our samples. For all the submicron samples, $K_{Q,J}$ values were obtained to be 11.76 ± 0.56 MPa $m^{1/2}$, which is lower than the macroscale K_{IC} value of 20.2 ± 5.5 MPa $m^{1/2}$ for {110} <100> crack orientation. As an alternative approach, maximum J values were taken from the resistance curves to obtain K_{Jmax} which, within experimental errors, were found to be in the range of K_{IC}. Hence, we concluded that the submicron sample sizes in our study were too small to obtain size independent material property of fracture toughness. Nevertheless, they are still crucial in providing a quantitative idea towards fracture behavior in similar sized structural components of W.

The combination of compression and bending experiments conclusively demonstrate that W can behave in a ductile manner at room temperature when its characteristic length scale is reduced to below 1 μm. The key mechanisms behind this phenomenon were found to be the enhanced mobility

of screw dislocations, driven by extremely high stress levels. Additionally, increased dominance of mixed dislocations was observed whose mobility is controlled by phonon drag and less dependent on thermal activation. The experimental data was consistent with the above mechanism that was uncovered by the DDD simulations [10, 110].

For the second class of materials, i.e., amorphous silica glasses, the phenomenon of high-pressure crystalline phase (Stishovite) formation was investigated. A series of quasi-static and shock compression experiments were conducted on fused silica (FS, 100% SiO_2) and soda lime glass (SLG, 70% SiO_2) samples. Since Stishovite is formed under extreme conditions of pressure, temperature and strain rate, a laser-generated flyer plate impact setup was developed (chapter 4). This setup is capable of achieving impact speeds between 0.5 - 3.5 km/s and results in a planar shock wave of 8 and 16 ns duration. FS is known to undergo phase transition to crystalline Stishovite at shock stress of 34 GPa. However, no such threshold is known for the SLG material. Therefore, we started with shock compression experiments on SLG plates and analyzed the post-shocked samples using transmission electron microscopy (TEM). A stress threshold value of 7 GPa for Stishovite nucleation was found. This is the first report of Stishovite nucleation stress in the SLG material. Diffusion of cationic impurities under localized shear and friction heating is attributed to such a low crystallization stress in SLG.

In order to uncover the size effect on the polymorphic activity in silica glasses, uniaxial compression tests were performed on FS and SLG nanopillars. The sample fabrication was conducted via FIB milling. The diameters of these pillars were 500 nm, with aspect ratio between 2 - 3. As presented in chapter 5, both materials showed unprecedented plastic flow with strains reaching above 50% and a complete absence of brittle failure. Furthermore, TEM analysis of

deformed SLG pillars revealed 4 nm regions of Stishovite crystals. The corresponding stress for this transformation was estimated to be only 4.2 GPa, which is 40% of the stishovite nucleation stress of 7 GPa observed in macroscale samples. The diffusion of cationic impurities under very high shear stresses in the SLG pillars is explained as the key mechanism for such a low stishovite nucleation stress. Interestingly, no Stishovite crystals were observed in any of the FS TEM samples, regardless of the pillar size, where the maximum stress was limited to only 7.2 GPa.

To further increase the stress levels in FS at microscale, the laser generated flyer plate impact setup was employed (chapter 6). FS pillars of diameters 3, 5, 10 and 15 μm and aspect ratio of 1 were fabricated using photolithography process. These pillars were arranged in a 1 mm sized pattern and shock loaded with flyer plate of diameter 0.8 mm and thickness 25 μm. The impact speeds were between 0.5 to 3.8 km/s resulting in estimated shock stresses of 3.5 to 30 GPa inside the pillars. By analyzing the post impact samples under X-ray diffraction, Stishovite's presence was detected in all the samples over certain thresholds. 3 and 5 μm pillars showed Stishovite peaks under XRD for impact over 15.24 GPa, whereas the threshold for 10 and 15 μm pillars was 19.37 GPa. This size dependent polymorphic behavior was attributed to the localized high shear in the pillars leading to significantly higher temperatures, compared to the bulk. The microscopic size of the pillars led to rapid cooling of the silica melt within the shock duration causing Stishovite to form inside the pillars.

In conclusion, throughout this work, a common theme of size effect at microscale was explored. Ductility was observed in tungsten and low-pressure crystallization of high-pressure Stishovite phase was detected in silica glasses. Based on the series of results obtained in both materials, it can now be stated that reducing domain size to micro scales is indeed a proxy to increasing temperature.

7.2. Future Work

7.2.1. Shock compression of tungsten at small scales under extreme conditions

Due to sluggish movement of screw dislocations in BCC metals, increasing strain rate of loading or reducing temperature below ambient induces more brittle behavior in these metals. It is therefore interesting to see if W can maintain its ductile behavior at micro scale even at ultra high strain rates and under cryogenic temperatures. Preliminary experiments were performed where FIB manufactured pillars (diameter 500 nm, AR = 3) were shock loaded directly with the flyer plate impact, as shown in Fig. 7.1. The SEM images of the shocked samples revealed significant plastic deformation and complete absence of brittle failure. It should be noted that the strain rates in this experiment were $>10^8$ s^{-1}. Further experiments need to be performed with different pillar sizes ranging from 100 nm to 5 μm to systematically study this effect. The test temperature can also be varied by precooling the samples to very low temperatures before loading. Such detailed investigation with varying testing conditions should uncover the limitations, if any, of the size induced ductility in W.

7.2.2. TEM investigation of dislocation mechanisms in tungsten

All the improved material properties of W at small scales, discussed in this work, rely on the size dependent dislocation behavior. The mechanisms by which the screw, edge and mixed dislocations influence BCC W's plastic behavior has so far only been explored via Discrete Dislocation Dynamics Simulations (DDD) [10, 110]. Therefore, there is a lack of visual confirmations of such mechanisms. Following future experiments are proposed to validate the DDD simulation results:

1. TEM imaging of post-compression W pillars of diameters 500 nm and 2 μm at strain rates of

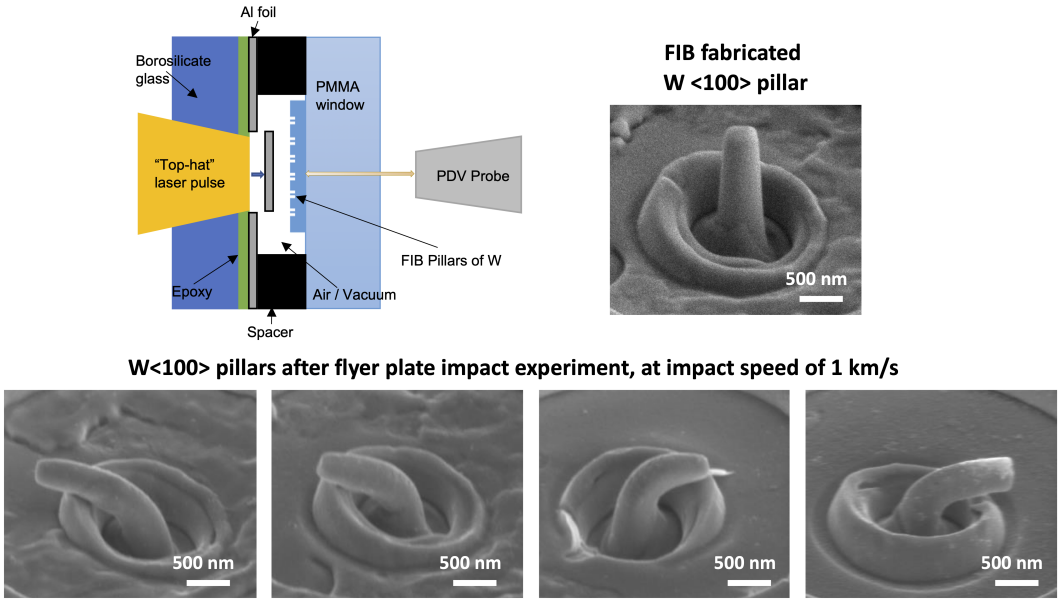

Figure 7.1: Shock loading of tungsten nanopillars (diameter 500 nm and aspect ratio of 3), via laser generated flyer plate impact, at impact speed of 1 km/s.

10^{-3} and 10^{-1} s^{-1}.

2. In-situ TEM compression of W pillars of diameters less than 200 nm, as they are thin enough to be electron transparent.

3. TEM imaging of shock loaded W pillars (Fig. 7.1).

In all the above proposed TEM works, aim should be to image and identify dislocations present in the sample. Their densities should be computed and compared with the densities obtained from the TEM images of undeformed W pillars of similar sizes. These investigations could reveal that the storage capability and the influence of screw dislocations are indeed diminished in micro scale samples.

7.2.3. Upgrading the laser generated flyer plate impact setup and shock compression of nano and micro-structured glass

As discussed in chapters 4 and 6, the phase transformation in amorphous soda lime glass and fused silica micropillars to the crystalline Stishovite at low shock stresses happens due to the formation of shear-induced localized hotspots formation. This hypothesis has been supported by either inspection of post compression samples via TEM where evidence of local melting was observed [156], or via MD simulations [158]. No in-situ temperature measurements have been performed to confirm any localized heating. We therefore propose employing the in-situ shock temperature measurement setup developed for miniature flyer plate impact experiment of reactive materials [181]. A schematic of the setup is shown in Fig. 7.2 and the working mechanism is explained by Bassett et al. [182].

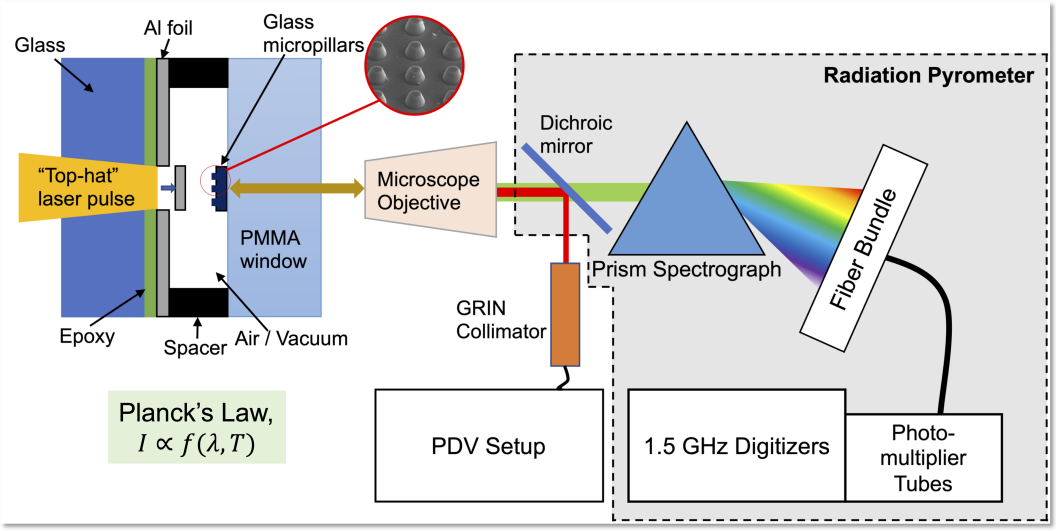

Figure 7.2: In-situ shock temperature measurement setup, enclosed by dotted lines. The setup serves as an attachment to the existing laser generated flyer plate setup and the photonic doppler velocimeter (PDV) and shares the same probe as the PDV.

The formation of high-density Stishovite phase at low stress provides a great opportunity to develop microstructured glass as ballistic armor material. Further ways should therefore be explored to make such silica glass-based structures outside the cleanroom lab environment. Significant

progress has been made in this field, especially in the development of nanoporous (NP) silica. The steps of fabrication can be found in the research work published by Marszewski et al. [183]. These are free standing porous slabs of fused silica and have remarkable thermal insulation properties. Efforts have been put towards characterizing the hardness and strength properties of NP silica [184]. Future work should focus on establishing the shock response and Hugoniot equation of state of NP silica. Shock compression via flyer plate impact on the NP slabs, with in-situ pressure and temperature measurements, could lead to very interesting observations. The post shock samples can be analyzed under X-ray diffraction and high resolution TEM to detect and visualize any polymorphic activities.

References

[1] AS Argon and SR Maloof. Plastic deformation of tungsten single crystals at low temperatures. *Acta metallurgica*, 14(11):1449–1462, 1966.

[2] RH Schnitzel. Deformation of tungsten single crystals from- 77° c to 800° c. *Journal of the Less Common Metals*, 8(2):81–89, 1965.

[3] H Conrad and W Hayes. Correlation of the thermal component of the yield stress of body centered cubic metals. Technical report, AEROSPACE CORP EL SEGUNDO CA, 1963.

[4] Michael D Uchic, Paul A Shade, and Dennis M Dimiduk. Plasticity of micrometer-scale single crystals in compression. *Annual Review of Materials Research*, 39:361–386, 2009.

[5] Ju-Young Kim, Dongchan Jang, and Julia R Greer. Tensile and compressive behavior of tungsten, molybdenum, tantalum and niobium at the nanoscale. *Acta Materialia*, 58(7): 2355–2363, 2010.

[6] Michael Zaiser, Jan Schwerdtfeger, AS Schneider, CP Frick, Blythe Gore Clark, PA Gruber, and Eduard Arzt. Strain bursts in plastically deforming molybdenum micro-and nanopillars. *Philosophical Magazine*, 88(30-32):3861–3874, 2008.

[7] David Cereceda, Martin Diehl, Franz Roters, Dierk Raabe, J Manuel Perlado, and Jaime Marian. Unraveling the temperature dependence of the yield strength in single-crystal tungsten using atomistically-informed crystal plasticity calculations. *International Journal of Plasticity*, 78:242–265, 2016.

[8] Brady G Butler, James D Paramore, Jonathan P Ligda, Chai Ren, Z Zak Fang, Scott C Middlemas, and Kevin J Hemker. Mechanisms of deformation and ductility in tungsten–a review. *International Journal of Refractory Metals and Hard Materials*, 75:248–261, 2018.

[9] Shuhei Shinzato, Masato Wakeda, and Shigenobu Ogata. An atomistically informed kinetic monte carlo model for predicting solid solution strengthening of body-centered cubic alloys. *International Journal of Plasticity*, 2019.

[10] Yinan Cui, Giacomo Po, and Nasr Ghoniem. Temperature insensitivity of the flow stress in body-centered cubic micropillar crystals. *Acta Materialia*, 108:128–137, 2016.

[11] Oscar Torrents Abad, Jeffrey M Wheeler, Johann Michler, Andreas S Schneider, and Eduard Arzt. Temperature-dependent size effects on the strength of ta and w micropillars. *Acta Materialia*, 103:483–494, 2016.

[12] Ryan Scott Crum. *Ultra-high strain rate behavior of FCC nanostructures*. PhD thesis, UCLA, 2016.

[13] Dariush Seif, Giacomo Po, Ryan Crum, Vijay Gupta, and Nasr M Ghoniem. Shock-induced plasticity and the hugoniot elastic limit in copper nano films and rods. *Journal of Applied Physics*, 115(5):054301, 2014.

[14] HA Colorado, A Navarro, SV Prikhodko, JM Yang, N Ghoniem, and V Gupta. Ultrahigh strain-rate bending of copper nanopillars with laser-generated shock waves. *Journal of Applied Physics*, 114(23):233510, 2013.

[15] M Rieth, JL Boutard, Sergei L Dudarev, T Ahlgren, S Antusch, Nadine Baluc, M-F Barthe,

CS Becquart, L Ciupinski, JB Correia, et al. Review on the efda programme on tungsten materials technology and science. *Journal of Nuclear Materials*, 417(1-3):463–467, 2011.

[16] Roshdy G Barsoum, Philip J Dudt, Syed Qadri, and William Ferrando. Polymorphic activity generated in soda-lime glass at hyper-velocity impact. In *29th International Symposium on Ballistics*, 2016.

[17] Joshua E Gorfain, C Scott Alexander, and Christopher T Key. High-pressure shock response and phase transition of soda-lime glass. In *AIP Conference Proceedings*, volume 2272, page 100011. AIP Publishing LLC, 2020.

[18] C Scott Alexander, LC Chhabildas, WD Reinhart, and DW Templeton. Changes to the shock response of fused quartz due to glass modification. *International Journal of Impact Engineering*, 35(12):1376–1385, 2008.

[19] Prithachakaran Renganathan, Thomas S Duffy, and Yogendra M Gupta. Hugoniot states and optical response of soda lime glass shock compressed to 120 gpa. *Journal of Applied Physics*, 127(20):205901, 2020.

[20] Norimasa Nishiyama, Fumihiro Wakai, Hiroaki Ohfuji, Yusuke Tamenori, Hidenobu Murata, Takashi Taniguchi, Masafumi Matsushita, Manabu Takahashi, Eleonora Kulik, Kimiko Yoshida, et al. Fracture-induced amorphization of polycrystalline sio2 stishovite: a potential platform for toughening in ceramics. *Scientific reports*, 4(1):1–8, 2014.

[21] Charles Meade, Russel J Hemley, and HK Mao. High-pressure x-ray diffraction of sio 2 glass. *Physical Review Letters*, 69(9):1387, 1992.

[22] Paul F McMillan and George H Wolf. Vibrational spectroscopy of silicate liquids. *Reviews in Mineralogy and Geochemistry*, 32(1):247–315, 1995.

[23] Chang-Sheng Zha, Russell J Hemley, Ho-kwang Mao, Thomas S Duffy, and Charles Meade. Acoustic velocities and refractive index of sio 2 glass to 57.5 gpa by brillouin scattering. *Physical Review B*, 50(18):13105, 1994.

[24] Michael Guerette, Michael R Ackerson, Jay Thomas, Fenglin Yuan, E Bruce Watson, David Walker, and Liping Huang. Structure and properties of silica glass densified in cold compression and hot compression. *Scientific reports*, 5(1):1–10, 2015.

[25] T Dümmer, JC Lasalvia, GJAM Ravichandran, and MA Meyers. Effect of strain rate on plastic flow and failure in polycrystalline tungsten. *Acta Materialia*, 46(17):6267–6290, 1998.

[26] R Gröger, AG Bailey, and V Vitek. Multiscale modeling of plastic deformation of molybdenum and tungsten: I. atomistic studies of the core structure and glide of $1/2 < 111 >$ screw dislocations at 0 k. *Acta Materialia*, 56(19):5401–5411, 2008.

[27] Pascale El Ters and Mutasem A Shehadeh. Modeling the temperature and high strain rate sensitivity in bcc iron: Atomistically informed multiscale dislocation dynamics simulations. *International Journal of Plasticity*, 112:257–277, 2019.

[28] Yinan Cui, Giacomo Po, and Nasr Ghoniem. Controlling strain bursts and avalanches at the nano-to micrometer scale. *Physical review letters*, 117(15):155502, 2016.

[29] Rui Huang, Qing-Jie Li, Zhang-Jie Wang, Ling Huang, Ju Li, Evan Ma, and Zhi-Wei Shan. Flow stress in submicron bcc iron single crystals: sample-size-dependent strain-rate

sensitivity and rate-dependent size strengthening. *Materials Research Letters*, 3(3):121–127, 2015.

[30] Q Wei, T Jiao, KT Ramesh, E Ma, LJ Kecskes, L Magness, R Dowding, VU Kazykhanov, and RZ Valiev. Mechanical behavior and dynamic failure of high-strength ultrafine grained tungsten under uniaxial compression. *Acta Materialia*, 54(1):77–87, 2006.

[31] YM Wang and E Ma. Strain hardening, strain rate sensitivity, and ductility of nanostructured metals. *Materials Science and Engineering: A*, 375:46–52, 2004.

[32] GM Cheng, WW Jian, WZ Xu, H Yuan, PC Millett, and YT Zhu. Grain size effect on deformation mechanisms of nanocrystalline bcc metals. *Materials Research Letters*, 1(1): 26–31, 2013.

[33] Lei Cao and Marisol Koslowski. Rate-limited plastic deformation in nanocrystalline ni. *Journal of Applied Physics*, 117(24):244301, 2015.

[34] Alan Xu, Michael Saleh, Joel Davis, Lyndon Edwards, and Dhriti Bhattacharyya. In-situ micro-tensile investigation of strain rate response along $< 100 >$ and $< 110 >$ directions in single crystal nickel. *International Journal of Plasticity*, 106:129–144, 2018.

[35] YN Cui, P Lin, ZL Liu, and Z Zhuang. Theoretical and numerical investigations of single arm dislocation source controlled plastic flow in fcc micropillars. *International journal of plasticity*, 55:279–292, 2014.

[36] George Z Voyiadjis and Yooseob Song. Strain gradient continuum plasticity theories: theoretical, numerical and experimental investigations. *International Journal of Plasticity*, 2019.

[37] Wei Chen, Zaiwang Huang, Shuo Cao, Yan Pan, Mingda Huang, Qingmiao Hu, Ding Xu, Qiaoyan Sun, Lin Xiao, and Jun Sun. Strain rate-induced plasticity in bcc β-ti alloy single crystal micropillars containing brittle ω-precipitates. *Materials & Design*, 137:404–413, 2018.

[38] M-Carmen Miguel, Alessandro Vespignani, Stefano Zapperi, Jérôme Weiss, and Jean-Robert Grasso. Intermittent dislocation flow in viscoplastic deformation. *Nature*, 410(6829):667, 2001.

[39] Michael Zaiser. Scale invariance in plastic flow of crystalline solids. *Adv. Phys.*, 55(1-2): 185–245, 2006.

[40] K.S. Ng and A.H.W. Ngan. Stochastic nature of plasticity of aluminum micro-pillars. *Acta Materialia*, 56(8):1712 – 1720, 2008.

[41] Stefanos Papanikolaou, Yinan Cui, and Nasr Ghoniem. Avalanches and plastic flow in crystal plasticity: an overview. *Modelling and Simulation in Materials Science and Engineering*, 26 (1):013001, 2017.

[42] R Maass and PM Derlet. Micro-plasticity and recent insights from intermittent and small-scale plasticity. *Acta Materialia*, 143:338–363, 2018.

[43] Stefanos Papanikolaou, Hengxu Song, and Erik Van der Giessen. Obstacles and sources in dislocation dynamics: Strengthening and statistics of abrupt plastic events in nanopillar compression. *Journal of the Mechanics and Physics of Solids*, 102:17–29, 2017.

[44] SS Jiang, KF Gan, YJ Huang, P Xue, ZL Ning, JF Sun, and AHW Ngan. Stochastic

deformation and shear transformation zones of the glassy matrix in cuzr-based metallic-glass composites. *International Journal of Plasticity*, 2019.

[45] Xiaoyue Ni, Haolu Zhang, Danilo B Liarte, Louis W McFaul, Karin A Dahmen, James P Sethna, and Julia R Greer. Yield precursor dislocation avalanches in small crystals: the irreversibility transition. *Physical review letters*, 123(3):035501, 2019.

[46] James P Sethna, Karin A Dahmen, and Christopher R Myers. Crackling noise. *Nature*, 410 (6825):242, 2001.

[47] Steffen Brinckmann, Ju-Young Kim, and Julia R Greer. Fundamental differences in mechanical behavior between two types of crystals at the nanoscale. *Physical review letters*, 100(15):155502, 2008.

[48] Gregory Sparks and Robert Maass. Shapes and velocity relaxation of dislocation avalanches in au and nb microcrystals. *Acta Materialia*, 152:86–95, 2018.

[49] Stefanos Papanikolaou, Dennis M Dimiduk, Woosong Choi, James P Sethna, Michael D Uchic, Christopher F Woodward, and Stefano Zapperi. Quasi-periodic events in crystal plasticity and the self-organized avalanche oscillator. *Nature*, 490(7421):517, 2012.

[50] Hengxu Song, Dennis Dimiduk, and Stefanos Papanikolaou. Universality class of nanocrystal plasticity: Localization and self-organization in discrete dislocation dynamics. *Physical review letters*, 122(17):178001, 2019.

[51] Hengxu Song and Stefanos Papanikolaou. From statistical correlations to stochasticity and size effects in sub-micron crystal plasticity. *Metals*, 9(8):835, 2019.

[52] G Sparks and R Maaß. Nontrivial scaling exponents of dislocation avalanches in microplasticity. *Physical Review Materials*, 2(12):120601, 2018.

[53] G Sparks, Y Cui, G Po, Q Rizzardi, J Marian, and R Maaß. Avalanche statistics and the intermittent-to-smooth transition in microplasticity. *Physical Review Materials*, 3(8):080601, 2019.

[54] Ling Huang, Qing-Jie Li, Zhi-Wei Shan, Ju Li, Jun Sun, and Evan Ma. A new regime for mechanical annealing and strong sample-size strengthening in body centred cubic molybdenum. *Nature communications*, 2:547, 2011.

[55] AS Schneider, D Kaufmann, BG Clark, CP Frick, PA Gruber, R Mönig, O Kraft, and E Arzt. Correlation between critical temperature and strength of small-scale bcc pillars. *Physical review letters*, 103(10):105501, 2009.

[56] Ju-Young Kim, Dongchan Jang, and Julia R Greer. Insight into the deformation behavior of niobium single crystals under uniaxial compression and tension at the nanoscale. *Scripta Materialia*, 61(3):300–303, 2009.

[57] Halil Yilmaz, Craig J Williams, Jared Risan, and Brian Derby. The size dependent strength of fe, nb and v micropillars at room and low temperature. *Materialia*, 7:100424, 2019.

[58] AB Hagen, BD Snartland, and C Thaulow. Temperature and orientation effects on the deformation mechanisms of α-fe micropillars. *Acta Materialia*, 129:398–407, 2017.

[59] Marc Bielmann, Uday Mahajan, and Rajiv K Singh. Effect of particle size during tungsten chemical mechanical polishing. *MRS Online Proceedings Library Archive*, 566, 1999.

[60] CP Frick, BG Clark, S Orso, AS Schneider, and E Arzt. Size effect on strength and strain hardening of small-scale [1 1 1] nickel compression pillars. *Materials Science and Engineering: A*, 489(1-2):319–329, 2008.

[61] CA Volkert, ET Lilleodden, D Kramer, and J Weissmüller. Approaching the theoretical strength in nanoporous au. *Applied Physics Letters*, 89(6):061920, 2006.

[62] Julia R Greer and Jeff Th M De Hosson. Plasticity in small-sized metallic systems: Intrinsic versus extrinsic size effect. *Progress in Materials Science*, 56(6):654–724, 2011.

[63] Haitao Zhang, Brian E Schuster, Qiuming Wei, and Kaliat T Ramesh. The design of accurate micro-compression experiments. *Scripta Materialia*, 54(2):181–186, 2006.

[64] JY Zhang, X Liang, P Zhang, K Wu, G Liu, and J Sun. Emergence of external size effects in the bulk-scale polycrystal to small-scale single-crystal transition: A maximum in the strength and strain-rate sensitivity of multicrystalline cu micropillars. *Acta materialia*, 66:302–316, 2014.

[65] Cynthia M Byer and KT Ramesh. Effects of the initial dislocation density on size effects in single-crystal magnesium. *Acta materialia*, 61(10):3808–3818, 2013.

[66] AS Schneider, CP Frick, BG Clark, PA Gruber, and E Arzt. Influence of orientation on the size effect in bcc pillars with different critical temperatures. *Materials Science and Engineering: A*, 528(3):1540–1547, 2011.

[67] Marta Pozuelo, Jacob W Stremfel, Jenn-Ming Yang, and Jaime Marian. Strengthening to softening transition in lath martensite. *Materialia*, 5:100254, 2019.

[68] Q Wei, S Cheng, KT Ramesh, and E Ma. Effect of nanocrystalline and ultrafine grain sizes on the strain rate sensitivity and activation volume: fcc versus bcc metals. *Materials Science and Engineering: A*, 381(1-2):71–79, 2004.

[69] R. Gu and A. H. W. Ngan. Dislocation arrangement in small crystal volumes determines power-law size dependence of yield strength. *Journal of the Mechanics & Physics of Solids*, 61(6):1531–1542, 2013.

[70] Cynthia Ann Volkert and Erica T Lilleodden. Size effects in the deformation of sub-micron au columns. *Philosophical Magazine*, 86(33-35):5567–5579, 2006.

[71] Yinan Cui, Giacomo Po, Pratyush Srivastava, Katherine Jiang, Vijay Gupta, and Nasr Ghoniem. The role of slow screw dislocations in controlling fast strain avalanche dynamics in body-centered cubic metals. *International Journal of Plasticity*, 2019.

[72] DM Dimiduk, MD Uchic, and TA Parthasarathy. Size-affected single-slip behavior of pure nickel microcrystals. *Acta Materialia*, 53(15):4065–4077, 2005.

[73] Shun Xu, Dongyue Xie, Guisen Liu, Kaisheng Ming, and Jian Wang. Quantifying the resistance to dislocation glide in single phase fecral alloy. *International Journal of Plasticity*, 132:102770, 2020. ISSN 0749-6419. doi: https://doi.org/10.1016/j.ijplas.2020.102770.

[74] DM Dimiduk, MD Uchic, SI Rao, C Woodward, and TA Parthasarathy. Overview of experiments on microcrystal plasticity in fcc-derivative materials: selected challenges for modelling and simulation of plasticity. *Modell. Simul. Mater. Sci. Eng.*, 15(2):135, 2007.

[75] Nir Friedman, Andrew T Jennings, Georgios Tsekenis, Ju-Young Kim, Molei Tao, Jonathan T Uhl, Julia R Greer, and Karin A Dahmen. Statistics of dislocation slip avalanches in nanosized

single crystals show tuned critical behavior predicted by a simple mean field model. *Physical review letters*, 109(9):095507, 2012.

[76] Jonathan T Uhl, Shivesh Pathak, Danijel Schorlemmer, Xin Liu, Ryan Swindeman, Braden AW Brinkman, Michael LeBlanc, Georgios Tsekenis, Nir Friedman, Robert Behringer, et al. Universal quake statistics: From compressed nanocrystals to earthquakes. *Sci. Rep.*, 5:16493, 2015.

[77] Yinan Cui, Giacomo Po, and Nasr Ghoniem. Influence of loading control on strain bursts and dislocation avalanches at the nanometer and micrometer scale. *Physical Review B*, 95(6): 064103, 2017.

[78] Ferenc F Csikor, Christian Motz, Daniel Weygand, Michael Zaiser, and Stefano Zapperi. Dislocation avalanches, strain bursts, and the problem of plastic forming at the micrometer scale. *Science*, 318(5848):251–254, 2007.

[79] R Maaß, M Wraith, JT Uhl, JR Greer, and KA Dahmen. Slip statistics of dislocation avalanches under different loading modes. *Physical review E*, 91(4):042403, 2015.

[80] Jeff Alstott, Ed Bullmore, and Dietmar Plenz. powerlaw: a python package for analysis of heavy-tailed distributions. *PloS one*, 9(1):e85777, 2014.

[81] Hongbin Bei, Sanghoon Shim, Easo P George, Michael K Miller, EG Herbert, and George Mathews Pharr. Compressive strengths of molybdenum alloy micro-pillars prepared using a new technique. *Scripta Materialia*, 57(5):397–400, 2007.

[82] Subin Lee, Jiwon Jeong, Youbin Kim, Seung Min Han, Daniel Kiener, and Sang Ho Oh.

Fib-induced dislocations in al submicron pillars: Annihilation by thermal annealing and effects on deformation behavior. *Acta Materialia*, 110:283–294, 2016.

[83] ZW Shan, Raja K Mishra, SA Syed Asif, Oden L Warren, and Andrew M Minor. Mechanical annealing and source-limited deformation in submicrometre-diameter ni crystals. *Nature materials*, 7(2):115–119, 2008.

[84] D Kiener and AM Minor. Source-controlled yield and hardening of cu (1 0 0) studied by in situ transmission electron microscopy. *Acta Materialia*, 59(4):1328–1337, 2011.

[85] Burghard von Blanckenhagen, Peter Gumbsch, and Eduard Arzt. Dislocation sources and the flow stress of polycrystalline thin metal films. *Philosophical Magazine Letters*, 83(1):1–8, 2003.

[86] Andrew T Jennings, Michael J Burek, and Julia R Greer. Microstructure versus size: mechanical properties of electroplated single crystalline cu nanopillars. *Physical review letters*, 104(13):135503, 2010.

[87] Julia R Greer, Warren C Oliver, and William D Nix. Size dependence of mechanical properties of gold at the micron scale in the absence of strain gradients. *Acta Materialia*, 53 (6):1821–1830, 2005.

[88] Q Wei, KT Ramesh, BE Schuster, LJ Kecskes, and RJ Dowding. Nanoengineering opens a new era for tungsten as well. *JOM*, 58(9):40–44, 2006.

[89] Xuan Zhang, Andrey Vyatskikh, Huajian Gao, Julia R Greer, and Xiaoyan Li. Lightweight, flaw-tolerant, and ultrastrong nanoarchitected carbon. *Proceedings of the National Academy of Sciences*, 116(14):6665–6672, 2019.

[90] Q Wei. Strain rate effects in the ultrafine grain and nanocrystalline regimes?influence on some constitutive responses. *Journal of materials science*, 42(5):1709–1727, 2007.

[91] J Hedworth and MJ Stowell. The measurement of strain-rate sensitivity in superplastic alloys. *Journal of Materials Science*, 6(8):1061–1069, 1971.

[92] D Jia, KT Ramesh, and E Ma. Effects of nanocrystalline and ultrafine grain sizes on constitutive behavior and shear bands in iron. *Acta materialia*, 51(12):3495–3509, 2003.

[93] Q Wei, KT Ramesh, E Ma, LJ Kesckes, RJ Dowding, VU Kazykhanov, and RZ Valiev. Plastic flow localization in bulk tungsten with ultrafine microstructure. *Applied Physics Letters*, 86(10):101907, 2005.

[94] Q Wei, T Jiao, SN Mathaudhu, E Ma, KT Hartwig, and KT Ramesh. Microstructure and mechanical properties of tantalum after equal channel angular extrusion (ecae). *Materials Science and Engineering: A*, 358(1-2):266–272, 2003.

[95] GA Malygin. Analysis of the strain-rate sensitivity of flow stresses in nanocrystalline fcc and bcc metals. *Physics of the Solid State*, 49(12):2266–2273, 2007.

[96] G Taylor. Thermally-activated deformation of bcc metals and alloys. *Progress in materials science*, 36:29–61, 1992.

[97] John E Dora and Stanley Rajnak. Nucleation of kink pairs and the peierls'mechanism of plastic deformation. 1963.

[98] AHW Ngan and M Wen. Atomistic simulation of energetics of motion of screw dislocations in bcc fe at finite temperatures. *Computational materials science*, 23(1-4):139–145, 2002.

[99] Giacomo Po, Yinan Cui, David Rivera, David Cereceda, Tom D Swinburne, Jaime Marian, and Nasr Ghoniem. A phenomenological dislocation mobility law for bcc metals. *Acta Materialia*, 119:123–135, 2016.

[100] Ulrich Fred Kocks, ARGON AS, and ASHBY MF. Thermodynamics and kinetics of slip. 1975.

[101] LJ Kecskes, KC Cho, RJ Dowding, BE Schuster, RZ Valiev, and Q Wei. Grain size engineering of bcc refractory metals: Top-down and bottom-up: Application to tungsten. *Materials Science and Engineering: A*, 467(1-2):33–43, 2007.

[102] J Riedle, P Gumbsch, HF Fischmeister, VG Glebovsky, and VN Semenov. Fracture studies of tungsten single crystals. *Materials Letters*, 20(5-6):311–317, 1994.

[103] JE Cordwell and D Hull. The brittle fracture of [100] axis tungsten single crystals. *Philosophical Magazine*, 19(161):951–966, 1969.

[104] D Hull, P Beardmore, and AP Valintine. Crack propagation in single crystals of tungsten. *The Philosophical Magazine: A Journal of Theoretical Experimental and Applied Physics*, 12(119):1021–1041, 1965.

[105] Peter Gumbsch, Joachim Riedle, Alexander Hartmaier, and Hellmut F Fischmeister. Controlling factors for the brittle-to-ductile transition in tungsten single crystals. *Science*, 282(5392):1293–1295, 1998.

[106] Armando Giannattasio and Steve G Roberts. Strain-rate dependence of the brittle-to-ductile transition temperature in tungsten. *Philosophical Magazine*, 87(17):2589–2598, 2007.

[107] Carsten Bonnekoh, Andreas Hoffmann, and Jens Reiser. The brittle-to-ductile transition in cold rolled tungsten: On the decrease of the brittle-to-ductile transition by 600 k to- 65 c. *International Journal of Refractory Metals and Hard Materials*, 71:181–189, 2018.

[108] Carsten Bonnekoh, Ute Jäntsch, Jan Hoffmann, Harald Leiste, Alexander Hartmaier, Daniel Weygand, Andreas Hoffmann, and Jens Reiser. The brittle-to-ductile transition in cold rolled tungsten plates: impact of crystallographic texture, grain size and dislocation density on the transition temperature. *International Journal of Refractory Metals and Hard Materials*, 78: 146–163, 2019.

[109] Jens Reiser, Jan Hoffmann, Ute Jäntsch, Michael Klimenkov, Simon Bonk, Carsten Bonnekoh, Michael Rieth, Andreas Hoffmann, and Tobias Mrotzek. Ductilisation of tungsten (w): On the shift of the brittle-to-ductile transition (bdt) to lower temperatures through cold rolling. *International Journal of Refractory Metals and Hard Materials*, 54:351–369, 2016.

[110] Yinan Cui, Giacomo Po, Pratyush Srivastava, Katherine Jiang, Vijay Gupta, and Nasr Ghoniem. The role of slow screw dislocations in controlling fast strain avalanche dynamics in body-centered cubic metals. *International journal of plasticity*, 124:117–132, 2020.

[111] Pratyush Srivastava, Katherine Jiang, Yinan Cui, Edgar Olivera, Nasr Ghoniem, and Vijay Gupta. The influence of nano/micro sample size on the strain-rate sensitivity of plastic flow in tungsten. *International Journal of Plasticity*, 136:102854, 2021.

[112] Joachim Riedle, Peter Gumbsch, and Hellmut F Fischmeister. Cleavage anisotropy in tungsten single crystals. *Physical review letters*, 76(19):3594, 1996.

[113] JE Cordwell and D Hull. Observation of $\{110\}$ cleavage in< 110> axis tungsten single crystals. *Philosophical Magazine*, 26(1):215–224, 1972.

[114] Peter Gumbsch. Brittle fracture and the brittle-to-ductile transition of tungsten. *Journal of Nuclear Materials*, 323(2-3):304–312, 2003.

[115] R Ayres and DF Stein. A dislocation dynamics approach to prediction of cleavage planes in bcc metals. *Acta Metallurgica*, 19(8):789–794, 1971.

[116] S Kohlhoff, P Gumbsch, and HF Fischmeister. Crack propagation in bcc crystals studied with a combined finite-element and atomistic model. *Philosophical Magazine A*, 64(4):851–878, 1991.

[117] Johannes Ast, Mathias Göken, and Karsten Durst. Size-dependent fracture toughness of tungsten. *Acta Materialia*, 138:198–211, 2017.

[118] C Bohnert, NJ Schmitt, SM Weygand, O Kraft, and R Schwaiger. Fracture toughness characterization of single-crystalline tungsten using notched micro-cantilever specimens. *International Journal of Plasticity*, 81:1–17, 2016.

[119] Stefan Wurster, Christian Motz, and Reinhard Pippan. Characterization of the fracture toughness of micro-sized tungsten single crystal notched specimens. *Philosophical Magazine*, 92(14):1803–1825, 2012.

[120] Johannes Ast, JJ Schwiedrzik, J Wehrs, D Frey, Mikhail Nikolayevich Polyakov, J Michler, and X Maeder. The brittle-ductile transition of tungsten single crystals at the micro-scale. *Materials & Design*, 152:168–180, 2018.

[121] James P Best, Johannes Zechner, Ivan Shorubalko, Jozef Vincenc Oboňa, Juri Wehrs, Marcus Morstein, and Johann Michler. A comparison of three different notching ions for small-scale fracture toughness measurement. *Scripta Materialia*, 112:71–74, 2016.

[122] Johannes Ast, Matteo Ghidelli, Karsten Durst, Mathias Göken, Marco Sebastiani, and Alexander M Korsunsky. A review of experimental approaches to fracture toughness evaluation at the micro-scale. *Materials & Design*, 173:107762, 2019.

[123] ASTM Standard. E399, standard test method for linear-elastic plane-strain fracture toughness kic of metallic materials. *ASTM Book of Standards, ASTM International, West Conshohocken, PA*, 2012.

[124] F Iqbal, J Ast, M Göken, and K Durst. In situ micro-cantilever tests to study fracture properties of nial single crystals. *Acta Materialia*, 60(3):1193–1200, 2012.

[125] David Broek. *Elementary engineering fracture mechanics*. Springer Science & Business Media, 1982.

[126] Peter L Raffo. Yielding and fracture in tungsten and tungsten-rhenium alloys. *Journal of the Less Common Metals*, 17(2):133–149, 1969.

[127] E1820-05 Astm et al. Standard test method for measurement of fracture toughness. *ASTM, Annual Book of Standards*, 3, 1820.

[128] Markus Alfreider, Darjan Kozic, Otmar Kolednik, and Daniel Kiener. In-situ elastic-plastic fracture mechanics on the microscale by means of continuous dynamical testing. *Materials & Design*, 148:177–187, 2018.

[129] Szilvia Kalácska, Johannes Ast, Péter Dusán Ispánovity, Johann Michler, and Xavier Maeder. 3d hr-ebsd characterization of the plastic zone around crack tips in tungsten single crystals at the micron scale. *Acta Materialia*, 200:211–222, 2020.

[130] Robb Thomson, C Hsieh, and V Rana. Lattice trapping of fracture cracks. *Journal of Applied Physics*, 42(8):3154–3160, 1971.

[131] Praveenkumar Hiremath, Solveig Melin, Erik Bitzek, and Pär AT Olsson. Effects of interatomic potential on fracture behaviour in single-and bicrystalline tungsten. *Computational Materials Science*, 207:111283, 2022.

[132] Reinhard Pippan, Stefan Wurster, and Daniel Kiener. Fracture mechanics of micro samples: fundamental considerations. *Materials & Design*, 159:252–267, 2018.

[133] WW Gerberich, J Michler, WM Mook, R Ghisleni, F Östlund, DD Stauffer, and R Ballarini. Scale effects for strength, ductility, and toughness in "brittle" materials. *Journal of Materials Research*, 24(3):898–906, 2009.

[134] Yu Zou, Pawel Kuczera, Alla Sologubenko, Takashi Sumigawa, Takayuki Kitamura, Walter Steurer, and Ralph Spolenak. Superior room-temperature ductility of typically brittle quasicrystals at small sizes. *Nature communications*, 7(1):1–7, 2016.

[135] Marta Pozuelo, Joseph Lefebvre, Pratyush Srivastava, and Vijay Gupta. Stishovite formation at very low pressures in soda-lime glass. *Scripta Materialia*, 171:6–9, 2019.

[136] B-S Li, TJ Marrow, SG Roberts, and DEJ Armstrong. Evaluation of fracture toughness measurements using chevron-notched silicon and tungsten microcantilevers. *JOM*, 71(10): 3378–3389, 2019.

[137] Steffen Brinckmann, Kurt Matoy, Christoph Kirchlechner, and Gerhard Dehm. On the influence of microcantilever pre-crack geometries on the apparent fracture toughness of brittle materials. *Acta Materialia*, 136:281–287, 2017.

[138] Sally June Tracy, Stefan J Turneaure, and Thomas S Duffy. In situ x-ray diffraction of shock-compressed fused silica. *Physical review letters*, 120(13):135702, 2018.

[139] C Scott Alexander, LC Chhabildas, and DW Templeton. The hugoniot elastic limit of soda-lime glass. In *AIP Conference Proceedings*, volume 955, pages 733–738. American Institute of Physics, 2007.

[140] Kathryn E Brown, William L Shaw, Xianxu Zheng, and Dana D Dlott. Simplified laser-driven flyer plates for shock compression science. *Review of Scientific Instruments*, 83(10):103901, 2012.

[141] AD Curtis and DD Dlott. Dynamics of shocks in laser-launched flyer plates probed by photon doppler velocimetry. In *Journal of Physics: Conference Series*, volume 500, page 192002. IOP Publishing, 2014.

[142] Alexandr A Banishev, William L Shaw, Will P Bassett, and Dana D Dlott. High-speed laser-launched flyer impacts studied with ultrafast photography and velocimetry. *Journal of Dynamic Behavior of Materials*, 2(2):194–206, 2016.

[143] Hiroki Fujiwara, Kathryn Brown, and Dana Dlott. A thin-film hugoniot measurement using a laser-driven flyer plate. In *AIP Conference Proceedings*, volume 1426, pages 382–385. American Institute of Physics, 2012.

[144] Wei-Qi Huang, Shi-Rong Liu, Zhong-Mei Huang, Ti-Ger Dong, Gang Wang, and Cao-Jian Qin. Magic electron affection in preparation process of silicon nanocrystal. *Scientific Reports*, 5(1):1–6, 2015.

[145] NK Bourne and Z Rosenberg. The dynamic response of soda-lime glass. In *AIP Conference Proceedings*, volume 370, pages 567–572. American Institute of Physics, 1996.

[146] Sairam Sundaram and Rodney J Clifton. The influence of a glassy phase on the high strain rate response of a ceramic. *Mechanics of materials*, 29(3-4):233–251, 1998.

[147] Rodney J Clifton. Response of materials under dynamic loading. *International Journal of Solids and Structures*, 37(1-2):105–113, 2000.

[148] RJ Clifton, M Mello, and NS Brar. Effect of shear on failure waves in soda lime glass. In *AIP Conference Proceedings*, volume 429, pages 521–524. American Institute of Physics, 1998.

[149] Yuan Shen, Shai B Jester, Tingting Qi, and Evan J Reed. Nanosecond homogeneous nucleation and crystal growth in shock-compressed sio2. *Nature materials*, 15(1):60–65, 2016.

[150] M Grujicic, WC Bell, PS Glomski, B Pandurangan, BA Cheeseman, C Fountzoulas, and P Patel. Multi-length scale modeling of high-pressure-induced phase transformations in soda-lime glass. *Journal of Materials Engineering and Performance*, 20(7):1144–1156, 2011.

[151] Anatolii N Dremin and Oleg Nikolaevich Breusov. Processes occurring in solids under the action of powerful shock waves. *Russian Chemical Reviews*, 37(5):392, 1968.

[152] Sung Keun Lee and Jonathan F Stebbins. Nature of cation mixing and ordering in na-ca silicate glasses and melts. *The Journal of Physical Chemistry B*, 107(14):3141–3148, 2003.

[153] CA Pampillo and HS Chen. Comprehensive plastic deformation of a bulk metallic glass. *Materials Science and Engineering*, 13(2):181–188, 1974.

[154] FM Ernsberger. Role of densification in deformation of glasses under point loading. *Journal of the American Ceramic Society*, 51(10):545–547, 1968.

[155] M Grujicic, WC Bell, B Pandurangan, BA Cheeseman, C Fountzoulas, and P Patel. Molecular-level simulations of shock generation and propagation in soda-lime glass. *Journal of Materials Engineering and Performance*, 21(8):1580–1590, 2012.

[156] Ulrich Mansfeld, Falko Langenhorst, Matthias Ebert, Astrid Kowitz, and Ralf Thomas Schmitt. Microscopic evidence of stishovite generated in low-pressure shock experiments on porous sandstone: Constraints on its genesis. *Meteoritics & Planetary Science*, 52(7): 1449–1464, 2017.

[157] Shiteng Zhao, Bimal Kad, Bruce A Remington, Jerry C LaSalvia, Christopher E Wehrenberg, Kristopher D Behler, and Marc A Meyers. Directional amorphization of boron carbide subjected to laser shock compression. *Proceedings of the National Academy of Sciences*, 113 (43):12088–12093, 2016.

[158] Matthew DeVries, Ghatu Subhash, and Amnaya Awasthi. Shocked ceramics melt: An atomistic analysis of thermodynamic behavior of boron carbide. *Physical Review B*, 101(14): 144107, 2020.

[159] AE Gleason, CA Bolme, HJ Lee, B Nagler, E Galtier, RG Kraus, R Sandberg, W Yang, F Langenhorst, and WL Mao. Time-resolved diffraction of shock-released sio2 and diaplectic glass formation. *Nature communications*, 8(1):1–6, 2017.

[160] DR Allen, JC Foley, and JH Perepezko. Nanocrystal development during primary crystallization of amorphous alloys. *Acta materialia*, 46(2):431–440, 1998.

[161] Y He, GJ Shiflet, and SJ Poon. Ball milling-induced nanocrystal formation in aluminum-based metallic glasses. *Acta metallurgica et materialia*, 43(1):83–91, 1995.

[162] F Ye and K Lu. Crystallization kinetics of amorphous solids under pressure. *Physical Review B*, 60(10):7018, 1999.

[163] Frans Spaepen. A microscopic mechanism for steady state inhomogeneous flow in metallic glasses. *Acta metallurgica*, 25(4):407–415, 1977.

[164] M Gogebakan, PJ Warren, and B Cantor. Crystallization behaviour of amorphous al85y11ni4 alloy. *Materials Science and Engineering: A*, 226:168–172, 1997.

[165] Alison Kubota, Maria-Jose Caturla, Lilian Davila, James Stolken, Babak Sadigh, Andrew Quong, Alexander M Rubenchik, and Michael D Feit. Structural modifications in fused silica due to laser-damage-induced shock compression. In *Laser-Induced Damage in Optical Materials: 2001*, volume 4679, pages 108–116. SPIE, 2002.

[166] FV Natrup, H Bracht, S Murugavel, and B Roling. Cation diffusion and ionic conductivity in soda-lime silicate glasses. *Physical chemistry chemical physics*, 7(11):2279–2286, 2005.

[167] R Lacroix, G Kermouche, J Teisseire, and E Barthel. Plastic deformation and residual stresses in amorphous silica pillars under uniaxial loading. *Acta Materialia*, 60(15):5555–5566, 2012.

[168] T Deschamps, A Kassir-Bodon, C Sonneville, J Margueritat, C Martinet, D De Ligny, A Mermet, and B Champagnon. Permanent densification of compressed silica glass: a raman-density calibration curve. *Journal of Physics: Condensed Matter*, 25(2):025402, 2012.

[169] Sheng-Nian Luo, Thomas J Ahrens, and Paul D Asimow. Polymorphism, superheating, and amorphization of silica upon shock wave loading and release. *Journal of Geophysical Research: Solid Earth*, 108(B9), 2003.

[170] Mica Grujicic, Jennifer Snipes, S Ramaswami, Ramin Yavari, and Bryan Cheeseman. Densification and devitrification of fused silica induced by ballistic impact: a computational investigation. *Journal of Nanomaterials*, 2015, 2015.

[171] Sheng-Nian Luo, JL Mosenfelder, Paul D Asimow, and Thomas J Ahrens. Direct shock wave loading of stishovite to 235 gpa: Implications for perovskite stability relative to an oxide assemblage at lower mantle conditions. *Geophysical Research Letters*, 29(14):36–1, 2002.

[172] Thomas J Ahrens. Equation of state. In *High-pressure shock compression of solids*, pages 75–113. Springer, 1993.

[173] Vladimir Bliznetsov, Hua Mao Lin, Yue Jia Zhang, and David Johnson. Deep sio2 etching with al and aln masks for mems devices. *Journal of Micromechanics and Microengineering*, 25(8):087002, 2015.

[174] Stanley P Marsh. *LASL shock Hugoniot data*. University of California press, 1980.

[175] Susan Werner Kieffer. Shock metamorphism of the coconino sandstone at meteor crater, arizona. *Journal of Geophysical Research*, 76(23):5449–5473, 1971.

[176] Astrid Kowitz, Ralf T Schmitt, W Uwe Reimold, and Ulrich Hornemann. The first memin shock recovery experiments at low shock pressure (5–12.5 gpa) with dry, porous sandstone. *Meteoritics & Planetary Science*, 48(1):99–114, 2013.

[177] A Kowitz, N Güldemeister, WU Reimold, RT Schmitt, and K Wünnemann. Diaplectic quartz glass and sio2 melt experimentally generated at only 5 gpa shock pressure in porous sandstone: Laboratory observations and meso-scale numerical modeling. *Earth and Planetary Science Letters*, 384:17–26, 2013.

[178] DE Grady. Shock deformation of brittle solids. *Journal of Geophysical Research: Solid Earth*, 85(B2):913–924, 1980.

[179] Hua Tan and Thomas J Ahrens. Shock induced polymorphic transition in quartz, carbon, and boron nitride. *Journal of Applied Physics*, 67(1):217–224, 1990.

[180] Falko Langenhorst and Jean-Paul Poirier. Anatomy of black veins in zagami: clues to the formation of high-pressure phases. *Earth and Planetary Science Letters*, 184(1):37–55, 2000.

[181] Will P Bassett and Dana D Dlott. High dynamic range emission measurements of shocked energetic materials: Octahydro-1, 3, 5, 7-tetranitro-1, 3, 5, 7-tetrazocine (hmx). *Journal of Applied Physics*, 119(22):225103, 2016.

[182] Will P Bassett and Dana D Dlott. 32-channel pyrometer with high dynamic range for studies of shocked nanothermites. In *AIP Conference Proceedings*, volume 1793, page 060012. AIP Publishing LLC, 2017.

[183] Michal Marszewski, Sophia C King, Yan Yan, Tiphaine Galy, Man Li, Ali Dashti, Danielle M Butts, Joon Sang Kang, Patricia E McNeil, Esther Lan, et al. Thick transparent nanoparticle-based mesoporous silica monolithic slabs for thermally insulating window materials. *ACS Applied Nano Materials*, 2(7):4547–4555, 2019.

[184] Michal Marszewski, Ali Dashti, Patricia E McNeil, Maggie Fox, Vivian Wall, Danielle M Butts, Sophia C King, Glareh N Kashanchi, Sarah H Tolbert, Bruce Dunn, et al. Elastic and plastic mechanical properties of nanoparticle-based silica aerogels and xerogels. *Microporous and Mesoporous Materials*, 330:111569, 2022.